BREAKTHROUGH OF ULTRASONIC IMAGING: FROM LINEAR ARRAY TO SPARSE NETWORK

XIONGBIN YANG

PhD

The Hong Kong Polytechnic University

2022

The Hong Kong Polytechnic University

Department of Mechanical Engineering

Breakthrough of Ultrasonic Imaging: from Linear Array to Sparse Network

Xiongbin YANG

A thesis submitted in partial fulfillment of the requirements

for the degree of Doctor of Philosophy

October 2021

CERTIFICATE OF ORIGINALITY

I hereby declare that this thesis is my own work and that, to the best of my knowledge and belief, it reproduces no material previously published or written, nor material that has been accepted for the award of any other degree or diploma, except where due acknowledgment has been made in the text.

Xiongbin YANG

ABSTRACT

Damage identification is somewhat like a detective task to catch the 'culprit' – defect or damage committed to materials and structures. Driven by the motivation to 'visualize' the 'culprit', diagnostic imaging using ultrasonic waves has been studied intensively and extensively over the past decades, to project identified defect or damage in an easily interpretable and intuitional quantitative image concerning the overall 'health' state of the structure under inspection. Nevertheless, prevailing diagnostic imaging approaches such as reverse time migration (RTM) and multiple signal classification (MUSIC), still show limitations when used in practice, particularly including

(i) **inferior imaging quality of the flaw**: as a common problem of most imaging approaches, the image quality of lower flaw surfaces is usually inadequate, leading to possible **deficiency** in depicting full features of flaw;

(ii) **limited capability to detect flaw in specimens featuring irregular surfaces**: prevailing imaging techniques often show proven effectiveness for a specimen with a flat surface that is either in parallel or oblique to the surface of the phased array, and it is a challenge to detect the specimens with non-planar surfaces;

(iii) **incomplete coverage of inspection region**: prevailing MUSIC methods are largely bound up with the use of a linear array, leaving blind zones and failing to access the full planar area of an inspected sample;

(iv) **insufficient signal features**: prevailing MUSIC algorithm, manipulated in the time domain, is applicable to monochromatic excitation only, ignoring

signal features spanning a broad frequency band which also carry information of damage; and

(v) **lack of *in-situ* structural health monitoring (SHM) strategy**: restricted by the use of bulky transducers, mobile manipulation, and computationally expensive imaging algorithms, it is a tough task to extend diagnostic imaging to real-time, continuous, *in-situ* SHM.

In recognition of the foregoing deficiencies in conventional ultrasonic imaging, a new ultrasonic imaging framework is developed in this PhD study.

First, an enhanced reverse time migration (ERTM) algorithm is developed, targeting superior imaging of full features of the embedded flaw in engineering material. On the basis of the multipath scattering analysis and Fermat's principle of the acoustic wave propagation, the algorithm establishes a new wavefield extrapolation model and presents a virtual phased array to reconstruct the lower surface of the embedded flaw. In conjunction with the flaw upper surface constructed by the actual phased array, the complete flaw features can be precisely delineated. The effectiveness of the ERTM approach is demonstrated by evaluating flaw with different geometric profiles in both simulation and experiment. Results show that, in comparison with the conventional RTM and TFM, the developed EMTR method can efficiently and accurately depict the full profiles of the flaw, providing a great alternative for characterizing flaw of complex shapes.

To extend the above imaging algorithm to an inspected specimen featuring an irregular top surface, an RTM-based multistep angular spectrum approach (ASA) imaging framework is developed. Central to the framework is a multistep ASA, via which the forward propagation wavefields of wave sources and backward propagation wavefields of the received wave signals are calculated. Upon applying a zero-lag cross-correlation imaging condition of RTM to the obtained forward and backward wavefields, the image of the specimen with an irregular surface can be reconstructed, in which hidden damage, if any and regardless of quantity, are visualized. The effectiveness and accuracy of the framework are examined using numerical simulation, followed with experiments, in which multiple side-drilled holes, at different locations in aluminum blocks with various irregular surfaces, are characterized. The validation affirms that the RTM-based multistep ASA shows an enhanced imaging resolution and contrast against conventional TFM.

An ameliorated multiple signal classification (Am-MUSIC) algorithm is proposed to remove the limitation of linear sensor array arrangement in conventional methods and to improve imaging resolution. The new method manipulates the signal representation matrix at each pixel using the excitation signal series, instead of the scattered signal series, which enables the use of a sparse sensor network with arbitrarily positioned transducers. By quantifying the orthogonal attributes between the signal subspace and noise subspace inherent in the signal representation matrix, a full spatial spectrum of the inspected sample can be generated, to visualize damage in the sample. Am-MUSIC is validated, in both simulation and experiment, by evaluating damage in plate-like waveguides with a sparse sensor network. Results verify that Am-MUSIC has full access to a sample, eliminating blind zones; and the amelioration expands conventional MUSIC from phased array-facilitated nondestructive evaluation to health monitoring using built-in sparse sensor networks.

Although Am-MUSIC algorithm expands conventional MUSIC algorithm from linear array-facilitated nondestructive evaluation to *in-situ* health monitoring with a sparse sensor network, a twofold issue still leaves to be improved: i) the signal representation equation is constructed at each pixel across the inspection region, incurring high computational cost; and ii) the algorithm is applicable to monochromatic excitation only, ignoring signal features scattered out of the excitation frequency band which also carry information on structural integrity. With this motivation, a multiple-damage-scattered wavefield model is developed, with which the signal representation equation is constructed in the frequency domain, avoiding computationally expensive pixel-based calculation – referred to as frequency-domain MUSIC (F-MUSIC). F-MUSIC quantifies the orthogonal attributes between the signal subspace and noise subspace inherent in the signal representation equation, and generates a full spatial spectrum of the inspected sample to visualize damage. Modeling in the frequency domain endows F-MUSIC with the capacity to fuse rich information scattered in a broad band and therefore enhance imaging precision. Both simulation and experiment are performed to validate F-MUSIC when used for imaging single and multiple sites of damage in a plate waveguide with a sparse sensor network. Results accentuate that the effectiveness of F-MUSIC is not limited by the quantity of damage and precision is not downgraded due to the use of a highly sparse sensor network – a challenging task for conventional MUSIC algorithm to fulfill.

Finally, an *in-situ* SHM diagnosis framework, from sensing to the presentation of diagnostic results, is established by integrating the all-printed nanocomposite sensor array (APNSA) and MUSIC diagnosis algorithm. The new breed of nanocomposite-based ultrasonic sensor – APNSA – is fabricated, in lieu of the conventional transducer array, featuring not only full integration with the inspected structure, but also high flexibility, ultralight weight, and broadband responsivity. Supported by the APNSA sensor and used in conjunction with the MUSIC algorithm, the continuous monitoring of damage can be implemented. The effectiveness of the diagnosis framework is validated experimentally by characterizing structural damage in the composite laminates, and results highlight its alluring application prospects for damage detection and health status perception in a real-time, *in-situ* manner.

In conclusion, enriched with fundamental theory development, dedicated modeling, innovative transducer fabrication, and intensive experimentation, a novel diagnosis imaging framework is developed in this study, to break through some critical bottlenecks of ultrasonic imaging, and cement a feasible way to meet diverse requirements in applications.

PUBLICATIONS ARISING FROM THE THESIS

Refereed Journal Papers

1. **X. Yang**, K. Wang, P. Zhou, L. Xu, J. Liu, P. Sun, Z. Su, Ameliorated-multiple signal classification (Am-MUSIC) for damage imaging using a sparse sensor network, ***Mechanical Systems and Signal Processing***, 163 (2022) 108154. (JCR Q1, IF: 6.820)

2. **X. Yang**, K. Wang, P. Zhou, L. Xu, J. Liu, P. Sun, Z. Su, Imaging Damage in Plate Waveguides Using Frequency-domain Multiple Signal Classification (F-MUSIC), ***Ultrasonics***, 119 (2022) 106607. (JCR Q1, IF: 2.890)

3. **X. Yang**, P. Zhou, Y. Liao, Y. Su, J. Yang, L. Xu, K. Wang, Z. Zeng, L.-m. Zhou, Z. Su, Direct-write nanocomposite sensor array for ultrasonic imaging of composites, ***Composites Communications***, 28 (2021) 100937. (JCR Q1, IF: 6.617)

4. **X. Yang**, K. Wang, Y. Xu, L. Xu, W. Hu, H. Wang, Z. Su, A reverse time migration-based multistep angular spectrum approach for ultrasonic imaging of specimens with irregular surfaces, ***Ultrasonics***, 108 (2020) 106233. (JCR Q1, IF: 2.890)

5. P. Zhou, Y. Liao, **X. Yang**, Y. Su, J. Yang, L. Xu, K. Wang, Z. Zeng, L.-m. Zhou, Z. Zhang, Z. Su, Thermally stable, adhesively strong graphene/polyimide films for inkjet printing ultrasound sensors, ***Carbon***, 184 (2021) 64-71. (JCR Q1, IF: 9.594)

6. L. Xu, Y. Su, K. Wang, **X. Yang**, S. Yuan, Z. Su, An elastodynamic reciprocity theorem-based closed-form solution to second harmonic generation of lamb waves by a fatigue crack: Theory & experimental validation, ***Journal of***

Sound and Vibration, 509 (2021) 116226. (JCR Q1, IF: 3.655)

7. L. Xu, K. Wang, **X. Yang**, Y. Su, J. Yang, Y. Liao, P. Zhou, Z. Su, Model-driven fatigue crack characterization and growth prediction: A two-step, 3-D fatigue damage modeling framework for structural health monitoring, ***International Journal of Mechanical Sciences***, 195 (2021) 106226. (JCR Q1, IF: 5.329)

8. W. Cao, K. Wang, P. Zhou, **X. Yang**, L. Xu, M. Liu, P. Fromme, B. Pang, R. Chi, Z. Su, Nonlinear ultrasonic evaluation of disorderedly clustered pitting damage using an in situ sensor network, ***Structural Health Monitoring***, 19 (2020) 1989-2006. (JCR Q1, IF: 5.929)

9. P. Zhou, W. Cao, Y. Liao, K. Wang, **X. Yang**, J. Yang, Y. Su, L. Xu, L.-m. Zhou, Z. Zhang, Z. Su, Temperature effect on all-inkjet-printed nanocomposite piezoresistive sensors for ultrasonics-based health monitoring, ***Composites Science and Technology***, 197 (2020) 108273. (JCR Q1, IF: 8.528)

10. K. Wang, W. Cao, L. Xu, **X. Yang**, Z. Su, X. Zhang, L. Chen, Diffuse ultrasonic wave-based structuralhealth monitoring for railway turnouts, ***Ultrasonics***, 101 (2020) 106031. (JCR Q1, IF: 2.890)

11. W. Cao, Y. Wang, P. Zhou, **X. Yang**, K. Wang, B. Pang, R. Chi, Z. Su, Microstructural materialcharacterization of hypervelocity-impact-induced pitting damage, ***International Journal of Mechanical Sciences***, 163 (2019) 105097. (JCR Q1, IF: 5.329)

12. P. Zhou, Y. Liao, Y. Li, D. Pan, W. Cao, **X. Yang**, F. Zou, L.-m. Zhou, Z. Zhang, Z. Su, An inkjet-printed, flexible, ultra-broadband nanocomposite film sensor for in-situ acquisition of high-frequency dynamic strains, ***Composites Part A: Applied Science and Manufacturing***, 125 (2019) 105554. (JCR Q1, IF: 7.664)

13. W. Cao, P. Zhou, Y. Liao, **X. Yang**, D. Pan, Y. Li, B. Pang, L.-m. Zhou, Z. Su, A Spray-on, Nanocomposite-Based Sensor Network for in-Situ Active Structural Health Monitoring, ***Sensors***, 19 (2019). (JCR Q1, IF: 3.576)

Refereed Papers in International Conference Proceedings

1. W. Cao, K. Wang, L. Xu, P. Zhou, **X. Yang**, B. Pang, P. Fromme, Z. Su, Modally selective nonlinear ultrasonic waves for characterization of pitting damage in whipple shields of spacecraft, Health Monitoring of Structural and Biological Systems XIV, International Society for Optics and Photonics, 2020, pp. 113811M.

ACKNOWLEDGEMENTS

Upon completion of this thesis, I am grateful to those who have offered me encouragement and support during the journey of my study.

First, special acknowledgment is given to my respectable supervisor, Prof. Zhongqing SU, without whom I would not have even been funded to start my PhD study and accomplish what is presented here. No matter what difficulties I met in my research, he always gave me patient instruction and constructive suggestions, which have considerably contributed to this thesis and to my understanding in various subjects. Not just as an academic supervisor, he is also a great mentor in all aspects. He always took care of my life and shared his valuable experience, which made my life in Hong Kong so enjoyable. Again, so many thanks to him and it is a lifetime honor to learn from him.

Moreover, it is my great fortune to have met and befriended a group of great people. A special thanks to Dr. Kai Wang, with whom I could quickly become familiar with my research field and the lab at the very beginning. I am also indebted to Dr. Wuxiong Cao and Dr. Yanfeng Xu for their indispensable guidance and help during my graduate study. Besides, I give many thanks to Dr. Yaozhong Liao, Pengyu Zhou, and Dr. Yafeng Wang. They accompanied me to truly integrate into the life of Hong Kong and spend much enjoyable time. In addition, I am grateful to Dr. Yehai Li, Yiyin Su, Lei Xu, Jianwei Yang, and Dengue Pan. We shared a lot, which has enriched my graduate experience with friendship.

Last but not least, my gratitude goes out to my families for their encouragement and supports at all times. Regardless of a nearly two years of separation from my families due to the COVID-19, their love, care, and patience always accompany me, and I miss them so much.

NOMENCLATURE

Acronyms and Initialisms

Am-MUSIC	Ameliorated multiple signal classification
APNSA	All-printed nanocomposite sensor array
ART	Algebraic reconstruction technique
ASA	Angular spectrum approach
CF/EP	Carbon-fibre-reinforced epoxy
CTFM	Combined total focusing method
DI	Damage index
DOA	Direction of arrival
DORT	Decomposition of the Time Reversal Operator
ERTM	Enhanced reverse time migration
FBP	Filtered back projection
FEM	Finite element method
FMC	Full matrix capture
F-MUSIC	Frequency-domain *MUSIC*
FSTFM	Full-Skip total focusing method
HSTFM	Half-Skip total focusing method
IWEX	Inverse wavefield extrapolation

LPE	Liquid phase exfoliation
MTFM	Multi-view total focusing method
MUSIC	Multiple signal classification
NGP	Nanographene Platelets
NMP	Anhydrous n-methyl-2-pyrrolidone
PAA	Poly (amic acid)
PCF	Phase coherence factor
PCI	Phase coherence imaging
PDI	Probability-based diagnostic imaging
PRA	Probabilistic reconstruction algorithm
PVP	Polyvinyl pyrrolidone
PWI	Plane wave imaging
PZT	Lead zirconate titanate
RoI	Region of interest
RTM	Reverse time migration
SAFT	Synthetic aperture focusing technique
SCF	Sign coherence factor
SFCBR-MUSIC	Single frequency component-based re-estimated MUSIC
SHM	Structural health monitoring
STA	Synthetic Transmit Aperture
TFM	Total focusing method

ToF	Time-of-flight
TR	Time reversal
TRP	Time-reversal process
VTFM	Vector total focusing method
VTR	Virtual time reversal

Symbols

λ	Wavelength
f	Frequency
c	Wave velocity
c_L	Longitudinal wave velocity
c_T	Transverse wave velocity
E	Young's modulus
υ	Poisson's ratio
G	Shear modulus
ρ	Density
ω	Angular frequency
k	Wavenumber
t	Time
R_n^a	Actual receiver wavefields

S_n^v	Virtual source wavefields
R_n^v	Virtual receiver wavefields
S_n	Source wavefields
R_n	Receiver wavefields
I	Image value
P	Acoustic pressure distribution
$\hat{P}$	Angular spectrum
C	Generalized reflection coefficient
δ	Dirac function
k_x	Wavenumber along x direction in the spatial frequency domain
k_z	Wavenumber along z direction in the spatial frequency domain
k_{fluid}	Wavenumber in the fluid
c_{fluid}	Velocity of wave in the fluid
k_{solid}	Wavenumber in the solid
$\mathcal{F}^{-1}$	Inverse Fourier transform
d	travelling distance of guided waves
ω_0	Central frequency of the toneburst
τ_k	Wave propagation time difference
$\mathbf{R}^{\text{residual}}(t)$	Residual signal vector

$\mathbf{C}$	Covariance matrix
$E[\ ]$	Covariance computation
H	Complex conjugate transpose
σ^2	Noise power
μ	Eigenvector
$\mathbf{U}_S$	Signal subspace
$\mathbf{U}_N$	Noise subspace
c_p	Phase velocity
$\alpha(\omega)$	Scattering coefficient in the frequency domain
$\mathbf{a}$	Steering vector
$\mathbf{A}$	Steering vector dictionary
l	Uniform element spacing
$\boldsymbol{\omega}$	Broad frequency band
P_{MUSIC}	Pixel value of spatial spectrum obtained by MUSIC algorithm
$P_{AM-MUSIC}$	Pixel value of spatial spectrum obtained by AM-MUSIC algorithm
$P_{F-MUSIC}$	Pixel value of spatial spectrum obtained by F-MUSIC algorithm

TABLE OF CONTENTS

LIST OF FIGURES

LIST OF TABLES

CHAPTER 1

Introduction

1.1 Background and Motivation

Engineering assets in aerospace, ground transportation, ship-building, and civil industry are prone to various types of damage under adverse working conditions. Without timely awareness and appropriate remediation, material defects or structural damage can impact detrimental effects on structural integrity and potentially result in catastrophic consequences. Therefore, it is of incontrovertible significance but also a great challenge to identify and characterize the damage in the engineering structures. Subsequent to identification, timely remediation can be applied, to prevent further material deterioration, weaken the risk of consequent system failure, warrant the reliability, integrity, and durability of an engineering asset, and further bring immense economic and social benefits [1].

Addressing such significance, a wide variety of damage identification techniques has been developed, exemplified by eddy current [2], ultrasonic testing [3], infrared thermography [4], magnetic testing [5], laser vibrometry [6], dye penetrant testing [7], shearography [8] and radiography [9]. Among them, ultrasonic testing, as a non-invasive monitoring means, has been at the core of intensive efforts over the past decades and has shown the prominent capability for damage identification. As a matter of fact:

i) Ultrasonic waves, classified into bulk waves and guided waves depending on the patterns of particulate motion, can be used for damage detection in a diversity of application scenarios. Specifically, bulk waves, referred to as waves that propagate in media without boundaries, are commonly applied to detect damage embedded in a thick solid (*i.e.*, remote from the surface); while guided waves are confined by boundaries and guided by the structure, capable of monitoring damage in thin structures whose planar dimensions are far greater than their thickness, such as plates, rods, and tubes.

ii) Thanks to the high sensitivity of ultrasonic waves, ultrasonic testing is accurate for determining the damage location and characterizing its size and shape.

iii) Ultrasonic testing can be applied for a variety of materials, *e.g.*, metals, composites, concrete, and woods, compared to methods like magnetic testing which is limited to ferromagnetic materials.

iv) Ultrasonic testing is nonhazardous to operation personnel and inspected materials, unlike radiography which needs adequate protection.

v) Ultrasonic testing is capable of highly automated operation and on-site testing.

The basic principle of ultrasonic testing is that the interaction of ultrasonic waves with structural damage can significantly influence their propagation, accompanied by wave reflection, scattering, and mode conversion. Upon capturing these characteristics and establishing relationships with damage parameters, the damage can be characterized.

With such a philosophy, damage identification using ultrasonic waves commonly includes the following essential steps:

i) activating desired ultrasonic waves and capturing the reflected waves (*pulse-echo*) or the transmitted waves (*pulse-catch*).

ii) extracting the characteristics of the captured wave signals, including delay in the time of transit, amplitude, frequency content, *etc***.**

iii) establishing the relationship between the extracted characteristics and damage performance in ultrasonic wavefields, including reflection, scattering, mode conversion, *etc*.

iv) figuring out the damage and estimating its severity with extracted characteristics, via the established relationship.

Though it appears straightforward, damage identification using ultrasonic waves is a typical inverse problem, which starts with the outcome (damage-scattered ultrasonic wave signals) and then needs to infer the reason (damage). Considering the fact that the inverse problem is often ill-posed and difficult to solve, continued efforts have been made to proposing solutions by means of proper techniques. As one of recent research focuses, imaging technique plays a significant role in solving an inverse problem and is widely adopted for damage identification [10-12]. In principle, the keystone of imaging technique is to project identified defect or damage to an intuitional and easy interpretation image via specific damage diagnostic imaging algorithms. In a synthetic image, each image pixel corresponds exclusively to a spatial location of the structure under inspection, and thus the defect or damage in the structure, if any, can be highlighted and depicted intuitively in the images, through investigating information borne by each pixel. Depending on the two basis wave modes of ultrasonic waves, imaging techniques can be commonly classified into bulk waves-based or guided waves-based.

For bulk wave-based imaging, scanning is the most straightforward approach and is commonly implemented using a single ultrasonic probe, in which the probe is maneuvered to move on a surface of the inspected sample and the arrival times of reflected waves are regularly recorded to construct an image [13, 14]. However, the single ultrasonic probe has fixed inspection parameters and provides very limited information. To enrich information for damage detection, an ultrasonic phased array, consisting of a number of small individual elements, has been introduced to cater to more versatile applications. As elements in a phased array can be sequentially activated with programmable time delays, phase differences can be created in the wavefronts and the resulting wave, as the synchronization of these wavefronts, shows strong directionality in propagation and is therefore termed beamforming. With various types of beamform, the phased array can be operated in different scanning patterns, as typified by linear scan, sectorial scan, and beam focusing scan [15-17].

Despite proven effectiveness when used for ultrasonic imaging, phased array scanning is time-consuming because different time delays need to be individually designed for each scanning direction or a focused point. Recently, a novel phased array-based imaging scheme is developed, in which the complete signal database of all transmitter-receiver element pairs, referred to as full matrix capture (FMC), is captured and post-processed by imaging algorithms to visualize damage [18]. The total focusing method (TFM) is one of the most representative post-processing imaging algorithms, which computes the time-of-flights (ToFs) of all transmitter-receiver element pairs for each inspected point using FMC data, achieving synthetically 'total focusing' at each pixel in an image [19]. Nevertheless, TFM imaging, as an amplitude-based algorithm, can be affected by numerous phenomena along the wave paths, such as diffraction, scattering losses, multiple reflections, resulting in lower resolution and artifacts in reconstructed images. To fully exploit FMC data so as to improve imaging accuracy and resolution, a wavefield-based method, reverse time migration (RTM), has been developed [20, 21].

RTM-based imaging method, on a basis of the wavefield extrapolation of the full-wave equation, is manipulated with a postulation that when a receiver wavefield is propagated backward from the receiver in the time domain, the wave components reflected from the internal damage will, in principle, focus at the location of the damage. The underlying principle of RTM-based imaging is the simultaneous extrapolation of forward propagation of wave sources and backward propagation of the received wave signals, followed by imaging formation via applying a cross-correlation imaging condition. Using such a philosophy, RTM-based imaging has been validated in various damage characterization scenarios.

However, prevailing bulk-wave based imaging methods show two major limitations in practice:

1) The image quality of a lower flaw surface is usually inadequate, leading to possible deficiency in depicting full features of a flaw [16]. This is because that: i) unlike abnormal tissues to be diagnosed in a clinic that has acoustic impedance similar to normal tissues, a flaw in engineering material (*e.g.,* a void) has a significantly distinct acoustic impedance from that of the intact

material, making it difficult for incident waves to penetrate the flaw and reach its lower surface; ii) the waves scattered from the lower flaw surface will still be heavily masked by a great number of waves reverberating between the top and bottom of the sample;

2) TFM and RTM-based imaging methods show proven effectiveness for a specimen with a flat surface that is either in parallel or oblique to the surface of the phased array, however, it is a challenge to detect the specimens with non-planar surfaces, respective of the fact that the non-planar surfaces are ubiquitous in engineering practice such as welds, molded components and pipelines [20].

These two challenges entail new research efforts, with a hope to circumvent the above deficiency of existing bulk-wave-based imaging.

For guided waves-based imaging, a sensor network consisting of multiple pairs of actuator-sensor is usually employed to provide desirable signal acquisition, followed with appropriate diagnostic imaging algorithms to depict damage. During implementation, the imaging algorithm is a predominant factor governing the accuracy and resolution that a reconstructed image can deliver, and this subject has attracted intensive research efforts over a long period, as typified by tomography-based imaging [22], ToF(time-of-flight)-based imaging [23], time-reversal (TR) imaging [24], probability-based imaging [25] and array signal processing-based imaging [26-30], to name a few.

Tomography-based imaging is based on the principle that a guided wave passes more easily through an intact structural region, whereas it is somewhat blocked ('attenuated') by damage. ToF is a straightforward feature of a guided wave signal that suggests the relative positions among the actuator, sensor and damage. The keystone of time-reversal imaging is that the damage can be assessed by quantifying the difference between the time reversed wave signals with regard to the original incident signals. In probability-based imaging, an appropriate damage index (DI) is extracted from captured guided wave signals to describe the probability of the presence of damage using a greyscale image. Array signal processing-based imaging can be implemented in various modalities, including minimum variance distortionless response method [27], subspace fitting method [28], maximum-likelihood method [29], and MUSIC algorithm [30].

Among them, the multiple signal classification (MUSIC) algorithm is a promising candidate owing to its attractive directional scanning and searching ability. Unlike the traditional imaging algorithms which rely on either ToF or amplitude information of guided wave signals [23, 27], MUSIC algorithm is an eigen-structure approach that utilizes the orthogonality of subspaces in wave signals to estimate damage features [31, 32]. The effectiveness of the MUSIC algorithm has been proved for identifying damage in numerous applications. Nevertheless, the algorithm still encounters some common problems: first, conventional MUSIC-based imaging methods are restricted to use the uniform linear sensor array that features a dense configuration of transmitter elements with a small enough element pitch, which barely covers the whole azimuth range 0°-360° and severely degrades the beamforming properties at the angles close to 0° and 180°, causing damage overridden in the regions of [0, 30°] or [150°, 180°] in most circumstances [33]. In addition, previous studies prior on MUSIC algorithms are applicable to monochromatic excitation only, ignoring signal features spanning a broad frequency band which also carry information of damage, potentially resulting in identification errors [34, 35]. Finally, linear sensor arrays in the previous studies are commonly configured by manually aligning a certain number of lead zirconate titanate (PZT) wafers [36-38]. Such a means is of a low degree of coupling compatibility with inspection structure, limited adaptation to curved or geometrically complex structural surface and low inspection reliability due to human interference [39]. In particular, the impossibility of integrating a bulky array with the inspected structure precludes the linear array-based inspection from being extended from offline damage detection to real-time, *in-situ* diagnostic imaging. All these limitations considerably hamper widespread use of conventional MUSIC-based methods in guided wave-based diagnostic imaging, stimulating efforts to improve the versatility of MUSIC-based methods by possibly ameliorated imaging strategies.

In conclusion, although remarkable progress has been made towards both bulk wave-based and guided wave-based diagnostic imaging, there still exist some challenging issues for future development of such a technique, and some of them are briefed as below:

i) the image quality of a lower flaw surface is usually inadequate, leading to possible deficiency in depicting full features of a flaw in bulk wave-based imaging;

ii) it is a challenge for bulk wave-based diagnostic imaging to detect the specimens featuring an irregular top surface;

iii) in guided wave-based diagnostic imaging, prevailing MUSIC-based methods are largely bound up with the use of a linear array. Constricted by this, it is a challenge to access the full planar area of an inspected sample, leaving blind zones to which an array fails to scan;

iv) the prevailing MUSIC algorithm in guided wave imaging, manipulated in the time domain, is applicable to monochromatic excitation only, ignoring signal features spanning a broad frequency band which also carry information of damage; and

v) the use of bulky linear arrays along with computationally expensive imaging algorithms obviously restricts the extension of imaging to real-time, continuous, *in-situ* structural health monitoring (SHM).

1.2 Research Objectives

To circumvent the above-addressed deficiencies of the prevailing ultrasonic imaging techniques both in bulk wave-based and guided wave-based testing, this PhD research is dedicated to developing a diagnostic imaging framework, to improve the detectability and accuracy of prevailing imaging-based damage identification. Addressing the inefficiencies of existing methods, the following specific objectives are expected to achieve in this PhD study:

i) to develop an enhanced reverse time migration (ERTM) algorithm for the precise delineation of the damage with the full feature, whereby both the higher and the lower surfaces of embedded damage can be characterized effectively;

ii) to propose an RTM-based multistep angular spectrum approach (ASA) imaging framework for detecting the specimen with an irregular top surface and depicting the multiple damage sites hidden in the specimen;

iii) to develop an ameliorated multiple signal classification (Am-MUSIC) algorithm for damage detection using sparse sensor networks, target removing the limitation of uniform sensor array arrangement and improving imaging resolution;

iv) to present the frequency-domain MUSIC (F-MUSIC) algorithm, aim at lowering the computational costs, fusing rich information scattered in a broad band and detecting multiple damage sites;

v) to propose an *in-situ* health diagnosis framework, from sensing to diagnosis, to implement ultrasonic imaging from offline testing to real-time, *in-situ* SHM.

1.3 Scope of the Thesis

In this PhD thesis, a new diagnostic imaging framework for ultrasonic wave-driven damage characterization is proposed, featuring theoretical analysis, numerical modeling, experimental validation, and proof-of-concept application paradigm. The chapters are organized roughly in the order of fundamental investigation, algorithm development, and engineering applications.

The state of the art of ultrasonic wave-driven diagnostic imaging approaches is reviewed in Chapter 2. Fundamentals of bulk waves and guided waves are briefly recapitulated, and principles of damage identification using both two types of waves are described. Particular emphasis is placed on the discussion of the prevailing diagnostic imaging algorithms, especially their applications and limitations.

In Chapter 3, the ERTM algorithm is investigated for depicting damage characterization and geometric profiling. This algorithm, on the basis of the multipath scattering analysis and Fermat's principle of the acoustic wave propagation, presents a virtual phased array to characterize the lower surface of the embedded damage. In conjunction with the damage upper surface constructed by the actual phased array, the full features damage can be precisely delineated. At the end of the chapter, both simulation and experiment are performed with ETRM algorithm when used for imaging damage with different geometric profiles.

Chapter 4 is pertaining to the development of an RTM-based multistep angular spectrum approach (ASA) imaging framework for non-destructive evaluation of the specimen featuring an irregular top surface. Central to the framework is a multistep angular spectrum approach (ASA), via which the forward propagation wavefields of wave sources and backward propagation wavefields of the received wave signals are calculated. Upon applying a zero-lag cross-correlation imaging condition of RTM to the obtained forward and backward wavefields, the image of the specimen with an irregular surface can be reconstructed, in which hidden damage, if any and regardless of quantity, are visualized. Experiments are performed to validate the proposed approach, in which multiple damage, at different locations in aluminum blocks with various irregular surfaces, are characterized quantitatively.

In Chapter 5, an Am-MUSIC algorithm is proposed to remove the limitation of uniform sensor array arrangement in the conventional method and improve damage imaging resolution. In the Am-MUSIC algorithm, the signal representation matrix at each pixel is manipulated by the excitation signal series, instead of the scattered signal series, which enables the use of a sparse sensor network with arbitrarily positioned transducers rather than a linear array featuring a dense configuration of transducing elements with a uniform element pitch. By quantifying the orthogonal attributes between the signal subspace and noise subspace inherent in the signal representation matrix, a full spatial spectrum of the inspected sample can be generated, to visualize damage in the sample. The performance of the F-MUSIC algorithm is also verified by both simulations and experiments.

Aimed at exploiting the merits of the Am-MUSIC algorithm earlier developed (particularly its flexibility in configuring a sensor network) but surmounting the deficiency that the algorithm remains, the F-MUSIC algorithm is developed in Chapter 6. F-MUSIC constructs the multiple-damage-scattered wavefield model over the frequency domain, rather than at each pixel in the spatial domain, to avoid computationally expensive pixel-based calculation. With quantifying the orthogonal attributes and integrating the calculation over a broad frequency band, F-MUSIC can fuse rich information scattered in a broad band and therefore enhance imaging precision. Both simulation and experiment are also performed to validate F-MUSIC when used for imaging single and multiple sites of damage in a plate waveguide with a sparse sensor network.

In Chapter 7, an *in-situ* health diagnosis framework, from sensing to diagnosis, is developed by integrating the APNSA sensor and MUSIC diagnosis algorithm. The fabrication of this new APNSA sensor is first elucidated, and its performance is then examined in a broadband ultrasonic regime. Supported by such a novel sensor and used in conjunction with the MUSIC algorithm, the diagnosis framework is implemented and its effectiveness is also validated through laboratorial investigation.

Chapter 8 serves as the conclusion of the thesis, where recommendations for future research are also made.

CHAPTER 2

State of the Art of Diagnostic Imaging: A Literature Review

2.1 Introduction

With the motivation to 'visualize' material defect or structural damage, diagnostic imaging using ultrasonic waves has been the core of intensive research in recent years. This chapter reviews the state of the art of ultrasonic wave-driven diagnostic imaging approaches.

Depending on the two basic wave modes of ultrasonic waves, diagnostic imaging approaches can be subdivided into two categories: the bulk waves-based and the guided waves-based [40]. The former has been primarily utilized for damage detection of the thick solid, as represented by scanning-based imaging, delay-and-sum-based imaging, and inversion-based imaging; whereas the latter is used to detect damage in thin plate/shell structures [41], which can be implemented in various modalities including tomography imaging, time-of-flight-based imaging, time-reversal imaging, probability-based diagnostic imaging and array signal processing-based imaging. Targeting developing a new diagnostic imaging framework, particular emphasis in this chapter is placed on the discussion of these diagnostic imaging approaches, especially their applications and limitations.

2.2 Bulk Wave-based Imaging Using Phased Arrays

2.2.1 Fundamentals of Bulk Wave-based Imaging

Waves that propagate in an object, independent of its boundary and shape, are called bulk waves [42]. Bulk waves can propagate in two basic modes in an infinite medium: longitudinal modes and transverse modes, as shown schematically in **Figure 2.1**. In longitudinal waves, particles move in the parallel direction to the energy transfer. Since longitudinal waves are commonly accompanied by compression forces, they can be generated in gases, liquids, as well as solids. Transverse waves are defined as waves whose particle motion is perpendicular to the direction of the energy transfer. Due to no shear strength in liquids and gasses, transverse waves only exist in solids.

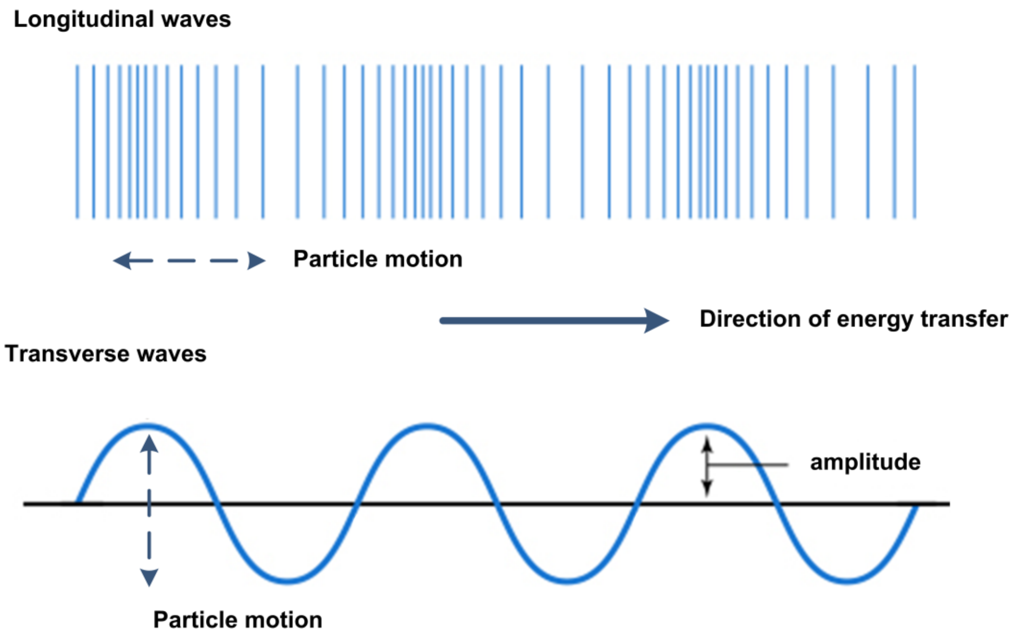

Figure 2.1 Longitudinal waves and transverse waves.

Velocity, as the most commonly used parameter in ultrasonic imaging, is typically determined by the elastic properties and density of the medium. For isotropic solids, the longitudinal and transverse wave velocities can be represented as [43]:

$$c_L = \sqrt{\frac{E(1-\upsilon)}{\rho(1+\upsilon)(1-2\upsilon)}}, \tag{2.1}$$

$$c_T = \sqrt{\frac{E}{2\rho(1+\upsilon)}} = \sqrt{\frac{G}{\rho}}, \tag{2.2}$$

where, c_L and c_T are the longitudinal and transverse wave velocities, respectively, E is Young's modulus, υ is Poisson's ratio, G is shear modulus and ρ is the density.

Generally, efficient activation and acquisition of ultrasonic waves is the prerequisite of ultrasonic wave-based damage detection, and therefore ultrasonic probes have been introduced. Thanks to its high flexibility and good controllability, the single element ultrasonic probe, **Figure 2.2**, is the most popular transducer for activating and capturing ultrasonic waves [44]. Signals captured by a single element probe are easy to interpret as the function of the wave traveling time, and the distance to the damage can be determined with the reflected time and known wave speed.

Nevertheless, the single element probe needs to be maneuvered during the practical implementation, incurring the high time consumption when inspecting a large structure. In addition, the single element probe has fixed inspection parameters including the aperture and the entry angle, failing to meet diverse requirements in engineering applications. Furthermore, the information provided by a single ultrasonic probe is limited, resulting in the poor capability of depicting full features of the damage.

Figure 2.2 Typical single element ultrasonic probes [45].

To circumvent these limitations, ultrasonic phased array probes, with some examples in **Figure 2.3**, have been developed to cater for more versatile applications [46-49]. A typical phased array consists of a number of transducer elements (typically from 16 to 256), as shown in **Figure 2.4**. Each element is connected to an individual channel in the array controller and can act as both a transmitter and a receiver. Thanks to such a superb characteristic, the damage identification technique using phased arrays is a promising method, in lieu of the traditional single probe-based approach, which presents the following features:

i) the capability of automated implementation, thereby simplifying the inspection procedure and reducing human interference;

ii) the capacity to generate multiple scanning patterns including sweeping, steering and focusing by appropriately designing the time delay of each element, thereby meeting diverse requirements in applications; and

iii) the ability to capture and record a large number of signals, enriching information for damage detection and therefore providing higher identification accuracy.

Figure 2.3 Typical ultrasonic phased array probes [50].

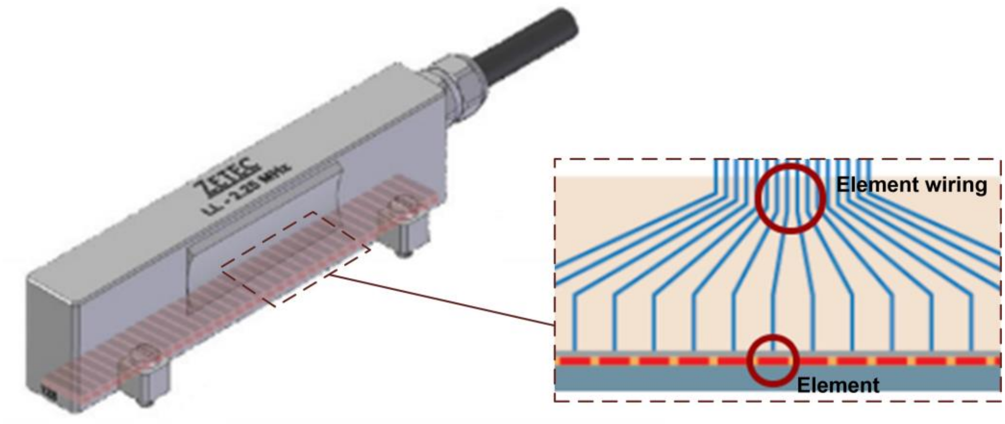

Figure 2.4 Schematic of an ultrasonic phased array probe [51].

With the original waveforms captured by a phased array, an easily interpretable and intuitional image is efficient to depict damage in terms of the location, size, shape and severity. Motivated by this, various phased array-based imaging methods have been increasingly studied [52-57], as categorized into i) scanning-based imaging, ii) delay-and-sum-based imaging, and iii) inversion-based imaging.

2.2.2 Scanning-based Imaging

Scanning is the most straightforward approach to construct an image of the inspected structure, which can be implemented using a single-element probe [14, 58, 59]. If the single-element probe is installed in a fixed position for both wave transmitting and receiving, **Figure 2.5(a)**, the testing results could be displayed as A-scan (amplitude scan), in which the amplitude of the signal is represented as a function of time, as shown in **Figure 2.5(b)**. When the probe is moved along a line and A-scan data are recorded regularly, B-scan (brightness scan) can be obtained, **Figure 2.6**. B-scan facilitates a two-dimensional (2D) image whose color scale implies damage and two axes represent the horizontal distance along with the specimen and the vertical distance (depth) into the specimen, respectively. As an extension of the B-scan, the C-scan pattern is implemented by moving the probe in two dimensions, displaying the test-piece in a top view, illustrated in **Figure 2.7**.

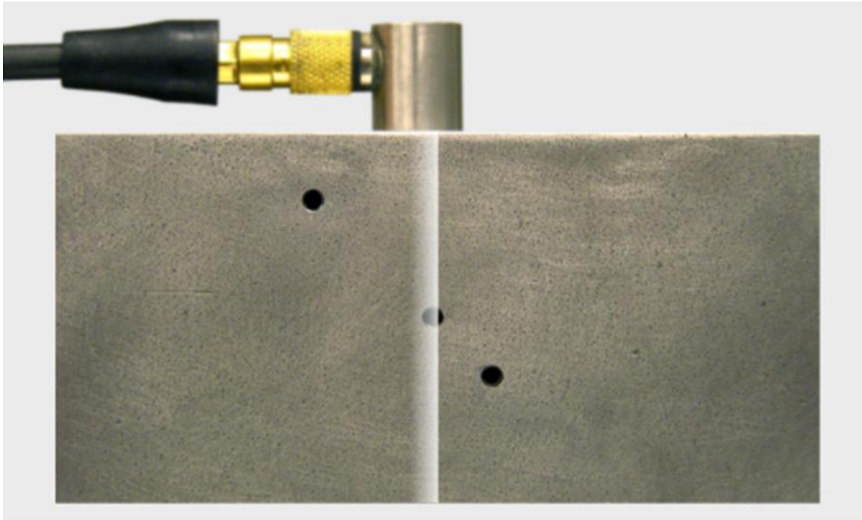

(a)

(b)

Figure 2.5 (a) A-scan with a single-element probe; and (b) A-scan result with a single-element probe [60].

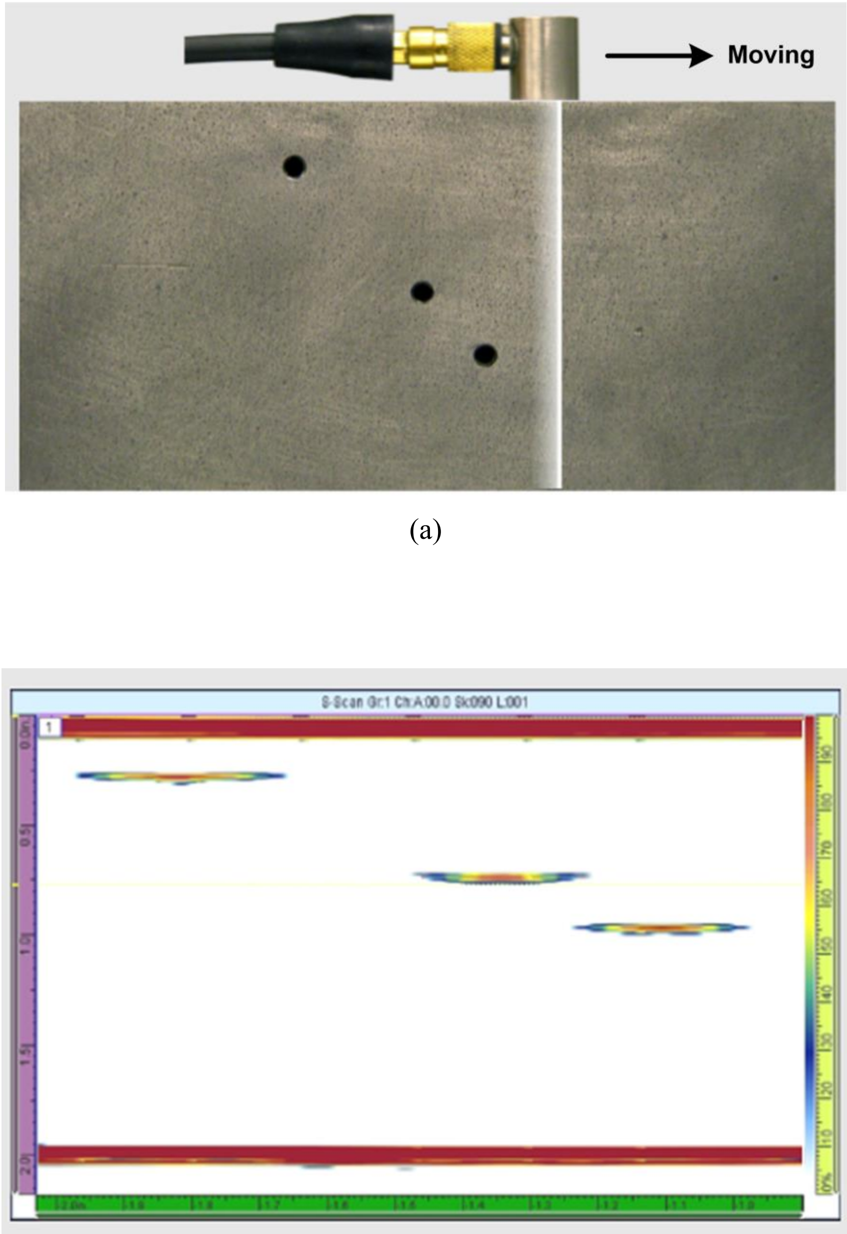

(a)

(b)

Figure 2.6 (a) B-scan with a single-element probe; and (b) B-scan result with a single-element probe [61].

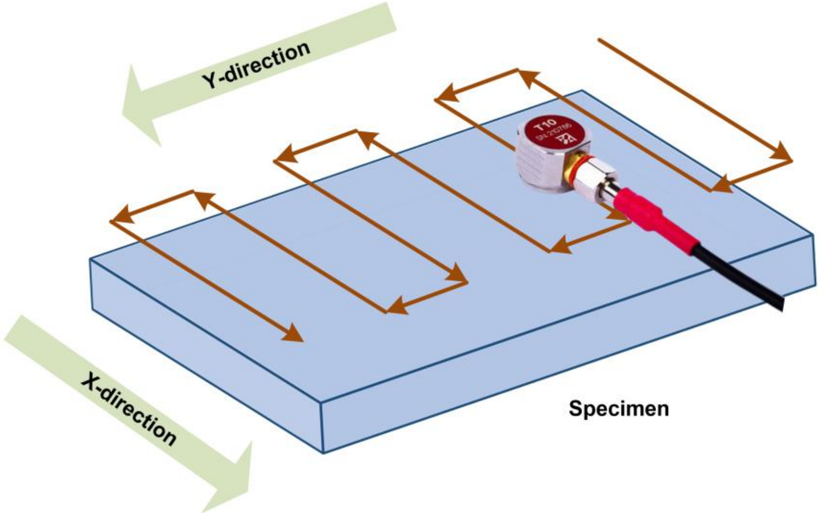

(a)

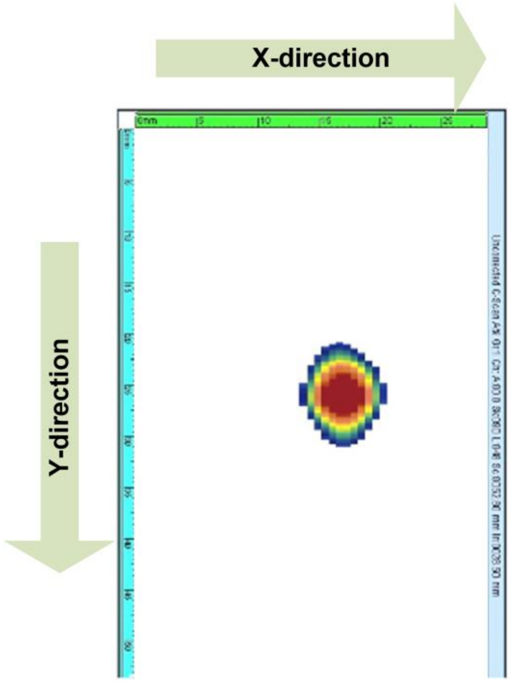

(b)

Figure 2.7 (a) C-scan with a single-element probe; and (b) C-scan result with a single-element probe [62].

Extending the above-discussed scanning using a single probe to the case using a phased array that consists of a multitude of transducer elements, each element can be individually fired to excite and receive ultrasonic waves. Such a merit remarkably simplifies the implementation of the B-scan by automatically activating each element without manually moving the array, as shown in **Figure 2.8**. Furthermore, C-scan can be also conveniently implemented by moving the array along a straight line, **Figure 2.9**.

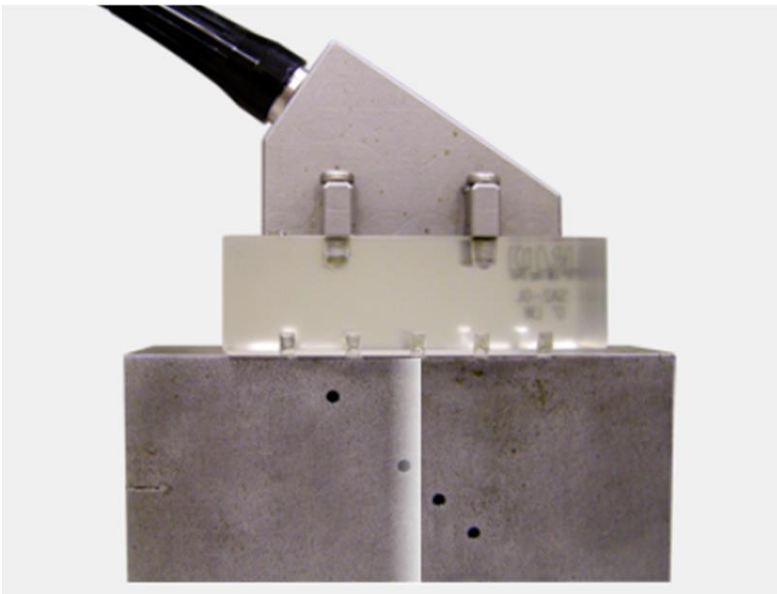

(a)

(b)

Figure 2.8 (a) B-scan with a phased array probe; and (b) B-scan result with a phased array probe [63].

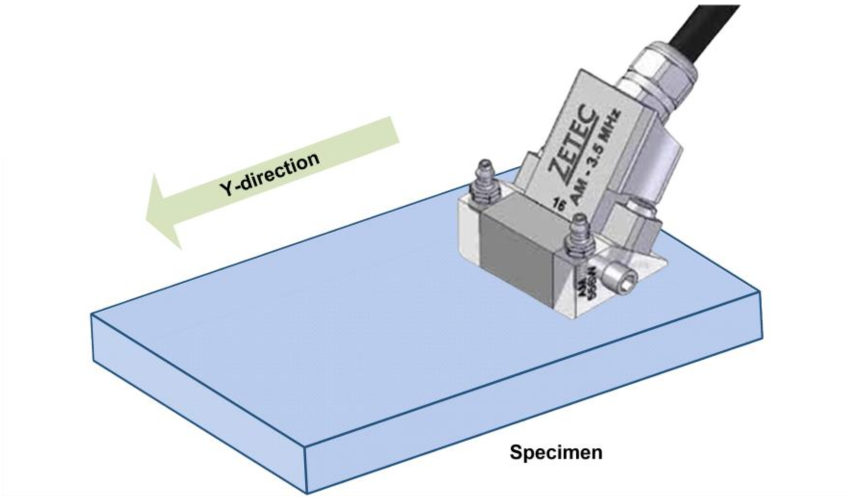

(a)

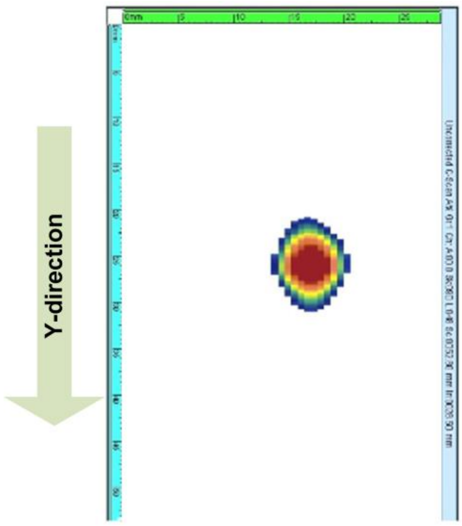

(b)

Figure 2.9 (a) C-scan with a phased array probe; and (b) C-scan result with a phased array probe [64].

Apart from the aforementioned scanning patterns relying on single-input mode (*i.e.*, only one element is activated at a measurement), one of the most attractive advantages of the phased array is that elements in the phased array can be sequentially activated with programmable time delays. As a result of the time delays, phase differences in the wavefronts activated by individual array elements are created. Therefore, the resulting wave, as the synchronization of these waves, is displayed as beamforming. With appropriate adjustment of the time delays, the beamforming can have strong directionality, endowing the phased array with various scanning patterns, representatively as linear scan, sectorial scan, and beam focusing scan [65-69].

In the linear scan, elements in a group are activated with the same time delay, forming a straight wave beam perpendicular to the inspected surface. After sequentially activating sensing groups in a phased array, a full image of the inspection structure can be reconstructed, as illustrated in **Figure 2.10(a)**. This scanning pattern is similar to the B-scan, but linear scan beamforming uses a group of elements, instead of a single element, to activate and receive wave signals, which can enhance the signal-to-noise ratio (SNR) and resolution. Moreover, with the assistance of wedges, the linear scan can be implemented at a fixed angle, allowing to detect wide structures, such as welds.

Sectorial scans commonly alter the time delay of all elements to sweep the beamform through a series of angles, featuring the rapid inspection without moving the array, shown in **Figure 2.10(b)**. The sectorial scan is typically applied in inaccessible structures, like the turbine and blade root. Depending primarily on the array frequency and the element spacing, the sweep angles can vary from ±20° up to ±80°.

Provided the time delay of elements is appropriately selected to meet the spherical timing relationship, the beam focusing scan can be implemented, in which the wave beam is focused at a special point, **Figure 2.10(c)**. Since the focusing point has the narrowest wave beam and the greatest lateral resolution, the beam focusing scan commonly outperforms other scanning patterns in terms of imaging sensitivity and resolution.

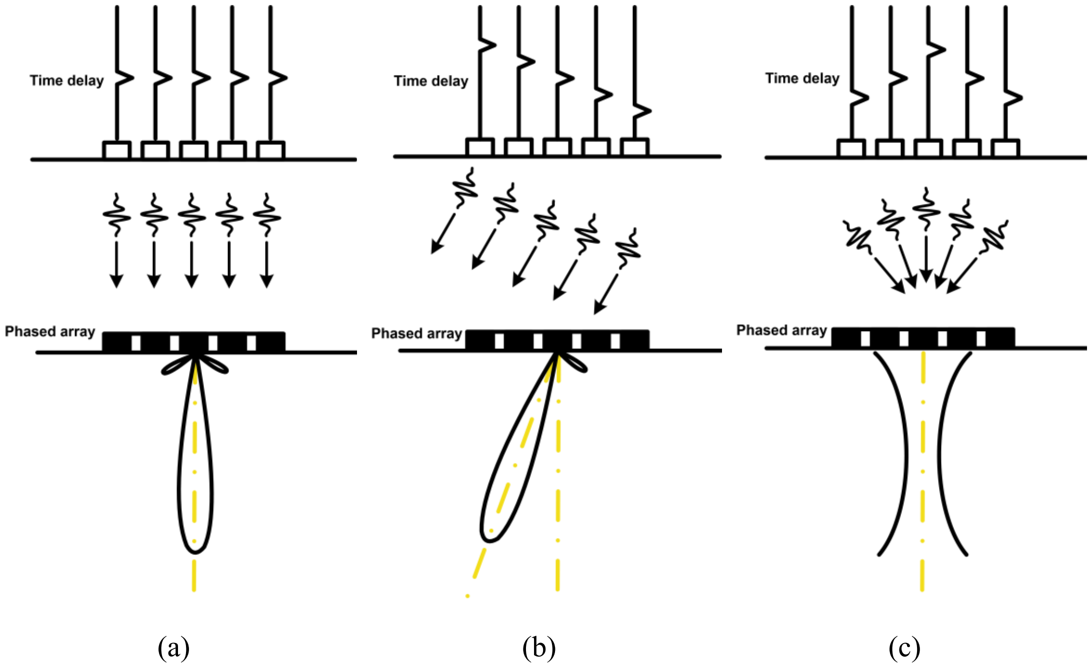

Figure 2.10 Scanning patterns of the phased array with different time delays: (a) linear scan; (b) sectorial scan; and (c) beam focusing scan [70].

However, in scanning-based imaging, different time delays need to be appropriately programmed for each scanning direction or each focused point, and this unavoidably requires burdensome work and incurs high time consumption. In addition, scanning-based imaging commonly displays imaging results in a direct manner, which is poor to exploit rich damage information in the captured wave signals. To circumvent these problems, two representative post-processing imaging approaches, delay-and-sum-based imaging and inversion-based imaging, have been developed to carry out data analysis of phased array signals, which are briefly introduced in Sections 2.2.3 and 2.2.4, respectively.

2.2.3 Delay-and-sum-based Imaging

The basic principle of delay-and-sum-based imaging is to construct the diagnostic image by weighting the sum of amplitude contributions from all received signals at pixel points. In general, delay-and-sum-based imaging requires a large number of received signals to ensure accuracy and precision of damage identification results, and such a requirement can be fulfilled by the phased array that consists of dense transducer elements. Therefore, delay-and-sum-based imaging is widely applied in the field of phased array-based damage identification and has been implemented in various modalities including synthetic aperture focusing technique (SAFT), TFM, wavenumber algorithm, plane wave imaging (PWI) method, phase coherence imaging (PCI) method.

The SAFT was originally developed as a single ultrasonic probe-based imaging technique, which collected pulse-echo signals at a series of points along the sample surface. This type of data collection procedure can be implemented using a phased array with N transducer elements, **Figure 2.11**, in which each element is employed in turn for wave activation and reception, rendering a total of N wave signals. Defining the wave signal activated and received by the m^{th} element at the position $(x_m, 0)$ as $u(x_m, t)$, the SAFT imaging value, $P(x,z)$, at pixel point (x, z) is performed as

$$P(x,z) = \sum_{m=1}^{N} u(x_m, \frac{2L_m}{c}) , \tag{2.3}$$

where $L_m = \sqrt{(x_m - x)^2 + z^2}$ the distance between the m^{th} element and the pixel point, and c is the wave velocity.

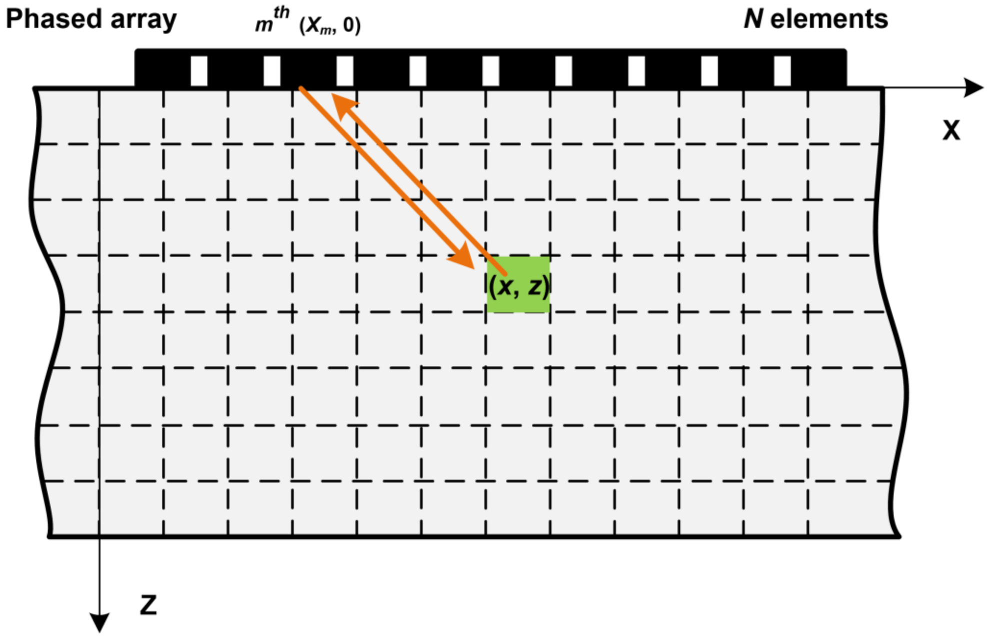

Figure 2.11 SAFT image formation process [43].

Several representative studies in the SAFT field are presented here. Karaman *et al.* [71] built a theoretical framework of the SAFT and discussed factors related to imaging quality. Martinez *et al.* [72] developed a digital signal processing procedure including apodization, deconvolution, dynamic focusing, and envelope detection, to improve the accuracy of the SAFT image. Chahbaz *et al.* [73] compared the scanning-based imaging and the SAFT-based imaging, concluding that SAFT could provide better reconstruction results with higher SNR and spatial resolution. Stepinski *et al.* [74] proposed a wavenumber SAFT algorithm that implemented the SAFT in the wavenumber domain, rather than in the time domain, by which the image resolution was improved and the grating lobes were lower. Skjelvareid *et al.*[75] combined the SAFT with the virtual source method, which enlarged the focusing range of cylindrical scanning.

However, in SAFT, the wave activation and reception are implemented using the same element, which fails to fully exploit the advantages of the phased array that can simultaneously record pulse-echo signals using all elements in the array. To tackle this deficiency, TFM was developed by Holmes *et al.* [18] to utilize all possible transmit-receive combinations of phased array elements. Consider that a phased array with N transducer elements is placed on the sample surface, **Figure 2.12**. Upon firing each element in turn and recording the received signal by all elements, the signals dataset of all transmitter-receiver pairs is collected, consisting of a total of $N \times N$ signals, termed FMC data. For the convenience of discussion in what follows, the signal transmitted from the m^{th} element at the position $(x_m, 0)$ and then received from the n^{th} element at the position $(x_n, 0)$ is defined as $u(x_m, x_n, t)$. The TFM image value, $P(x, z)$, at pixel point (x, z) is given as:

$$P(x,z) = \sum_{m=1}^{N}\sum_{n=1}^{N} u(x_m, x_n, \frac{L_{m-xz-n}}{c}), \tag{2.4}$$

where $L_{m-xz-n} = \sqrt{(x_m - x)^2 + {z_m}^2} + \sqrt{(x_n - x)^2 + {z_n}^2}$ is the distance from the m^{th} element to the pixel point (x, z) and then to the n^{th} element. Equation (2.4) is the mathematical expression of TFM, in which all transmitter–receiver signals are employed so as to achieve the maximum utilization of information at each point.

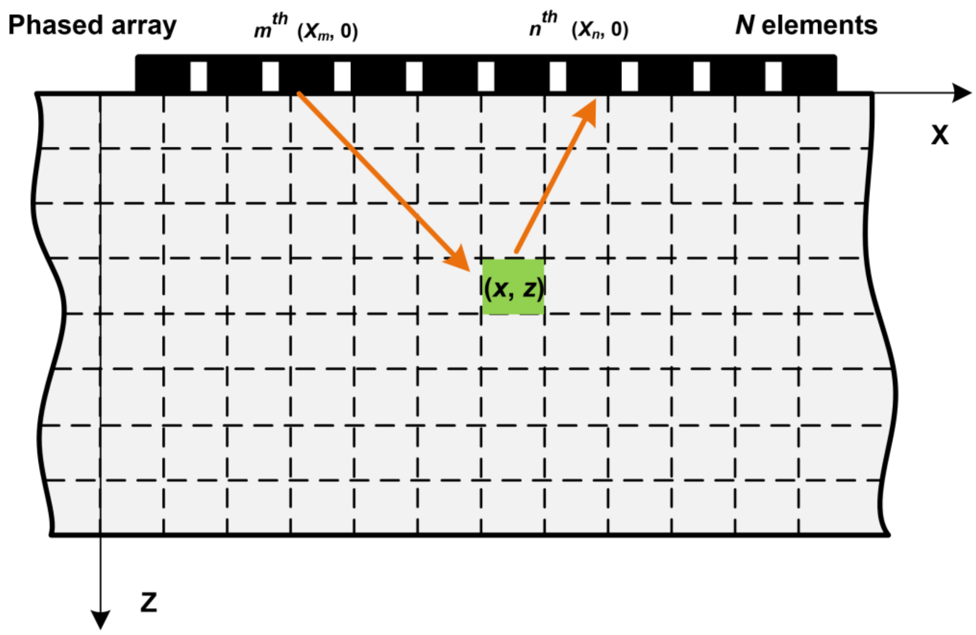

Figure 2.12 TFM image formation process [43].

Based on this study, various modalities of the TFM have been developed. Paul *et al.* [76, 77] proposed the vector TFM (VTFM) algorithm by subdividing the phased array into equal-sized sub-arrays and weighting angular reflectivity characteristics to TFM results of all sub-arrays, via which the orientation of small damage could be determined and visualized. Felice *et al.* [78] considered the wave path that reflected from the back surface of a sample to the damage, and presented the Half-Skip TFM (HSTFM), thereby characterizing small surface-breaking cracks. Extending Felice's method, the Full-Skip TFM (FSTFM) [79] was developed by introducing the wave propagation path that both transmission and reception include one reflected ray from the back surface. Upon fusing the information obtained from the TFM, FSTFM, and HSTFM, multi-view TFM (MTFM) [80] and combined TFM (CTFM) [81, 82] were developed to fully extract the signal features for damage identification. Taking mode conversions between longitudinal waves and transverse waves into account, Zhang *et al.* [83] proposed a multi-mode TFM, showing proven capability of localizing flaw in a multi-layered structure. P. Masson *et al.* [84] presented an Excitelet imaging approach by calculating the correlation between measured signals and theoretical TFM signals, endowing it with the capability of reducing the number of required transducers without loss of imaging quality.

Attempting to focus FMC data at each image pixel, the wavenumber algorithm was developed [85]. In the wavenumber algorithm, a mathematically rigorous solution is deducted for the wave propagation model in the wavenumber domain, instead of the time domain, achieving better image quality and superior computational performance.

Derived from the medical imaging technique, the PWI method [86] was developed, in which plane ultrasonic wavefronts were transmitted at different angles and the image was reconstructed by dynamically focusing with a subset of adjacent elements. In comparison with the TFM, the PWI method requires fewer wave signals and provides higher image resolution [87].

Jorge Camacho *et al.* [88] presented the PCI method by analyzing the phase diversity at the aperture data, which weighted the coherent sum output with the phase coherence factor (PCF) and the sign coherence factor (SCF) to suppress the side lobes in ultrasound images.

2.2.4 Inversion-based Imaging

The reciprocity of the wave propagation states that the received waves after time-reversal could converge at the source point if time is going backward. Based on this philosophy, inversion-based imaging has been intensively developed in recent years, represented by inverse wavefield extrapolation (IWEX), time-reversal (TR) mirror, decomposition of the time-reversal operator (DORT), scattering matrix-based imaging, topological imaging, and RTM.

Portzgen *et al.* [89] proposed the IWEX approach based on the acoustic wavefield theory, with which inverse wavefields were extrapolated and focused on the damage position. Similar to TFM, the IWEX approach was developed in conjunction with Half-Skip and Full-Skip to enhance the capability of detecting corrosion and cracks [90, 91].

TR mirror was developed to refocus received waves on the defect position. Fink *et al.* [92, 93] contributed the fundamental theory of the TR mirror, in which mathematical principles and operating procedures were detailed. Rodríguez *et al.* [94] presented a model-based TR mirror to solve the inverse problem in a high-efficiency way. Jeong [95] extended the TR mirror to the anisotropic media using a modular Gaussian beam (MGB) model.

As an extension of the TR mirror, the DORT method is developed, which constructs the response matrix of the medium and decomposes the TR operator to determine the TR invariants, rather than directly calculates the iterative process. Prada *et al.* [96] compared the performance of the TR mirror and DORT method, concluding that the TR mirror could accurately control wave focusing to reduce the speckle noise, while the DORT method could detect and separate multiple damage sites without the need for programmable generators. Nguyen *et al.* [97] defined two significant singular values corresponding to monopole and dipole mode in the anisotropic medium respectively, whereby extending the DORT method to characterize the small scatterer.

Villaverde *et al.* [98] combined the DORT method with the synthetic transmit aperture (STA) imaging to inspect coarse-grained steel. Cunningham *et al.* [99] developed an enhanced DORT method, which utilised the singular value decomposition of the time-frequency domain response matrices to detect welds.

The scattering coefficient matrix, as a function of incident and scattering angles, can be used to represent the damage scattering field that stores the scattering amplitude and phase information of the scatterer. Motivated by this, the scattering matrix-based imaging method has attracted intensive research efforts for damage identification. Respectively, Zhang *et al.* [100] built the scattering coefficient matrix databases using finite element method (FEM) simulations and identified the damage characterization by comparing the experimental scattering coefficient matrix with simulation databases. Bai *et al.* [101] extended Zhang's method by introducing the correlation coefficient and the structural similarity index, which quantitatively evaluated the similarity between the scattering matrices of the inspected defect and those of reference cracks. Another successful application of the scattering matrix-based imaging was proposed by Cunningham [102], in which the relationship between sizes of cracks and maximum eigenvalues of crack scattering matrices were constructed on the basis of the Kirchhoff scattering model, bringing advantages of no requirement of scattering matrices databases and the ability to detect the small crack.

Topological imaging is a novel inversion-based algorithm. Dominguez *et al.* [103] first established the topological gradient method to identify the position and shape of scatterers. This method was aimed at minimizing the topological gradient function to find the optimal adequation between the measuring signals and FMC data. Based on a similar idea, the full waveform inversion method was developed by Seidl *et al.* [104, 105], which iteratively adjusted the parameters of the simulation model to match the measured signals of the flawed specimen.

RTM, originating from seismic imaging, has consolidated its popularity in ultrasonic imaging in recent years. The RTM-based imaging is manipulated with a postulation that when a receiver wavefield is propagated backward from the receiver in the time domain, the wave components reflected from the internal damage will, in principle, focus at the location of the damage. Representatively, Muller *et al.* [20] applied the RTM to image hidden scatterers in civil structures. Gao *et al.* [106] combined the TR algorithm with RTM, via which internal damage in a multi-layered medium was accurately visualized. Asadollahi *et al.* [107] presented an analytical RTM approach, in which the source and receiver wavefields were approximately calculated to improve computational efficiency. Rao *et al.* [108] developed elastic reverse time migration using a two-way elastic wave propagation equation, to image notches with irregular shapes.

Although bulk wave-based imaging methods discussed in this section have demonstrated effectiveness in various applications, two main problematic issues are remaining for exploration: first, the lower surface of the embedded scatterer is inadequately characterized, leading to inferior imaging quality of full features of the scatterer. Second, the prevailing imaging algorithms have proven capacity of inspecting a specimen with a flat surface, and it is a challenge to detect specimens with non-planar surfaces.

2.3 Guided Wave-based Imaging Using Sensor Networks

2.3.1 Fundamentals of Guided Wave-based Imaging

In a bounded medium, propagation of elastic waves is guided by waveguide boundaries, and elastic waves in this case are known as guided waves. Depending on different boundary conditions, guided waves take a variety of modalities, typically as Rayleigh waves, Lamb waves, and Stoneley waves [109]. Amongst them, Lamb waves, propagating in thin plate- or shell-like structures, have been at the core of intensive efforts since the late 1980s and offered an effective avenue for damage identification [110], which features superb characteristics include: i) capability of rapidly inspecting a large area; ii) superior sensitivity to various types of damage; iii) ability to examine inaccessible structural components; and iv) great potential for online and *in-situ* monitoring.

To provide a basis for Lamb wave-based damage detection, fundamentals of Lamb waves are recapped here briefly. In a thin isotropic plate, the governing equation of motion of elastic disturbance can be represented in the form of Cartesian tensor notation. Using the Helmholtz decomposition [111], the Lamb waves can be decomposed into two uncoupled parts, longitudinal waves and transverse waves, respectively. After applying boundary conditions at both the upper and lower surfaces, the general description of Lamb waves can be obtained as [112]:

$$\frac{\tan(qh)}{\tan(ph)} = -\frac{4k^2qp}{(k^2-q^2)^2} \quad \text{(symmetric modes)}, \tag{2.5a}$$

$$\frac{\tan(qh)}{\tan(ph)} = -\frac{(k^2 - q^2)^2}{4k^2 qp} \quad \text{(antisymmetric modes)}, \tag{2.5b}$$

where $p^2 = \frac{\omega^2}{{c_L}^2} - k^2$, $q^2 = \frac{\omega^2}{{c_T}^2} - k^2$ and $k = \frac{2\pi}{\lambda}$. h is the half thickness of the plate, k, ω, and λ are the wavenumber, angular frequency, and wavelength. Equations (2.5a) and (2.5b) are collectively known as the Rayleigh-Lamb equations, which implies that Lamb waves consist of symmetric and anti-symmetric modes. Each type of modes has an infinite number of modes and can be symbolized as S_i and A_i respectively (i = 0, 1, 2, …namely the order of Lamb waves).

In guided wave-based damage identification, a multitude of spatially distributed sensors is usually networked to configure a sensor network. By 'cooperating' with each other, the sensor network can certainly provide adequate wave signals, thereby increasing detection confidence and minimizing dependence on the isolated actuator-sensor path [113, 114]. With adequate wave signals captured by a sensor network, it is crucial to extract and fuse the damage information extracted from these signals, and therefore various diagnostic imaging algorithms have been developed, including tomography imaging, time-of-flight-based imaging, time-reversal imaging, probability-based diagnostic imaging, and array signal processing-based imaging to name a few.

2.3.2 Tomography Imaging

The principle of guided wave-based tomography imaging lies in that a guided wave passes more easily through the intact structure whereas it is somewhat blocked by damage, if any. If these abnormal features in waves are extracted and quantified, the damage could be highlighted in the reconstructed image via appropriate imaging algorithms. In practice, guided wave-based tomography can be conducted following certain basic steps:

i) meshing the inspected area into small cells (called grid cells);

ii) extracting the feature of the signal received by an actuator-sensor pair in a sensor network as the sum of contributions from all cells that lie on the straight line (called a ray) of the actuator-sensor path;

iii) using appropriate algorithms to establish the field value at each grid cell based on signal features extracted in step ii);

iv) repeating steps ii) and iii) for all the available rays in a sensor network, and fusing field values as the final tomogram.

Following the above procedure, various guided wave-based tomography methods have been developed. Hutchins *et al.* [115, 116] made a substantial contribution to the early development of tomography, which utilized changes in wave velocity and attenuation of wave signals to reconstruct tomograms. Malyarenko *et al.* [117] introduced two major schemes for implementing guided wave tomography, namely parallel beam projection and crosshole scheme, as illustrated in **Figure 2.13**. Parallel beam projection employed one actuator-sensor pair and inspected the object by rotating the object with a very tiny angular; while in crosshole projection, a large number of transducers were fixed surrounding the object to form multiple actuator-sensor pairs for tomographic reconstruction. To take the multi-mode characteristics of Lamb waves into account, Hinders *et al.* [118] developed the multi-mode tomography in conjunction with the arrival time sorting algorithm, whereby to improve the identification precision in pipes and plates. Xu *et al.* [119] established an ellipse-based corrosion damage model for Lamb wave tomography, by which the shape and orientation of corrosion could be efficiently detected. Belanger *et al.* [120] developed a novel diffraction tomography algorithm based on the Born approximation, applicable for thickness reconstruction of plates or pipes. To facilitate tomography imaging under varying environmental conditions, G. Park *et al.* [121] presented a relative baseline approach on the basis of cross-correlation and power spectral density analysis, endowing it with the capability of reducing the effects of environment condition changes and quantifying structural damage. Zhao *et al.* [122] compared some typical tomographic imaging techniques, drawing the conclusion that algebraic reconstruction technique (ART) performed better than filtered back projection (FBP) in terms of noise tolerance and datasets handling, while probabilistic reconstruction algorithm (PRA) benefited flexibility of array scheme selection and efficiency of reconstruction. This research also discussed the sensor array geometries, finding that the rectangular array featured higher precision while the square sensor array was more cost-effective.

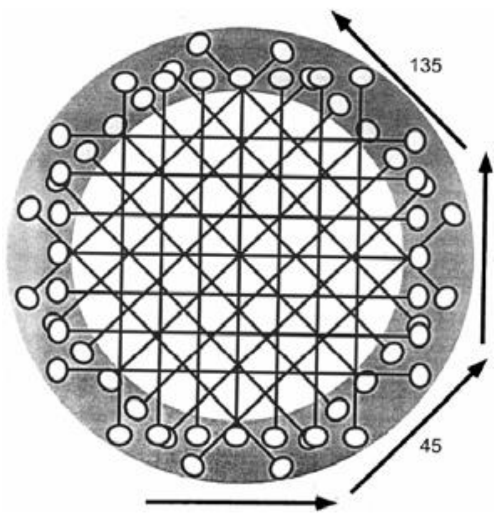

(a)

Figure 2.13 Schemes of Lamb wave tomography: (a) parallel projection scheme; and (b) crosshole scheme [123].

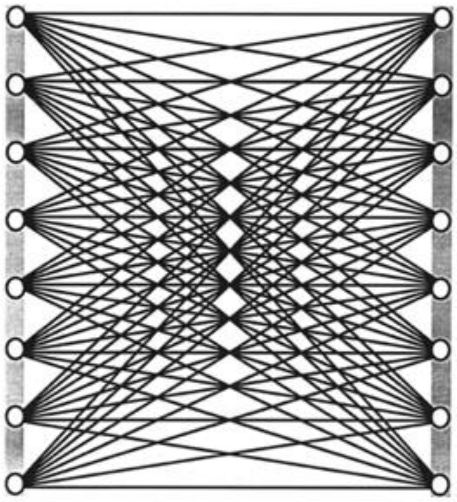

(b)

Figure 2.13 *Cont.*

Despite demonstrated effectiveness in numerous applications, tomography imaging still suffers from the requirement of a large number of rays in order to cover the entire inspection area, which heavily increases the operation time and fairly narrows the application fields.

2.3.3 Time-of-flight-based Imaging

ToF, defined as the time consumed for a wave to travel a certain distance, is one of the most straightforward signal features, which suggests the relative positions among the actuator, receiver and damage. Upon extracting ToFs from a certain number of signals captured by a sensor network and applying proper imaging algorithms, damage can accordingly be identified [124-126].

To facilitate comprehension, the ToF-based imaging algorithm is briefly introduced using a scenario consisting of one actuator and two sensors, as shown in **Figure 2.14**.

In this scenario, the incident wave activated by the actuator is scattered by the damage, and then captured by two sensors sequentially.

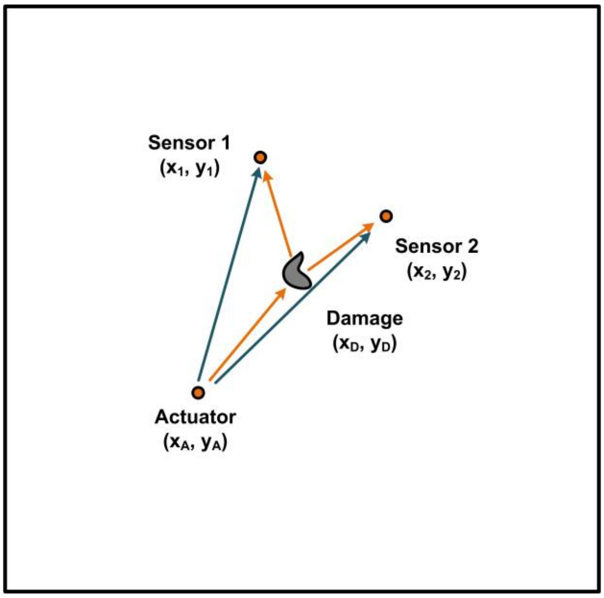

Figure 2.14 Schematic of a two-dimensional plate with one actuator and two sensors [127].

For an actuator-sensor pair, the time difference, Δt_{i-j}, between the incident wave that the sensor first captures and the wave scattered by damage can be expressed as

$$t_{A-D-S_i} - t_{A-S_i} = \frac{L_{A-D} + L_{D-S_i}}{c} - \frac{L_{A-S_i}}{c} = \Delta t \quad (i, = 1, 2), \tag{2.6}$$

where $L_{A-D} = \sqrt{(x_D - x_A)^2 + (y_D - y_A)^2}$, $L_{D-S_i} = \sqrt{(x_D - x_{S_i})^2 + (y_D - y_{S_i})^2}$, $L_{A-S_i} = \sqrt{(x_{S_i} - x_A)^2 + (y_{S_i} - y_A)^2}$, (x_A, y_A), (x_{S_i}, y_{S_i}) and (x_D, y_D) are the locations of the actuator A, sensor S_j and damage D, and c is wave velocity. Equation (2.6) configures the locus of possible damage locations as an ellipse with the actuator and sensor being its two foci, as shown in **Figure 2.15**.

Allowing for two sensing paths, the difference in the ToFs between these two actuator-sensor pairs can be expressed as

$$t_{A-D-S_1} - t_{A-D-S_2} = \frac{L_{D-S_1}}{c} - \frac{L_{D-S_2}}{c} = \Delta t_{1-2} \,, \tag{2.7}$$

where L_{D-S_1} and L_{D-S_2} are the distances from the damage to sensor S_1 and from the damage to sensor S_2, respectively. Mathematically, the locus defined by Equation (2.7) is a hyperbola with two sensors being its two foci and suggests possible damage locations. With Equations (2.6) and (2.7), damage positions can be determined by seeking intersections of these spatial loci (ellipses or hyperbolae), as shown in **Figure 2.15**.

The above discussion can practically be expanded to the sensor network consisting of *N* lead zirconate titanate (PZT) wafers (each can function as both the actuator and the sensor).

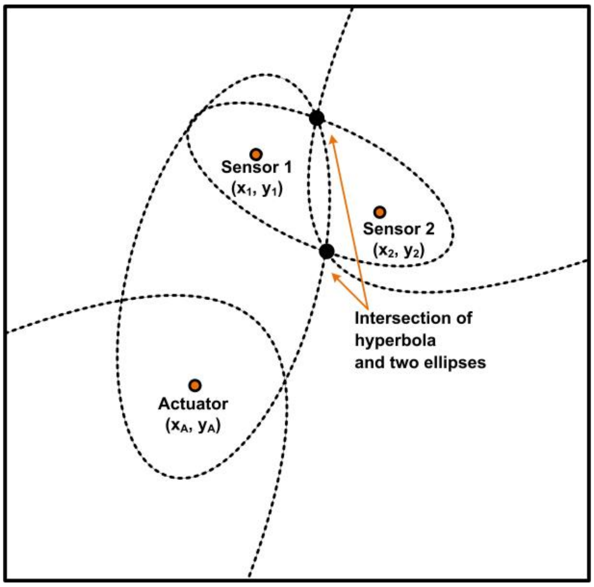

Figure 2.15 ToF-based imaging of damage in a two-dimensional plate with one actuator and two sensors [127].

Using such a philosophy, ToF-based imaging methods have been developed and implemented for various damage scenarios. Tua *et al.* [128] detailed the procedure of the ToF-based imaging, and detected cracks damage by seeking intersections of ellipses. Croxford *et al.* [129] compared the ellipse-based method and hyperbola-based method, concluding that the overall performance of the two methods was similar, while when a small number of sensors was arranged, the hyperbola-based method was superior with higher SNR. Fendzi *et al.* [130] combined the Bayesian analysis with ToF-based imaging, to improve localization accuracy of the impact to a sandwich plate. Moll *et al.* [131] extended the ellipse-based method by amending the wave propagation velocity via an angle-dependent profile, endowing it with the capability of localizing multiple damage sites in the anisotropic plate.

In the above studies, the accuracy of ToF extraction plays a dominant role in ToF-based imaging, but mode conversion and boundary reflection are some factors that can complicate ToF extraction. To this end, appropriate signal processing tools, such as the short-time Fourier transform (STFT), Hilbert transform and wavelet analysis, are often employed to improve the performance of ToF-based imaging [132, 133].

2.3.4 Time-reversal Imaging

Time-reversal imaging is developed based on the principle of time reversibility of acoustic waves. Specifically, in an intact structure, received wave signals can be reconstructed at the original activation source with a time-reversal process (TRP), while if any damage exists on the wave propagation path, the time reversibility of acoustic waves would break down. Therefore, examining the discrepancies between the reconstructed wave signal and the original incident signal can indicate the presence of damage without requiring the baseline signal [134, 135].

The above principle can be better understood using an example, in which two Lamb wave signals acquired in an aluminum plate with/without damage are reconstructed using TRP, as shown in **Figures 2.16(a)** and **(b)**, respectively. It can be seen that due to the presence of damage, a large discrepancy between the reconstructed signal and the original incident signal is clearly evident in **Figure 2.16(b)**, resulting in a much higher DI (*i.e.*, the signal discrepancy between the reconstructed signal and the original incident signal in this example).

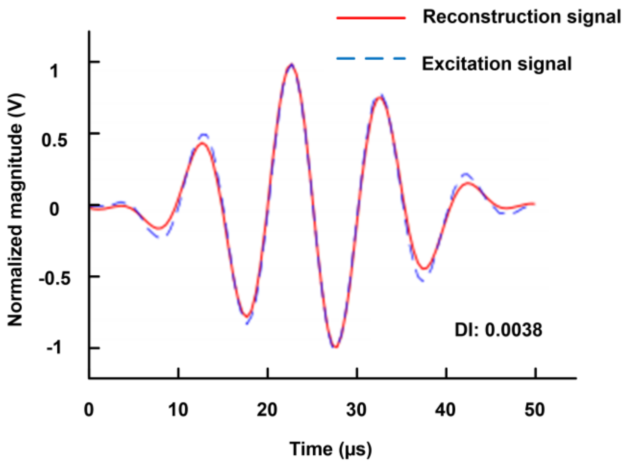

(a)

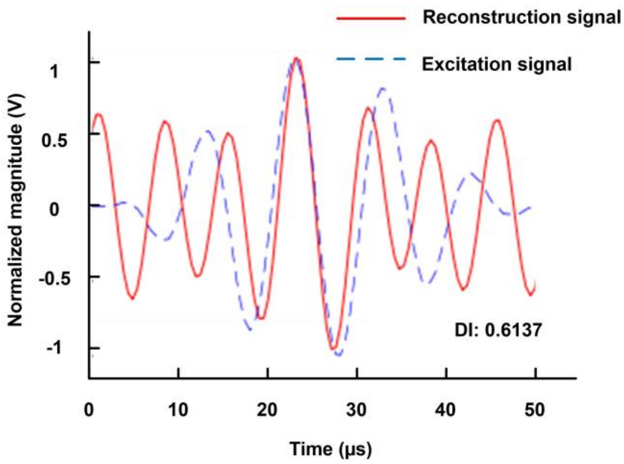

(b)

Figure 2.16 Reconstructed wave signals: (a) without damage; and (b) with damage [136].

This example also shows two key tasks in time-reversal imaging: the reconstruction of received signals and the calibration of deviation. To investigate these aspects, a number of studies have been reported. Park *et al.* [137] theoretically interpreted the TRP of Lamb waves and discussed factors in the TRP including velocity, dispersion, modes and boundary reflection. Xu and Giurgiutiu [138] developed a new theoretical model to analyze the TRP, concluding that Lamb waves could be rigorously time reversible under narrow-band tone burst excitation. Agrahari *et al.* [139] investigated the frequency tuning of time reversibility, finding that the best reconstruction did not occur at the sweet spot frequency of the single-mode excitation, which could be influenced by parameters including transducer size and thickness, number of tone bursts and plate thickness. Wang *et al.* [136] proposed a virtual time reversal (VTR) algorithm in conjunction with the air-coupled scan method, whereby reducing the hardware manipulation of TRP and achieving better waveform reconstruction.

2.3.5 Probability-based Diagnostic Imaging

Compared with the definitive identification results, the underlying implication of probability is more consistent with the implication of estimating damage [140, 141]. Based on such a philosophy, probability-based diagnostic imaging (PDI) has been intensively studied. In PDI, the distribution probability of damage can be calculated with an appropriate DI extracted from captured guided wave signals (*e.g.*, ToF, signal magnitude, and signal correlation) and finally displayed in a greyscale image.

ToF-based PDI in virtue of the ToF discussed in Sections 2.3.3 configures the locus of damage locations as an ellipse or a hyperbola, and calculates the probability of the presence of damage at a specific pixel according to the shortest distance between this pixel and the locus. Signal magnitude-based PDI (also called the delay-and-sum method) relies on the fact that the existence of damage leads to the presence of an additional wave packet, namely damage-scattered wave, in the captured wave; therefore, the ToF and strength of damage-scattered wave can be used to reveal the damage. Practically, the damage-scattered wave signals are commonly extracted from captured wave signals by benchmarking the baseline signals, and the PDI can be defined in terms of the superposition of the magnitude of the damage-scattered wave signals that are shifted using a time-shifting rule. Signal correlation-based PDI hypothesizes that a low correlation between signals captured from a damaged structure and from the benchmark structure implies a high probability of damage presence along the signal acquisition path and vice versa. Based on this, the damage can be highlighted by aggregating all actuator-sensor paths with low correlation.

PDI has proven effectiveness for identifying damage in a diversity of case studies. Representatively, Su *et al.* [142] applied ToF-based PDI to detect delamination in carbon-fiber-reinforced epoxy (CF/EP) laminates. Michaels *et al.* [23] proposed a delay-and-sum imaging method to characterize damage in a variable temperature environment. Wang *et al.* [143] developed a signal correlation-based PDI algorithm in conjunction with the use of virtual sensing paths, whereby to predict the location of damage in aluminum plates. Zhou *et al.* [144] presented a hybrid image fusion scheme that fused the various signal features including temporal information, signal energy, and signal correlation, applicable to visualizing structural damage regardless of its shape and number. In addition, in recognition of the fact that the performance of PDI can be significantly influenced by dispersive, multiple modes, frequency bandwidth, and baseline model, some enhanced PDI methods [145-147] were developed to address the above concerns.

2.3.6 Array Signal Processing-based Imaging

Instead of using straightforward wave features such as time-of-flight or signal amplitude, the array signal processing-based imaging commonly makes use of global features of the wave signals to estimate damage characterization, which has been implemented in various modalities, including minimum variance distortionless response method [27], subspace fitting [28], maximum-likelihood method [29], and MUSIC and so on.

In particular, the MUSIC algorithm, with its theoretical framework shaped by Schmit [148] in 1981 for frequency estimation and radio direction finding, is a directional scanning and searching method to unbiasedly estimate signal features in terms of the orthogonal attributes between signal subspace and noise subspace. With a directional scanning ability, MUSIC has been proven effectiveness in guided wave-based damage imaging. Representatively, Stepinski and Engholm [149] are among those first demonstrated the use of the MUSIC algorithm for estimating the direction of arrival (DOA) of an incoming Lamb wave in passive acoustic emission. Yang *et al* [150, 151] accurately determined the direction of impact-induced acoustic waves using MUSIC in conjunction with a linear sensor array, which, however, failed to precisely locate the impact site as the approach is based on the far-field hypothesis by simplifying that the impact-emanated wave is of a plane wavefront when the wave arrives at the array – it is not true for a waveguide in the near-field.

To circumvent this limitation, Zhong *et al* [36] developed a near-field MUSIC algorithm on the basis of the Taylor expansion theory, in which incoming waves are deemed to feature a spherical wavefront. This method was then validated by locating damage in a real composite oil tank, showing potential to improve localization accuracy. Extending this study and also taking into account other impact-induced wave components out of the excitation frequency, Yuan *et al* [37] proposed a single frequency component-based re-estimated MUSIC (SFCBR-MUSIC) with Shannon wavelet transform, showing the proven capability of localizing impact applied on a composite aircraft wing box. Conventional MUSIC was revamped by Zhong *et al* [152] based on 2D near-field assumption and the Gerschgorin discs theorem, and this revamped MUSIC algorithm facilitated detection of multiple damage sites.

In addition to the above passive impact localization, MUSIC-based detection methods have also been extended to active damage identification. Bao *et al* [38] combined transmitter beamforming and weighted imaging with MUSIC, with which the severity of corrosion in aluminum plates was assessed, in conjunction with the use of a dual array consisting of two linear sensor arrays. Zuo *et al* [153] presented a model-based MUSIC algorithm by calculating the cross-correlation function between modeled scattered signals and measured residual signals, for identifying added mass attached to composite laminates, though material anisotropy of the composites and therefore discrepancy in wave velocities along different propagation directions were not considered. As an amendment to this approach, Bao *et al* [154, 155] developed an updated MUSIC algorithm to compensate for the anisotropy, by considering the effect of both the sensor localization error and the sensor phase error due to the material anisotropy, so that damage localization precision can be improved.

Despite demonstrated applications, MUSIC-based damage identification methods are usually restricted to the use of uniform linear arrays featuring a dense configuration of transmitter elements with a sufficiently small and uniform element pitch. This category of methods barely provides full inspection coverage, showing downgraded beamforming capability at azimuth angles close to 0° and 180°, as a result of which damage in the regions of [0, 30°] or [150°, 180°] within the inspection region may be overridden [33]. In addition, prevailing MUSIC-based methods, manipulated in the time domain solely at the monochromatic wave excitation frequency band only, ignore the wave components in the captured signals out of the range of the excitation frequency band which also carries rich information on structural damage or material degradation along wave propagation paths [34], potentially resulting identification errors [156]. Finally, linear sensor arrays in the previous studies are commonly configured by manually aligning a certain number of PZT wafers. Such a means is of a low degree of coupling compatibility with inspection structure and poor inspection reliability due to human interference, let alone extension of offline inspection to continuous monitoring of material deterioration and damage progressing.

2.4 Summary

In brief, this chapter reviews the state of the art of prevailing ultrasonic wave-based diagnostic imaging approaches. Depending on the two basis wave modes of ultrasonic waves, the diagnostic imaging approaches are distinguished by the bulk waves-based and the guided waves-based. In bulk waves-based diagnostic imaging, scanning-based imaging is the most straightforward approach but suffers from the cumbersome operation of moving transducers. Delay-and-sum-based imaging and inversion-based imaging, as post-processing methods, can exploit rich information in the captured signals and therefore enhance imaging precision. Guided waves-based diagnostic imaging is represented as tomography imaging, time-of-flight-based imaging, time-reversal imaging, probability-based diagnostic imaging, and array signal processing-based imaging, each of which is discussed in terms of its applications and limitations. Driven by the state of the art reviewed above, developing the innovative diagnostic imaging framework for ultrasonic wave-driven damage characterization is the main objective of this PhD study.

CHAPTER 3

Enhanced Reverse Time Migration (ERTM) for Damage Characterization and Geometric Profiling Using Phased Array

3.1 Introduction

To implement phased array-based imaging, phased arrays are manipulated on the surface of the inspected sample, to capture signals. However, such an imaging philosophy fails to delineate the lower surface of an embedded flaw (*e.g.,* damage), let alone achieve a detailed depiction of its full features. This deficiency is mainly attributable to the difficulty in making use of the waves scattered from the lower surface of a scatterer. To this end, an ERTM algorithm is developed in this chapter for delineating damage characterization and geometric profiling. In ERTM, a virtual phased array is disposed on the basis of the multipath scattering analysis and Fermat's principle of the acoustic wave propagation, to portray the lower flaw surface. In conjunction with the damage upper surface constructed by the actual phased array, the full features damage can be precisely delineated. The effectiveness of the ERTM algorithm is also verified in both numerical simulations and experimental investigations.

3.2 Principle of Enhanced Reverse Time Migration (ERTM)

Considering a homogeneous solid with two flat parallel surfaces and a hidden scatterer, a phased array with N elements is placed on its upper surface, operating in a two-dimensional scenario, as shown in **Figure 3.1**, where x and z stand for the horizontal dimension and the vertical dimension, respectively. Without losing generality, when a wave is transmitted from the n^{th} element, there are two possible propagation paths of interest related to the scatterer: *Path* 1- the incident wave is reflected directly from the upper surface of the scatterer, and then received by elements in the array; *Path* 2 - the incident wave is reflected by the bottom of solid, scattered from the lower scatterer surface, and then captured by elements in the array. The conventional imaging methods, especially those capitalizing on ToFs and amplitude, take the *Path* 1 into account only and neglect wave components along the *Path* 2 which also carries rich information on the embedded scatterer, resulting in the deficiency in depicting full features of the scatterer. To overcome this bottleneck, the ERTM algorithm is developed in this chapter.

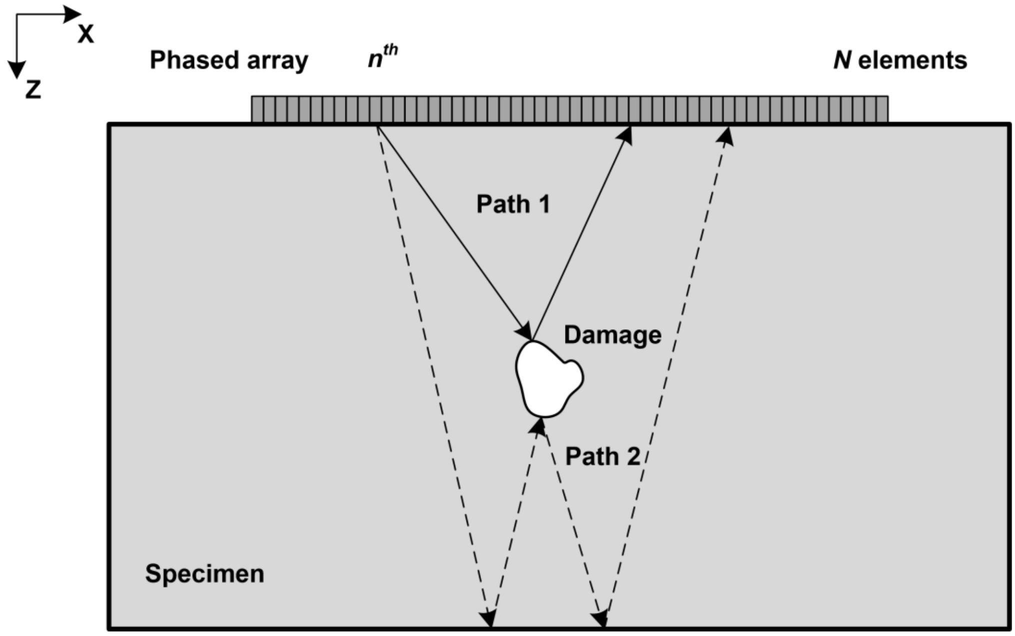

Figure 3.1 Schematic of the wave propagation in the specimen with hidden damage.

Before detailing the ERTM, three premises should be pointed out: i) ERTM, as a post-processing method, is based on the aforementioned FMC data, so it is assumed that FMC data have previously been captured for all damage cases; ii) the wave signals shall be recorded in a sufficiently long duration, ensuring that the multiple reflections from *Path* 2 can be included; and iii) the mode conversion in wave propagation are neglected, due to the weakness in the energy of the converted transverse wave mode, and only the longitudinal wave is investigated.

In recognition of the fact that the ultrasound waves that underwent the multiple scattering *Path* 2 indicate the intensity of lower damage surface, ERTM treats the bottom of the solid specimen as a mirror and creates a virtual phased array that is located symmetrically with regard to the actual array, as shown in **Figure 3.2**. In conjunction with Fermat's principle of the acoustic wave propagation [157], the multiple scattering *Path* 2 could be simplified as the direct scattering path, equivalent to the path that waves are transmitted from the n^{th} element of the virtual phased array, reflected by the lower surface of the damage, and then captured with the virtual phased array. In this way, both the scattering paths 1 and 2 are viewed as the direct scattering paths, which contribute to the construction of the upper damage surface and the lower damage surface, respectively.

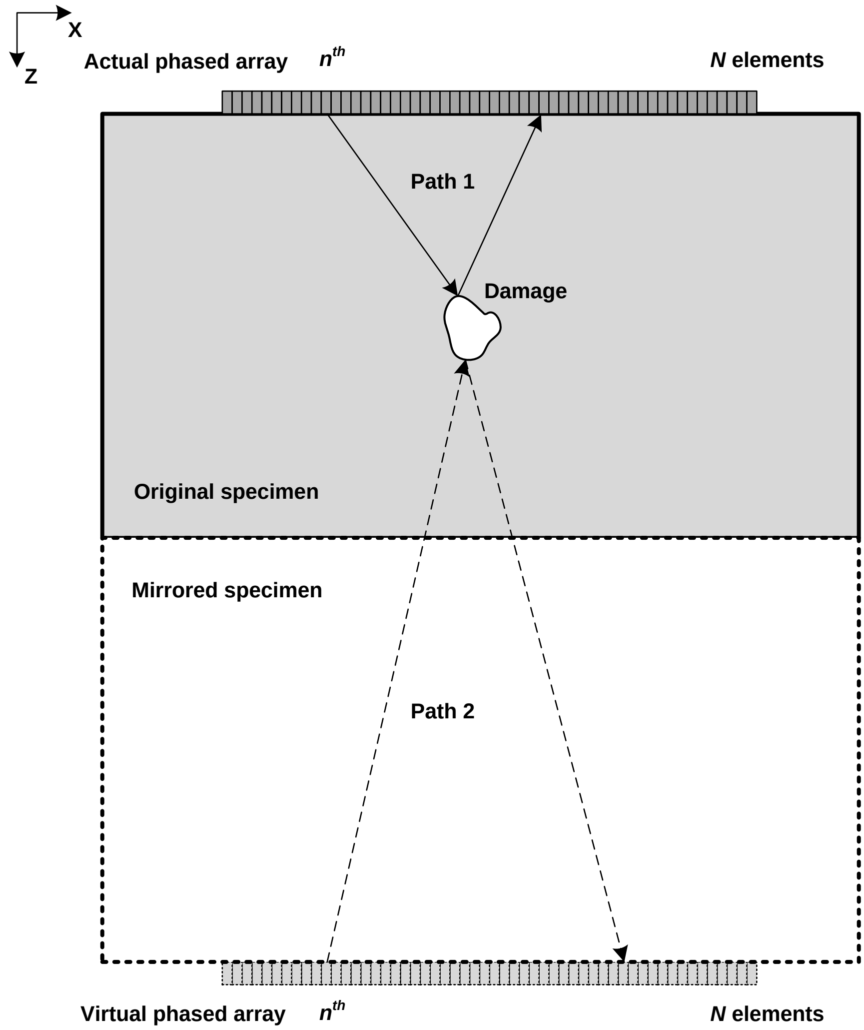

Figure 3.2 Schematic of the wave propagation in the specimen using an actual phased array and a virtual phased array.

Based on this mechanism, a novel model consisting of the original specimen and the mirrored specimen is established, **Figure 3.3**, under the assumption of initial undamaged material, via which a threefold ETRM imaging process is proposed for damage characterization:

(i) *upper scatterer surface*: the actual phased array is employed for the RTM processing. Specifically, the wave signal excited by the n^{th} element in the actual phased array is propagated forward to extrapolate the actual source wavefields $S_n^a(x,z,t), (n=1,2,...,N)$; subsequently, the measured signals are reversed in time and excited at the corresponding locations of all elements in the actual array to extrapolate the actual receiver wavefields $R_n^a(x,z,T-t), (n=1,2,...,N)$.

(ii) *lower scatterer surface*: the RTM processing is applied with the virtual phased array, embracing the following two key steps. First, the virtual source wavefields $S_n^v(x,z,t), (n=1,2,...,N)$ are extrapolated by exciting the n^{th} element in the virtual phased array; Second, the time-reversed signals are excited by the corresponding elements in the virtual phased array to extrapolate the virtual receiver wavefields $R_n^v(x,z,T-t), (n=1,2,...,N)$.

(iii) *image reconstruction*: the image of the specimen is reconstructed by using the zero-lag cross-correlating imaging condition for the source wavefields and the receiver wavefields obtained in steps (i) and (ii), defined as

$$\begin{aligned} I(x,z) &= I_{\text{upper}}(x,z) + I_{\text{lower}}(x,z) \\ &= \sum_{n=1}^{N} \frac{\sum_t S_n^a(x,z,t) R_n^a(x,z,T-t)}{\sum_t S_n^a(x,z,t)^2} + \sum_{n=1}^{N} \frac{\sum_t S_n^v(x,z,t) R_n^v(x,z,T-t)}{\sum_t S_n^v(x,z,t)^2}, \end{aligned} \tag{3.1}$$

where $I_{\text{upper}}(x,z)$ is the pixel value to define the upper surface flaw and $I_{\text{lower}}(x,z)$ to define the lower flaw surface; and $I(x,z)$ is the image value at the pixel (x,z) in the reconstructed image. With Equation (3.1), the full profile of an embedded scatterer can be depicted accurately.

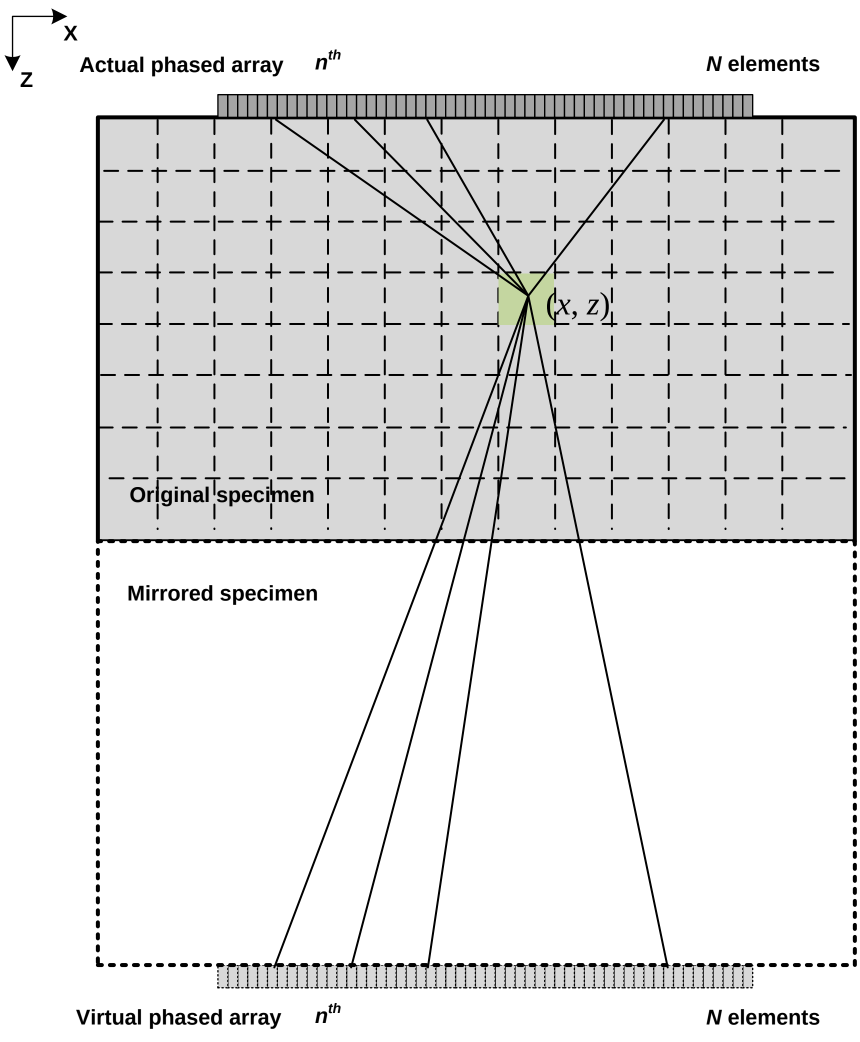

Figure 3.3 Schematic of wavefields extrapolation model.

The computation of source and receiver wavefields is the crucial concern in the ETRM imaging process, which can be solved with numerical techniques including finite elements, finite volumes or finite differences. In this chapter, the finite element method

(FEM) is chosen to provide the solution with the aid of flexible and various calculation modules of commercial software.

3.3 Feasibility Study Using Numerical Simulation

3.3.1 Numerical Model

To verify the performance of the proposed ERTM, numerical simulation is carried out with COMSOL Multiphysics® software. Consider an aluminum sample (longitudinal wave velocity $c_L = 6190$ m/s, density $\rho = 2700$ kg/m^3 and Poisson's ratio $\upsilon = 0.33$) with the size of 50 mm × 20 mm, a phased array with 32 elements is placed on the top surface of the sample. Three damage cases, labelled as C-I – C-III, are created by introducing the flaw with different geometries to the sample, as shown in **Figure 3.4**. The flaw is modeled by enforcing the material local stiffness to be zero. A 1.5-cycle Hann-windowed tone-burst with a central frequency of 5 MHz signal is selected as the excitation signal. By firing each element in turn and recording the received signals with all elements, the FMC data are obtained for all damage cases.

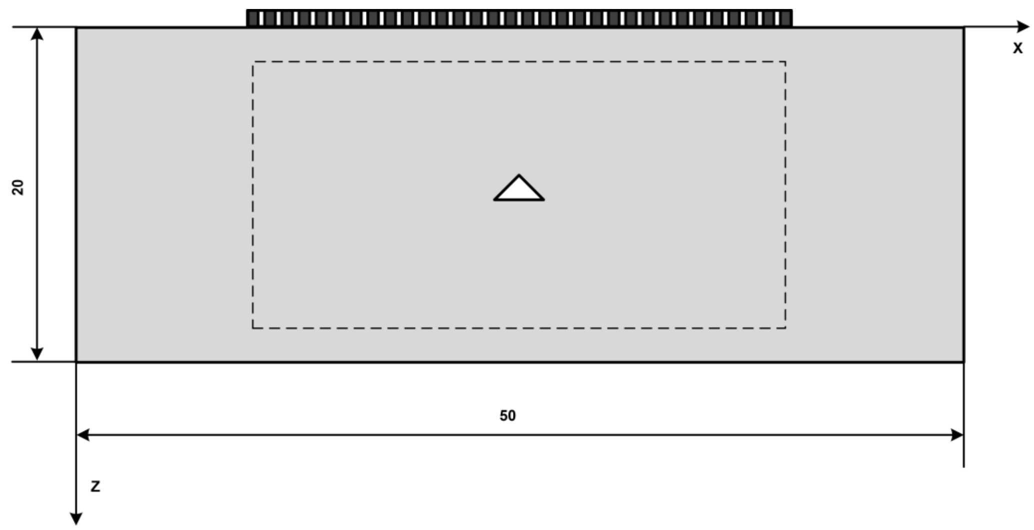

(a)

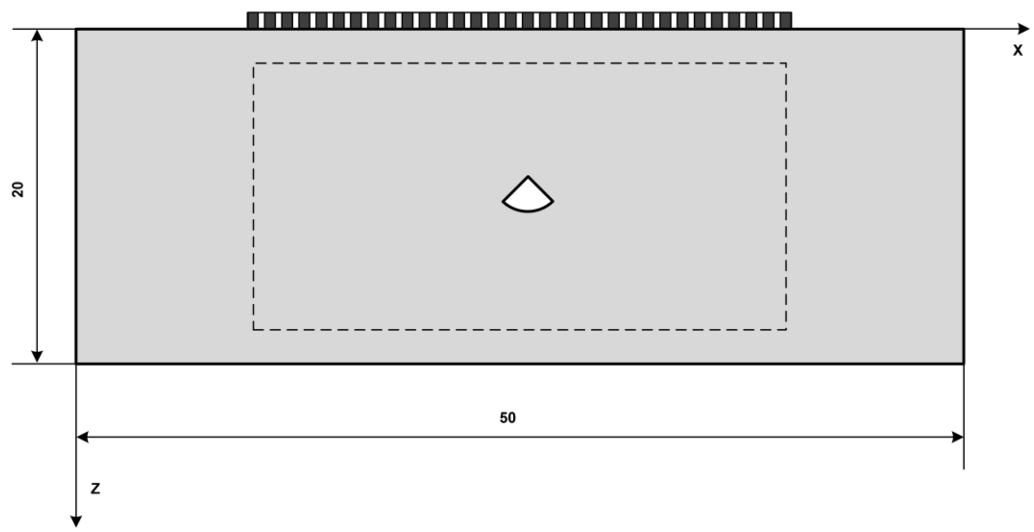

(b)

Figure 3.4 Schematics of 2D models in simulation for damage case (all dimensions in mm): (a) C-I; (b) C-II; and (c) C-III.

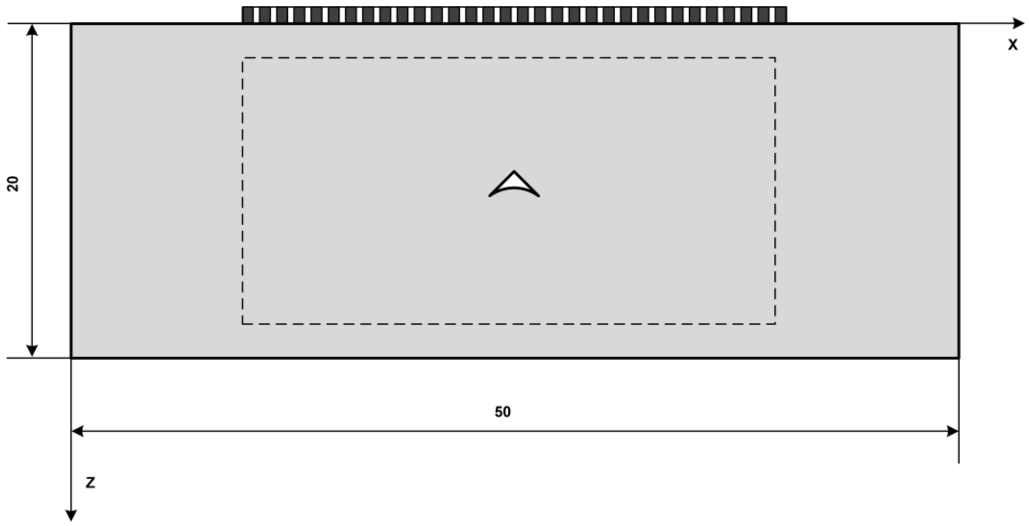

(c)

Figure 3.4 *Cont.*

3.3.2 Results

Applying the ERTM method (Equation 3.1), the upper surface and the lower surface of the damage are displayed in **Figures 3.5(a)** and **Figure 3.5(b)**, respectively. Aggregating the above two images produces a resulting image, **Figure 3.5(c)**, in which the full profile of the embedded flaw is characterized, coinciding exactly with the actual flaw geometry. For illustrative comparison, the conventional methods, RTM and TFM, are also employed, and the resulting images are shown in **Figure 3.5(d)** and **Figure 3.5(e)**, respectively. In both images, the upper surface of the flaw is defined only, while the lower flaw surface fails to be portrayed.

With the same imaging procedure, the flaw in C-II and C-III are reconstructed in **Figures 3.6** and **3.7**, respectively. The imaging results confirm the conclusion that the EMTR method can efficiently characterize the lower surface of the flaw, conducive to the precise delineation of the flaw with full features; whereas conventional methods highlight flaw upper surface only, which is poor to accurately define the lower flaw surface.

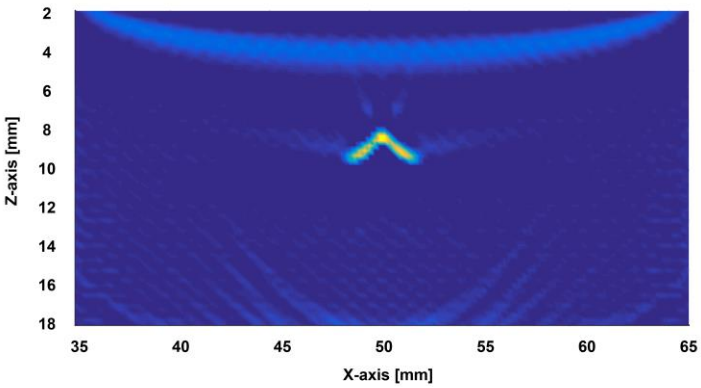

(a)

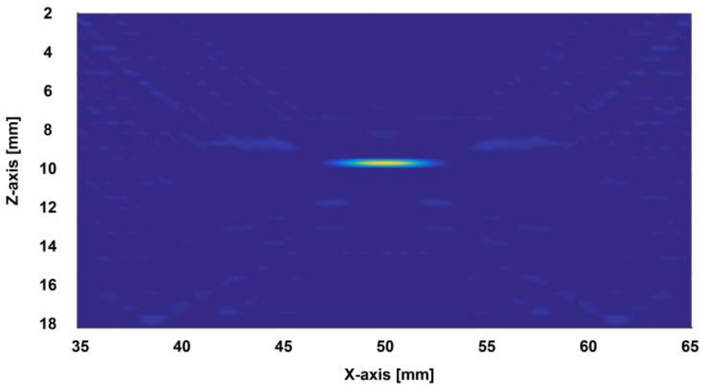

(b)

Figure 3.5 (a) Reconstructed image of the flaw upper surface using ERTM for C-I; (b) reconstructed image of the flaw lower surface using ERTM for C-I ; (c) reconstructed image of the flaw using ERTM for C-I; (d) reconstructed image of the flaw using RTM for C-I; and (e) reconstructed image of the flaw using TFM for C-I; Z axis represents the distance below the array surface which is positioned at Z = 0; X axis represents the distance in region of interest (RoI) (the dotted-line-framed region in **Figure 3.4**(a)).

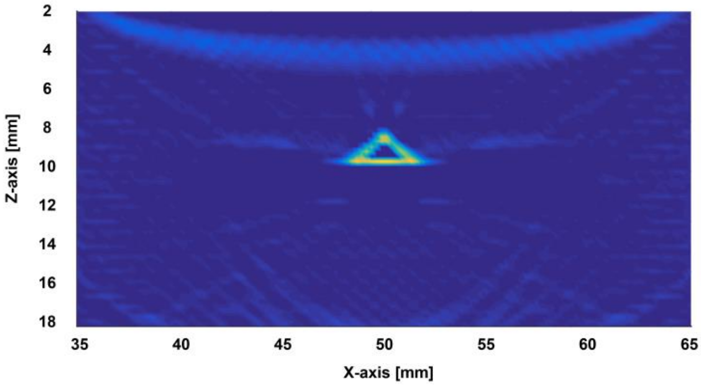

(c)

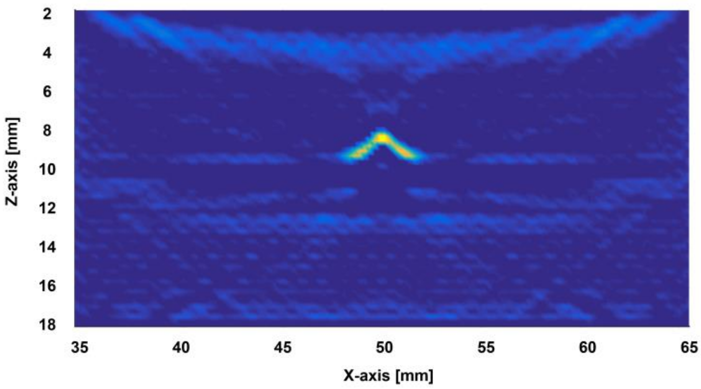

(d)

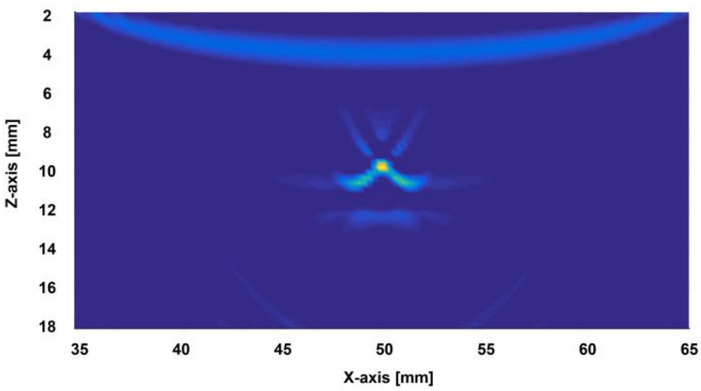

(e)

Figure 3.5 *Cont.*

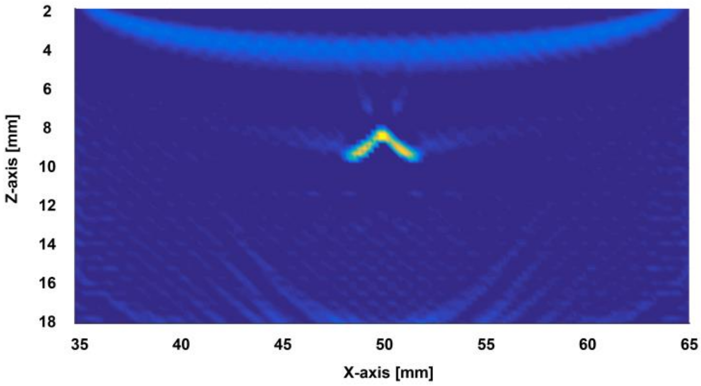

(a)

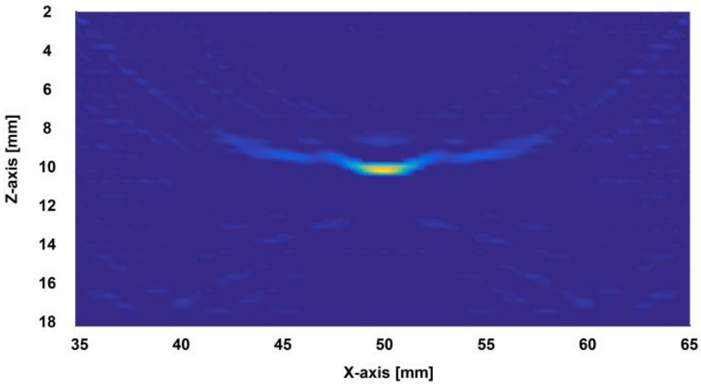

(b)

Figure 3.6 (a) Reconstructed image of the flaw upper surface using ERTM for C-II; (b) reconstructed image of the flaw lower surface using ERTM for C-II; (c) reconstructed image of the flaw using ERTM for C-II; (d) reconstructed image of the flaw using RTM for C-II; and (e) reconstructed image of the flaw using TFM for C-II; Z axis represents the distance below the array surface which is positioned at Z = 0; X axis represents the distance in RoI only (the dotted-line-framed region in **Figure 3.4**(b)).

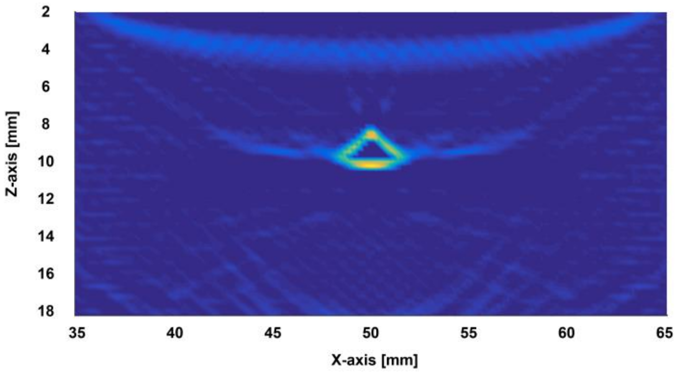

(c)

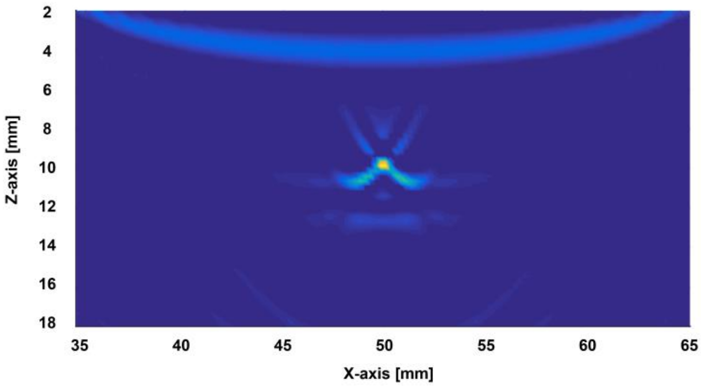

(d)

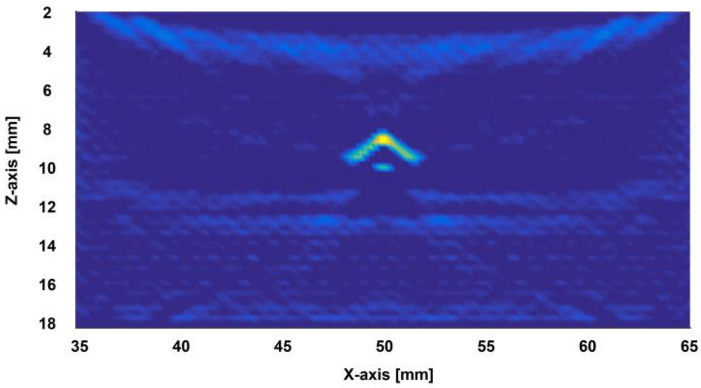

(e)

Figure 3.6 *Cont.*

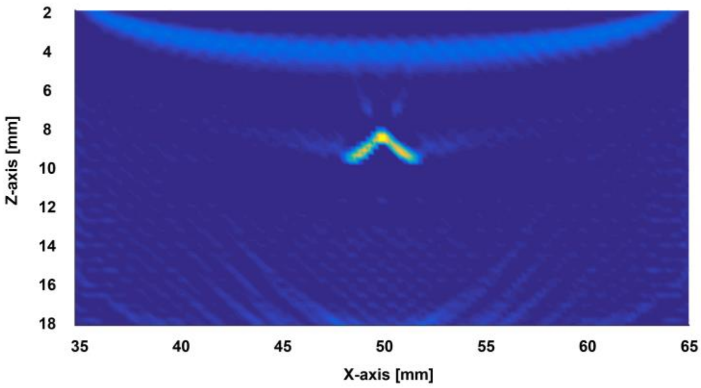

(a)

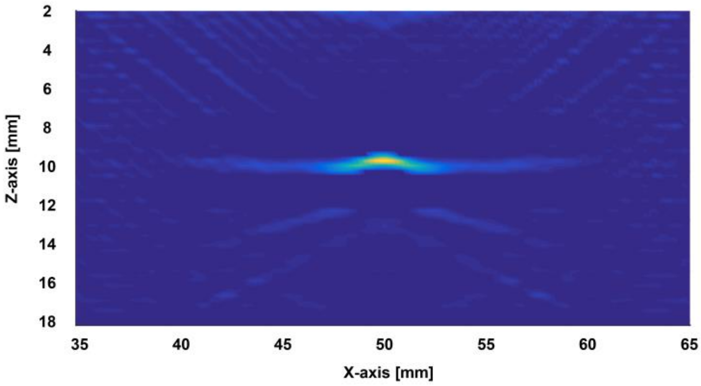

(b)

Figure 3.7 (a) Reconstructed image of the flaw upper surface using ERTM for C-III; (b) reconstructed image of the flaw lower surface using ERTM for C-III ; (c) reconstructed image of the flaw using ERTM for C-III; (d) reconstructed image of the flaw using RTM for C-III, and (e) reconstructed image of the flaw using TFM for C-III; Z axis represents the distance below the array surface which is positioned at Z = 0; X axis represents the distance in RoI only (the dotted-line-framed region in **Figure 3.4**(c)).

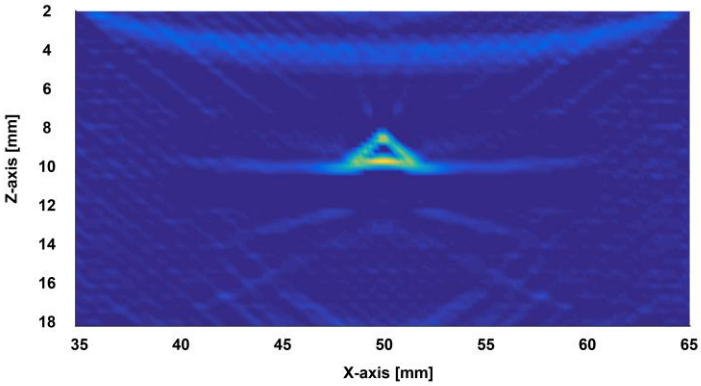

(c)

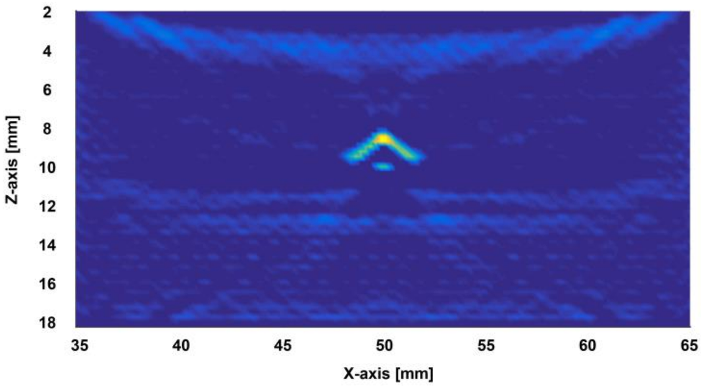

(d)

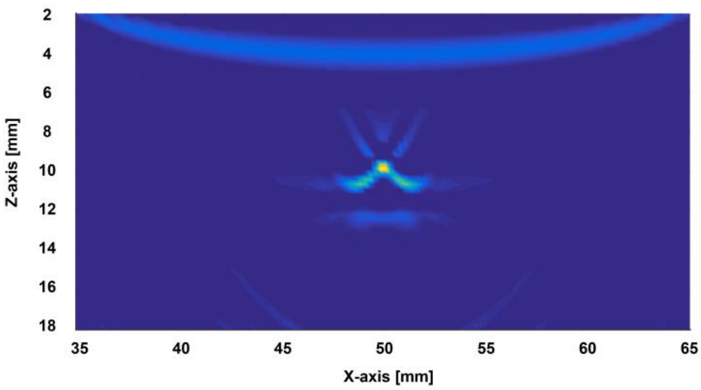

(e)

Figure 3.7 *Cont.*

3.4 Experimental Validation

To experimentally validate the proposed ERTM imaging framework, an ultrasound testing platform (SonixTOUCH, Ultrasonix™) is designed and built, as shown in **Figure 3.8(a)**. A linear array with 128 elements is arranged on the top surface of the specimen (longitudinal wave velocity $c_L = 6190$ m/s, density $\rho = 2700$ kg/m^3, and Poisson's ratio $\upsilon = 0.33$) and is regulated by the array controller (SonixTOUCH, Ultrasonix™) to excite and capture wave signals. The excitation wave – a 3-cycle Gaussian pulse with a central frequency of 5 MHz – is generated under an applied voltage of 60 V. A side-drilled hole (SDH) of 8 mm in diameter is introduced in the aluminum block as the damage scenario, **Figure 3.8(b)**.

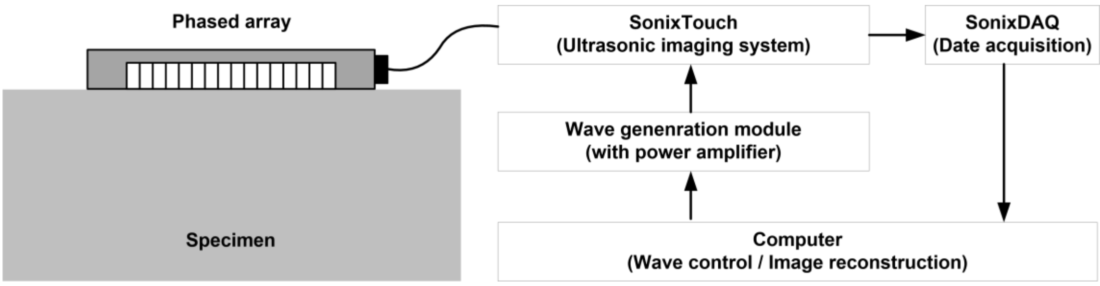

(a)

Figure 3.8 (a) Schematic of experimental set-up for validation; (b) An aluminum block featuring an SDH of 8 mm in diameter (all dimensions in mm).

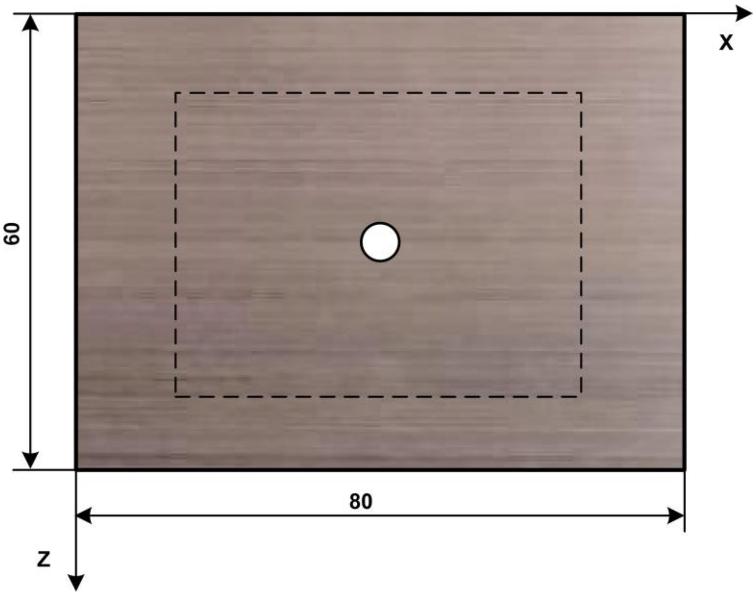

(b)

Figure 3.8 *Cont.*

The reconstructed image using the ERTM algorithm is presented in **Figure 3.9(a)**, in which both the upper surface and lower surface of damage are clearly and accurately indicated in the image, achieving superior imaging of full features of the embedded damage. To take a step further, conventional TFM and RTM algorithms are recalled for comparison, and reconstructed images are presented in **Figures 3.9(b)** and **3.9(c)**, respectively. It can be seen that both the methods fail to delineate the lower surface of the embedded damage accurately, let alone achieve a detailed depiction of its full features.

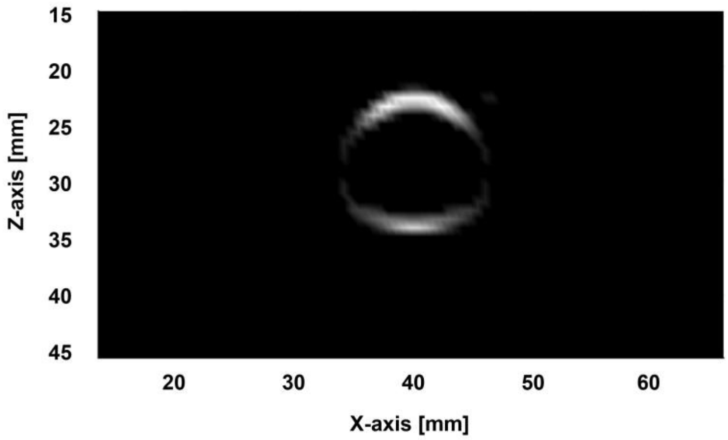

(a)

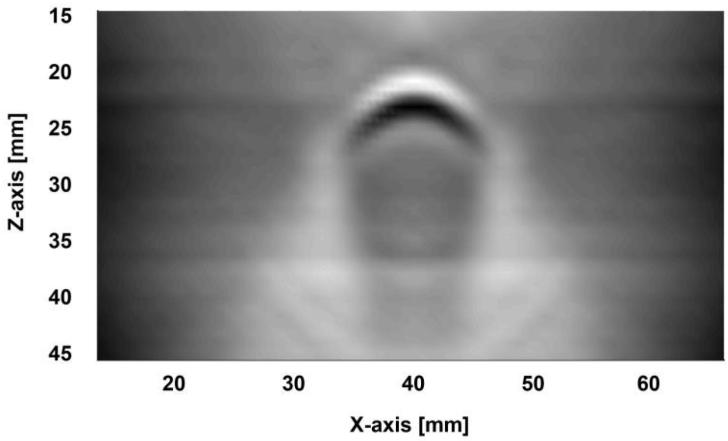

(b)

Figure 3.9 Reconstructed images using (a) ERTM; (b) RTM; and (c) TFM; *Z* axis represents the distance below the array surface which is positioned at $Z = 0$; *X* axis represents the distance in RoI only (the dotted-line-framed region in **Figure 3.8**(b)).

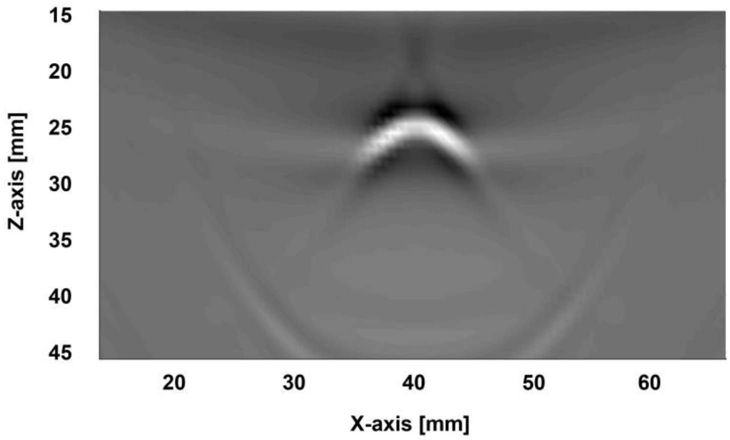

(c)

Figure 3.9 *Cont.*

3.5 Summary

In this chapter, the ETRM imaging algorithm is investigated for depicting damage characterization and geometric profiling. The new algorithm, on the basis of the multipath scattering analysis and Fermat's principle of the acoustic wave propagation, proposes a virtual phased array to characterize the lower surface of the embedded damage. In conjunction with the damage upper surface constructed by the actual phased array, the full features damage can be precisely delineated. The ERTM is validated, in both simulation and experiment, by evaluating flaw with different geometric profiles. Results show that compared with the conventional methods, the developed EMTR method can efficiently define the lower surfaces of the flaw and therefore precisely delineate full features of the flaw, which provides a great alternative for characterizing the flaw with complex shapes.

CHAPTER 4

A Reverse Time Migration-based Multistep Angular Spectrum Approach for Ultrasonic Imaging of Specimens with Irregular Surfaces

4.1 Introduction

The prevailing imaging algorithms have proven the capacity of inspecting a specimen with a flat surface that is either in parallel or oblique to the surface of the phased array. Nevertheless, these algorithms often fail when they are extended to the specimens with non-planar surfaces, irrespective of the fact that the non-planar surfaces are ubiquitous in engineering practice such as weld-caps, molded components and pipelines. To circumvent such deficiency that most ultrasonic imaging algorithms may encounter, this chapter details a new ultrasonic imaging framework for a specimen featuring an irregular top surface, and demonstrate its capability of accurately depicting the multiple damage sites hidden in the specimen. Central to the framework is a multistep ASA, via which the forward propagation wavefields of wave sources and backward propagation wavefields of the received wave signals are calculated. Upon applying a zero-lag cross-correlation imaging condition of RTM to the obtained forward and backward wavefields, the image of the specimen with an irregular surface can be reconstructed, in which hidden damages, if any and regardless of quantity, are visualized.

4.2 RTM-based Multistep ASA

4.2.1 Reverse Time Migration (RTM)

In RTM-based imaging, the imaging conditions are applied to the forward propagation of a source signal and the backward propagation of a received signal, to reconstruct an image along with the specimen depth. Both the forward and backward wave propagation in a homogeneous medium is calculated on the basis of the acoustic wave equation using acoustic parameters (density, acoustic velocity, *etc.*) known a priori, with the assumption that the specimen is free of damage. **Figure 4.1** shows the schematic of wave propagation in a homogeneous solid immersed in the fluid with an irregular top surface (*i.e.*, a fluid-solid coupled system with an irregular interface) and hidden damage, when an N-element linear phased array is placed in the fluid to perform ultrasonic scanning.

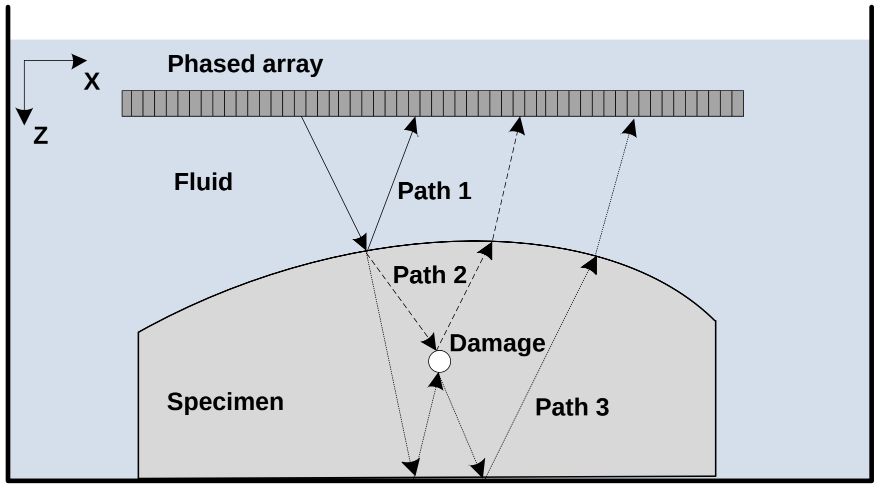

Figure 4.1 Schematic of wave propagation in a fluid-solid coupled system with an irregular interface and hidden damage, under ultrasonic inspection using a phased array.

For the 2D scenario shown in **Figure 4.1**, with (x, z) representing the Cartesian coordinates of an image pixel and t denoting the time, consider three paths of wave propagation when the n^{th} element in the phased array ($n = 1, 2, ..., N$) is triggered to emit a probing wave into the coupled system: *Path* 1 – the wave is reflected directly from the upper surface of the specimen, and then captured by an element in the array; *Path* 2 – the wave is incident to the specimen, reflected by the damage, and then captured by an element in the array; and *Path* 3 – the wave is incident to the specimen, reflected by the specimen bottom to interact with the lower damage surface, reflected by the bottom again after wave scattering from the lower damage surface, and then captured by an element in the array. Amongst these three wave propagation paths, the wave signal along *Path* 1 contributes to the spatial determination of the specimen top surface, while the signals along *Paths* 2 and 3 facilitate imaging of the hidden damage. The wave signal acquisition duration, T, shall be sufficiently long, so that the multiple reflections from the specimen bottom along *Path 3* can be included in the captured signals.

RTM-based imaging embraces the following three key steps in sequence:

(i) the wave signal excited by the n^{th} element in the phased array is propagated forward in time with material properties and medium geometrical information known *a priori*, to extrapolate the source wavefields $S_n(x,z,t)$, ($n=1,2,...,N$) from the initial time (when $t=0$) through the end of the signal acquisition (when $t=T$);

(ii) the received signals are reversed in time – the kernel of the RTM-based imaging; subsequently, the time-reversed signals are excited at the corresponding locations of all elements in the array, to extrapolate the receiver wavefields $R_n(x,z,T-t)$; and

(iii) the image of the specimen is reconstructed after the zero-lag cross-correlating the source wavefields and the receiver wavefields under certain imaging conditions.

In this study, the zero-lag cross-correlation imaging condition in (iii), for all the possible pairs of source elements and receiving elements in the array, is defined as

$$I(x,z)=\sum_{n=1}^{N}\frac{\sum_{t=0}^{T}S_n(x,z,t)\cdot R_n(x,z,T-t)}{\sum_{t=0}^{T}S_n^2(x,z,t)} \qquad (n=1,2,...,N), \quad (4.1)$$

where $I(x,z)$ is the image value at a pixel (x,z) in the reconstructed image. To obtain the forward propagation wavefield $S_n(x,z,t)$ and backward propagation wavefield $R_n(x,z,T-t)$ in the specimen, one can use the aforementioned numerical methods, with which the entire fluid-solid coupled system, including the fluid, has to be modeled and imaged. This demands the extraordinarily high yet unnecessary computational cost, even though the wavefield in the fluid contributes none to the characterization of damage – a major demerit that conventional RTM-based imaging has.

4.2.2 Multistep Angular Spectrum Approach (ASA)

A multistep ASA-based imaging framework is developed, to break through the limitations of conventional RTM in tackling fluid-solid coupled media with irregular interfaces. This framework allows modeling and calculation of the wavefields in the local region of interest (RoI) only, rather than the entire coupled system. Furthermore, it circumvents the shortcoming of the conventional ASA (namely, the extrapolation of wavefield can only be fulfilled when the interface possesses uniform acoustic parameters in the horizontal direction, and it cannot be extended to a solid with an irregular surface) [158-160].

With the assumption that (i) wave reflections from the top surface of the fluid and from the phased array surface are not taken into account, and (ii) the mode conversion in wave propagation is neglected, due to the weakness in the energy of the converted transverse wave mode, and only the longitudinal wave is investigated. The model for extrapolating wavefields is illustrated schematically in **Figure 4.2**. A twofold calculation process is proposed for wavefield extrapolation: (i) wave propagation in the fluid is ascertained to obtain the wavefields at the fluid-solid interface, as detailed in Section 4.2.2.1; (ii) the obtained wavefields at the interface are then treated as incident waves to emit into the solid, and with that, the wavefields in the solid are extrapolated, Section 4.2.2.2.

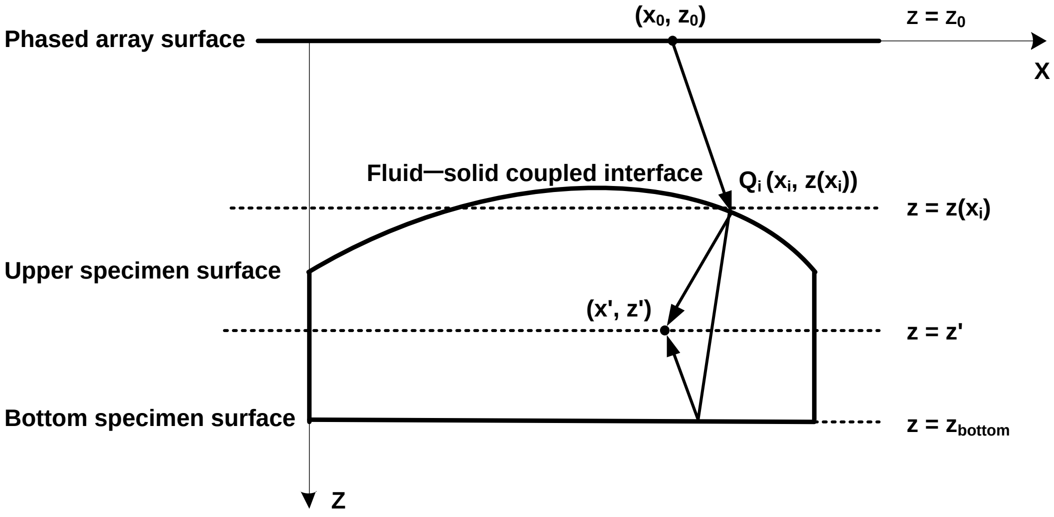

Figure 4.2 A 2D model for wavefield extrapolation in a fluid-solid coupled system with an irregular interface.

4.2.2.1 *Wavefields in Fluid and at Interface*

For the fluid-solid coupled system with an irregular interface shown in **Figure 4.2**, a phased array is placed in the fluid at the plane when $z = z_0$ for wave excitation and acquisition. Given that an input signal $p(t)$ is produced by a source element in the phased array at (x_0, z_0), the Fourier modality of the acoustic pressure distribution, $P(x, z, f)$, at the initial plane when $z = z_0$ can be expressed as

$$P(x, z_0, f) = P(f) \cdot \delta(x - x_0), \tag{4.2}$$

where δ signifies the Dirac function and f the frequency. $P(f)$ is the Fourier transform of $p(t)$. Subsequently, Fourier transform is applied to $P(x, z_0, f)$ with respect to *x*, to transform $P(x, z_0, f)$ from the spatial to the wavenumber domain, and obtain its angular spectrum, $\hat{P}(k_x, z, f)$, at the plane when $z = z_0$, which reads

$$\hat{P}(k_x, z_0, f) = P(f) e^{-ik_x x_0}, \tag{4.3}$$

where k_x denotes sampling wavenumber along x direction in the spatial frequency domain, which is the same in the solid and the fluid.

Without loss of the generality, arbitrarily choose a point at the irregular interface, Q_i (here, subscript i denotes a parameter at the interface; $i = 1, 2, \ldots, M$ where M stands for the total number of the discrete points selected on the interface for ASA calculation). The coordinates of Q_i, namely $\left(x_i, z\left(x_i\right)\right)$, can be determined in terms of the ToF of the first echo wave (*i.e.*, the wave propagating along *Path 1* as shown in **Figure 4.1**). When the probing wave travels from the initial plane ($z = z_0$) to point Q_i, the angular spectrum of the acoustic field at the plane $z = z(x_i)$, denoted with $\hat{P}\left(k_x, z(x_i), f\right)$, can be derived by introducing a phase shift with regard to $\hat{P}\left(k_x, z_0, f\right)$, as

$$\hat{P}\left(k_x, z(x_i), f\right) = \hat{P}\left(k_x, z_0, f\right) e^{-ik_{fluid-z}\left(z(x_i) - z_0\right)}, \tag{4.4}$$

where $k_{fluid-z} = \sqrt{k_{fluid}^2 - k_x^2}$ ($k_{fluid} = 2\pi f / c_{fluid}$: the wavenumber in the fluid; c_{fluid} : the velocity of a wave in the fluid).

Subsequently, the transient wavefield at Q_i, *viz*., $p\left(x_i, z\left(x_i\right), t\right)$, can be calculated upon applying the 2D inverse Fourier transform (including a spatial inverse Fourier transform first, and then a temporal inverse Fourier transform) on $\hat{P}\left(k_x, z(x_i), f\right)$, via

$$p\left(x_i, z\left(x_i\right), t\right) = \mathcal{F}_{2D}^{-1}\left\{\hat{P}\left(k_x, z(x_i), f\right)\Big|_{x=x_i}\right\}, \tag{4.5}$$

where $\mathcal{F}_{2D}^{-1}$ represents the 2D inverse Fourier transform.

4.2.2.2 *Wavefields in Solid*

The transient wavefield at the interface derived in the above, $p\left(x_i, z\left(x_i\right), t\right)$, is incident to the solid. Provided a damage site exists in the solid at $\left(x', z'\right)$, in **Figure 4.2**, the damage scatters the incident wave via direct reflection from the plane $z = z'$ (*Path 2*) and multiple reflections from the specimen bottom (*Path 3*). In the same vein, the angular spectrum of the acoustic field at the plane $z = z'$, where the damage exists, $\hat{P}_i^{(solid)}\left(k_x, z', f\right)$, can be ascertained, using Equation (4.4), as,

$$\hat{P}_i^{(solid)}\left(k_x, z', f\right) = \hat{P}\left(k_x, z(x_i), f\right) e^{-ik_{solid-z}\left(z'-z\left(x_i\right)\right)} + C \cdot \hat{P}\left(k_x, z(x_i), f\right) e^{-ik_{solid-z}\left(2z_{bottom}-z'-z\left(x_i\right)\right)}$$

$$(i = 1, 2, \ldots, M), \qquad (4.6)$$

In Equation (4.6) the first term $\hat{P}\left(k_x, z(x_i), f\right) e^{-ik_{solid-z}\left(z'-z\left(x_i\right)\right)}$ and the second term $C \cdot \hat{P}\left(k_x, z(x_i), f\right) e^{-ik_{solid-z}\left(2z_{bottom}-z'-z\left(x_i\right)\right)}$ refer to the wavefields contributed by *Paths* 2 and 3, respectively; the superscript or subscript '*solid*' distinguishes variables in the solid from those in the fluid as used in Section 4.2.2.1. $k_{solid-z} = \sqrt{k_{solid}^2 - k_x^2}$ (k_{solid}: the wavenumber in the solid). C is a generalized reflection coefficient determined by the traction-free boundary condition at the specimen bottom, which can be obtained by solving Equation (4.6) when the term $\sum_i \left[\hat{P}\left(k_x, z(x_i), f\right) e^{-ik_{solid-z}\left(z'-z\left(x_i\right)\right)} + C \cdot \hat{P}\left(k_x, z(x_i), f\right) e^{-ik_{solid-z}\left(2z_{bottom}-z'-z\left(x_i\right)\right)}\right]$ is zero. It is the introduction of such a coefficient in the angular spectrum calculation that makes it possible to accurately describe the lower surface of the hidden damage, in contrast with conventional imaging using TFM in which only the wave reflections from the upper surface of the damage (*i.e.*, wave propagation along *Path* 2) are considered. Equation (4.6) is manipulated for each discrete point on the interface (M in total) to yield $\hat{P}_i^{(solid)}\left(k_x, z', f\right)$ (where $i = 1, 2, ..., M$), summation of which leads to the total angular spectrum $\hat{P}^{(solid)}\left(k_x, z', f\right)$, at the plane $z = z'$ (where damage exists):

$$\hat{P}^{(solid)}\left(k_x, z', f\right) = \sum_{i=1}^{M} \hat{P}_i^{(solid)}\left(k_x, z', f\right) \qquad (i = 1, 2, ..., M). \tag{4.7}$$

Subsequently, using the 2D inverse Fourier transform, the transient wavefield at the point $\left(x', z'\right)$ can be obtained, as

$$p\left(x', z', t\right) = \mathcal{F}_{2D}^{-1}\left\{\hat{P}^{(solid)}\left(k_x, z', f\right)\Big|_{x=x'}\right\}. \tag{4.8}$$

Upon applying the above multistep ASA to the excited signals and time-reversed signals, the forward and backward propagation wavefields in the solid are defined. With the wavefields, the entire solid can be imaged using Equation (4.1) of the RTM algorithm, in which damages, if any in the solid and regardless of the quantity, can be visualized.

4.2.3 Numerical Verification

To verify the RTM-based multistep ASA for ultrasonic imaging, numerical simulation is performed first, in which a 2D fluid-solid coupled system, as schematically shown in **Figure 4.3(a)**, is considered. The depth of the fluid and the solid is 10 mm each, with respective key acoustic parameters listed in **Table 4.1**, and key parameters used in ASA calculation in **Table 4.2**.

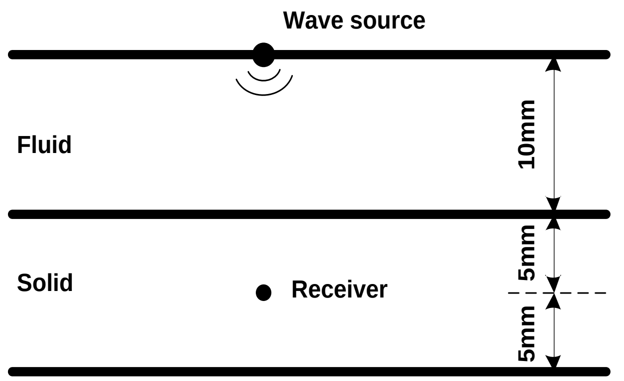

(a)

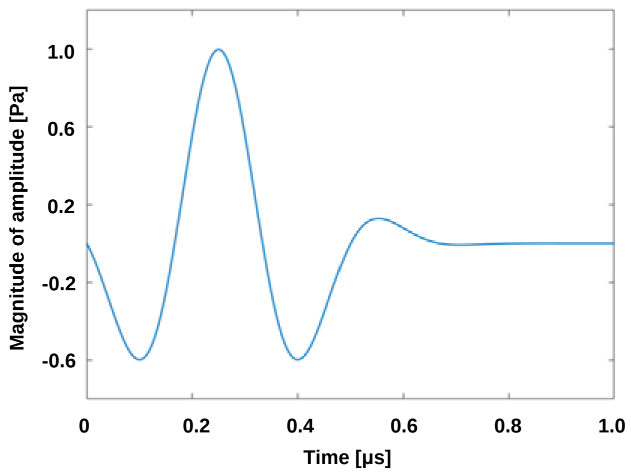

(b)

Figure 4.3 (a) A simplified 2D fluid-solid coupled system for illustrating multistep ASA-based imaging; (b) excitation signal; and (c) comparison of results obtained using the proposed algorithm and using FEM.

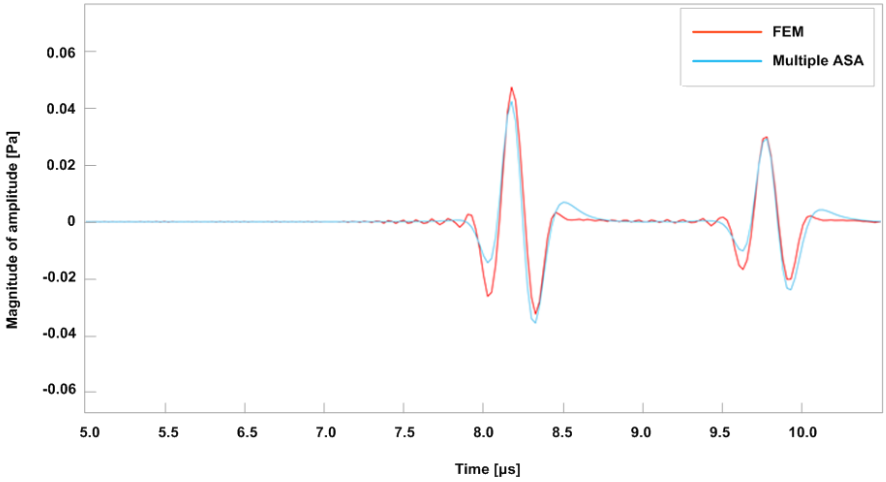

(c)

Figure 4.3 *Cont.*

Table 4.1 Acoustic parameters of the fluid-solid coupled system in simulation

	fluid	solid
Velocity of wave (m/s)	1480	6300
Density (kg/m^3)	1000	2700

Table 4.2 Key parameters used in the simulation for 2D inverse Fourier transform

Sampling frequency	80 MHz
Sampling interval of frequency	0.05 MHz
Sampling wavenumber	45 mm^{-1}
Sampling interval of wavenumber	0.005 mm^{-1}

A point-like wave source is placed at the upper boundary of the fluid to excite an acoustic wave – a 1.5-cycle hamming modulated sinusoidal toneburst centered at

5MHz, **Figure 4.3(b)**. Eight discrete points per wavelength are selected on the interface (Q_i) for multistep ASA calculation.

To verify the results obtained using multiple ASA, FEM-based modeling and simulation are performed using COMSOL Multiphysics® software. The FEM model features the same dimension along the *z* direction with that in the multistep ASA calculation, while it has a finite dimension along the *x* direction and is then applied with acoustic absorbing boundaries at both the left and right boundaries (eliminating wave reflection at boundaries). Thus, the model used in the multistep ASA calculation and the one in the FEM simulation have identical boundary conditions. The mesh size of the FEM model is 0.06 mm in the fluid and 0.24 mm in the solid. Arbitrarily choosing a point in the solid as the receiving point, as indicated in **Figure 4.3(a)**, the time-series signal of the FEM-calculated wavefield at the receiving point is compared with that obtained using the multistep ASA, in **Figure 4.3(c)**, to observe quantitative matching in between.

It is noteworthy that under the same computational conditions, the computing time consumed by the multistep ASA calculation is reduced drastically to 500 seconds from the 3390 seconds used by the FEM simulation.

4.3 Experimental Validation

The multistep ASA-based imaging framework is validated experimentally on an ultrasound testing platform (SonixTOUCH, *Ultrasonix*™). Two aluminum blocks with irregular top surfaces – one featuring a parabolic surface and the other a wavelike surface, are immersed in water for ultrasonic scanning.

4.3.1 Set-up and Specimens

The experimental set-up is illustrated schematically in **Figure 4.4**, showing the key equipment adopted. The first specimen, **Figure 4.5(a)**, has a parabolic surface, in which four side-drilled holes (SDHs) are pre-treated, the diameter of these holes is 2.5 mm, which is prudently selected to examine the detectability of the proposed algorithm; while the second specimen, **Figure 4.6(a)**, possesses a top surface of a sinusoidal profile, in which two SDHs (Ø2.5 mm each) are pre-introduced. The locations of array surface, specimen surfaces, and SDHs are indicated in **Figures 4.5(a)** and **4.6(a)**, for two specimens.

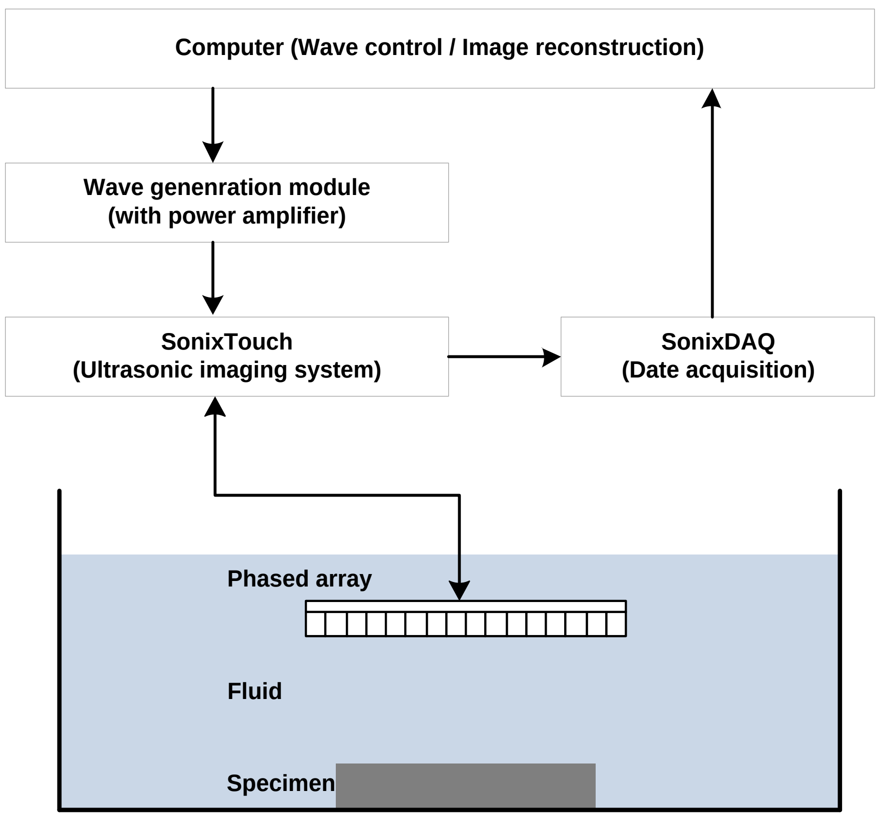

Figure 4.4 Schematic of experimental set-up for validation.

The respective acoustic parameters of the fluid and the two specimens remain the same as those in numerical verification, **Table 4.1**. A multi-channel data acquisition module (SonixDAQ, *Ultrasonix*^{TM}) is used to capture signals which render up to 128 channels at a sampling rate of 80 MHz for each channel. A commercial array controller (SonixTOUCH, *Ultrasonix*^{TM}) regulates a linear array with a central resonance frequency of 5 MHz which comprises 128 elements (0.2698 mm in width for each element and 0.3048 mm in pitch). A 3-cycle Gaussian pulse is excited with the array under an applied voltage of 60 V, to generate the probing ultrasonic waves. Reflected wave signals from the specimen surface, damage, and specimen bottom are acquired with the array via fluid coupling.

4.3.2 Results

The surface of each specimen is first determined via a B-scan in which the wave propagation along *Path* 1 is considered and the Hilbert envelope of the corresponding waveform data is used to image interface depth, with results shown in **Figures 4.5(b)** and **4.6(b)**. The identified specimen surfaces tally well with the reality. With the determination of the location of the specimen surface, the transient wavefields at the specimen surface are calculated using the multistep ASA (Equation (4.5)). Subsequently, these wavefields are used as the incident waves to the specimen, and the wavefields at any location throughout the entire specimen can be calculated using Equations (4.6), (4.7), and (4.8). Applied with the zero-lag cross-correlation imaging conditions as defined in Equation (4.1), the image of the RoI (the region near the SDHs, namely the dotted-line-framed region in figures) can be reconstructed, shown in **Figures 4.5(c)** and **4.6(c)**.

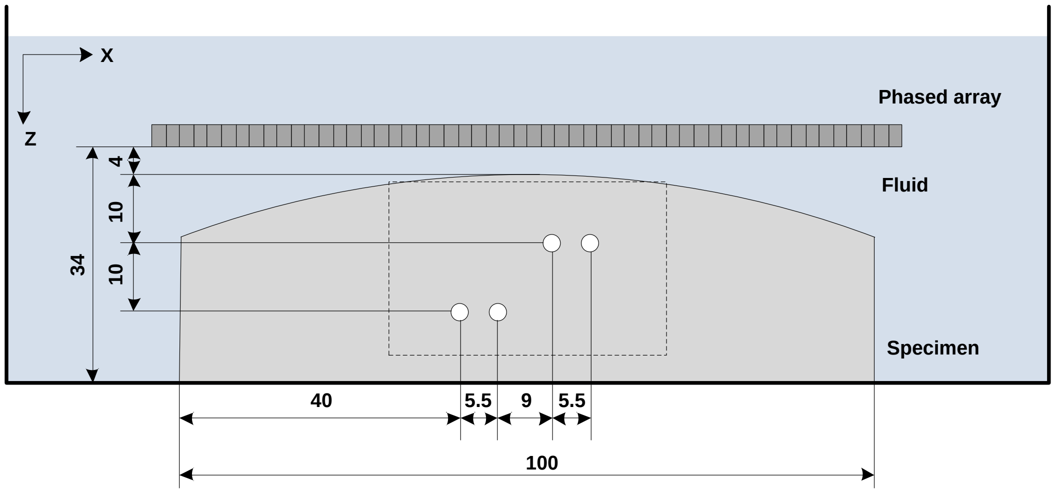

(a)

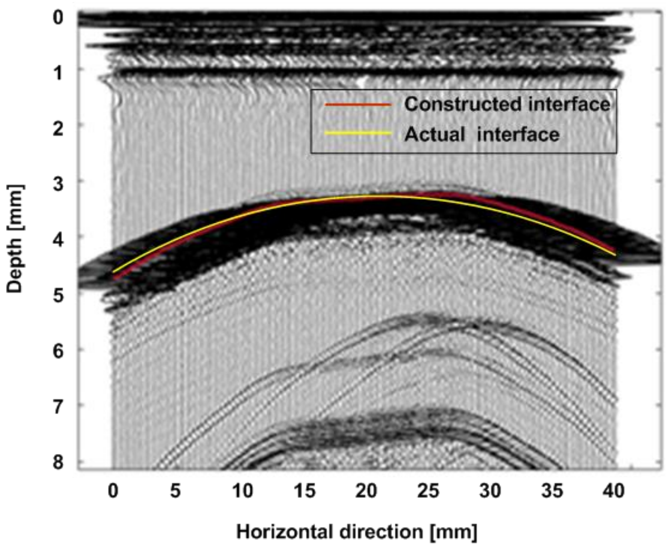

(b)

Figure 4.5 (a) An aluminum block featuring a parabolic surface with four SHDs (unit: mm); (b) image of the upper part of the specimen constructed by a B-scan, for determination of specimen upper surface; (c) reconstructed image using the proposed imaging algorithm; and (d) reconstructed image using conventional TFM (for (c) and (d), Z axis represents the distance below the array surface which is positioned at Z=0; X axis represents the distance in RoI only (the dotted-line-framed region in **Figure 4.5**(a)).

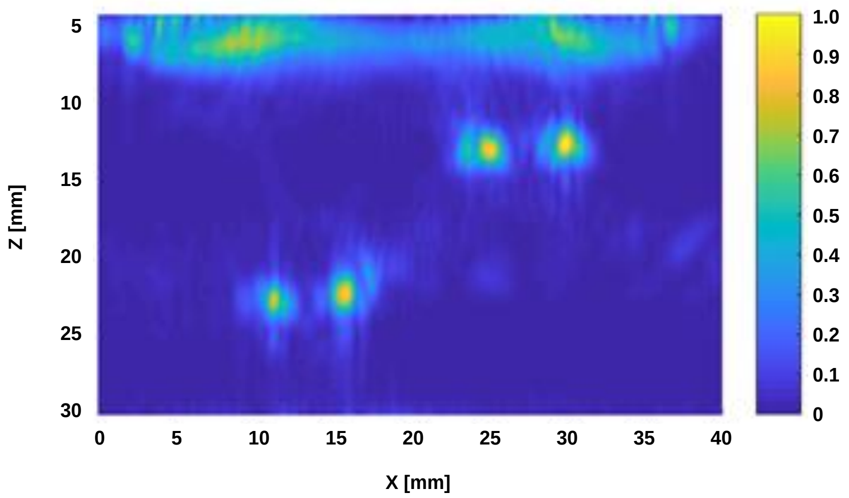

(c)

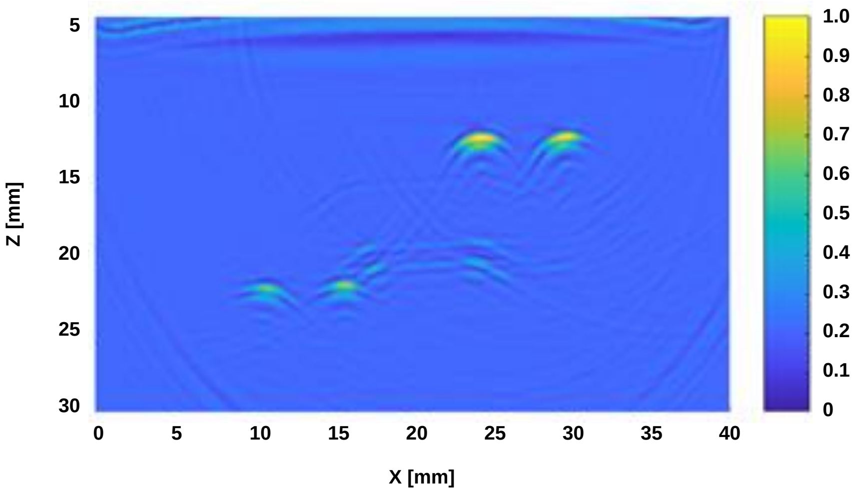

(d)

Figure 4.5 *Cont.*

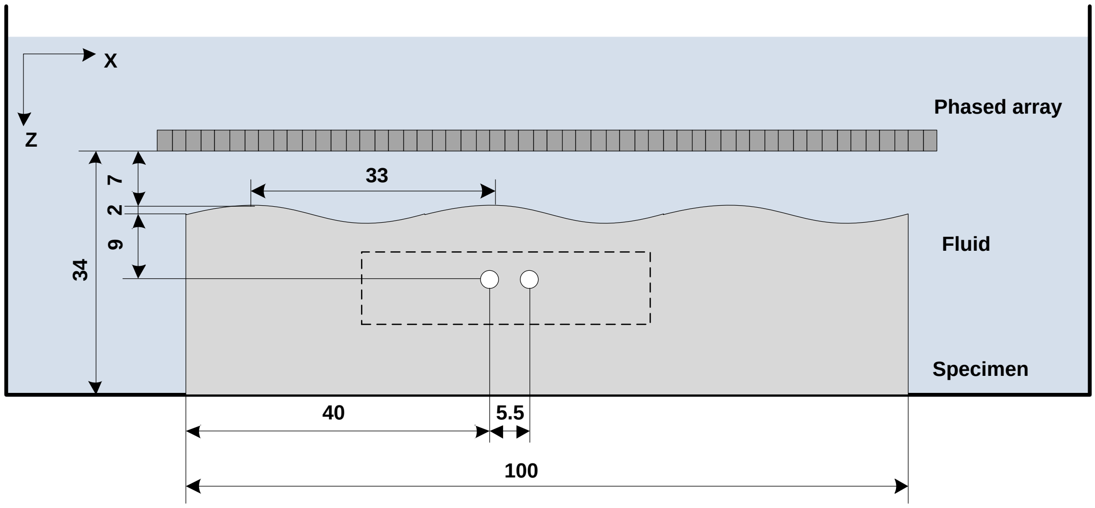

(a)

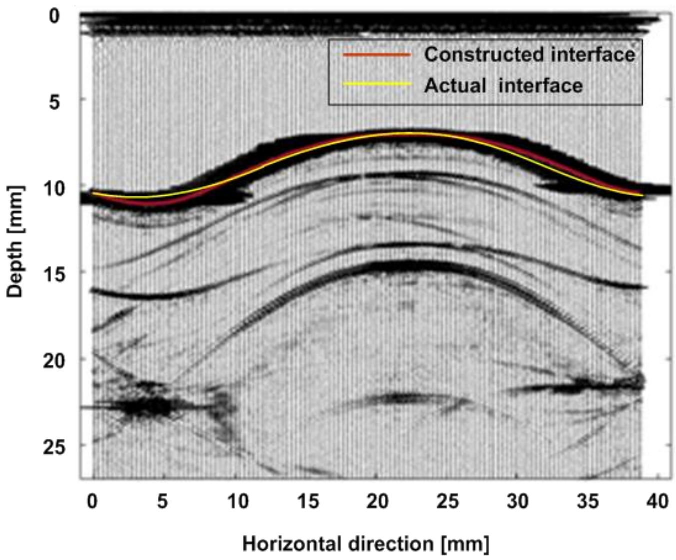

(b)

Figure 4.6 (a) An aluminum block featuring a sinusoidal surface with two SHDs (unit: mm); (b) image of the upper part of the specimen constructed by a B-scan, for determination of specimen upper surface; (c) reconstructed image using the proposed imaging algorithm; and (d) reconstructed image using conventional TFM (for (c) and (d), Z axis represents the distance below the array surface which is positioned at Z=0; X axis represents the distance in RoI only (the dotted-line-framed region in **Figure 4.6**(a)).

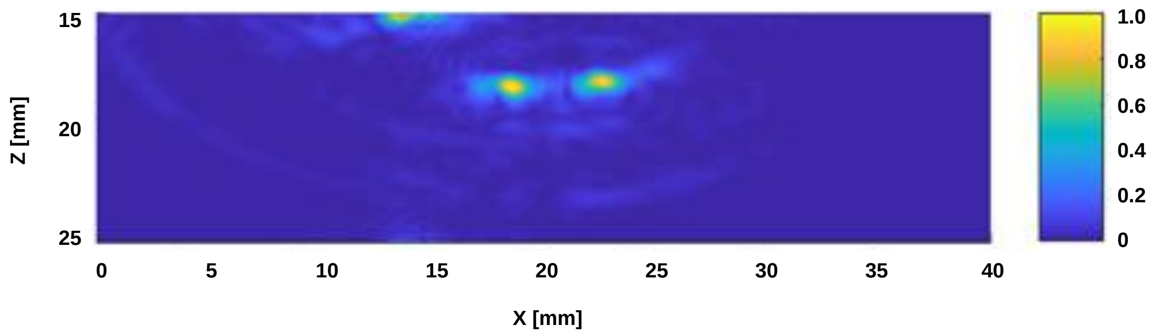

(c)

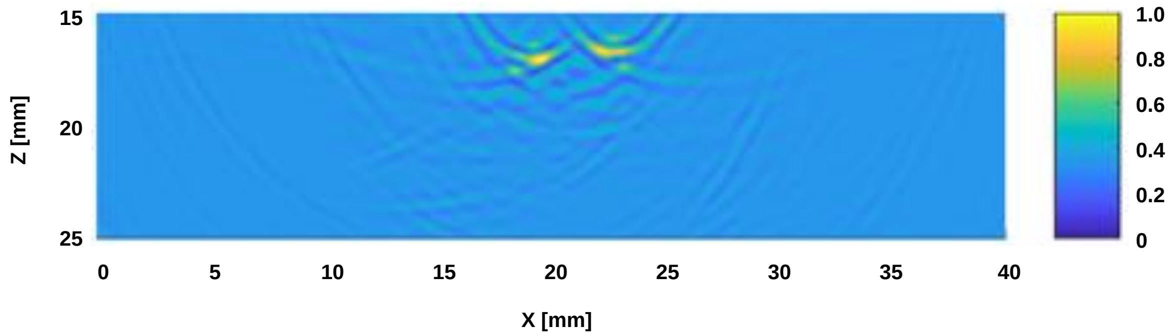

(d)

Figure 4.6 *Cont.*

In the RoI images, each SDH in the two specimens is precisely depicted, showing not only its location and upper surface, but also its lower surface, thanks to the inclusion of multiple wave reflections from the damage and from the specimen bottom during wavefield extrapolation in the proposed approach. Notably, the proposed ASA allows imaging of the RoI only, while avoids modeling and imaging the entire fluid-solid coupled system, which significantly reduces the computational cost and unburdens computing hardware.

Artifacts are observed in the reconstructed images, most of which are near the specimen upper surfaces – an inevitable consequence due to the inclusion of wave reflections from the specimen upper surface during wavefield extrapolation. Upon obtainment of the wavefields at the interface, the reflection remains in the incident wave to the specimen, and then in the backward propagation, resulting in artifacts near the specimen upper surfaces.

4.4 Discussion: Comparison with Conventional Total Focusing Method (TFM)

To compare with the proposed RTM-based multistep ASA, conventional TFM is recalled, to characterize the same SDHs in the two specimens, in which all testing parameters remain unchanged. In conventional TFM-based imaging, wave reflections from the specimen bottom are not considered. With the determined locations of the specimen upper surfaces, ToFs of waves are extracted from captured signals, with which images of the specimens are reconstructed, in **Figures 4.5(d)** and **4.6(d)**. In the reconstructed images, all SDHs are located, whereas the image resolution is fairly low with the inadequate description of SDHs, and in particular the lower surface of each SDH is not depicted. In comparison with the conventional TFM, the RTM-based multistep ASA has proven capability of defining the lower damage surface with obviously improved image resolution. In conventional TFM, the irregular specimen surface is also a barrier to preclude the time-reversed signals from focusing at the damage location, resulting in low imaging resolution. Artifacts are also observed in TFM-reconstructed images, which can be attributed to the multiple wave reflections between the specimen bottom and the damage.

Figure 4.7 further compares the mean values of the image pixel within the depth of ± 0.5 mm where SDHs exist, obtained using the proposed multistep ASA approach and using the conventional TFM-based algorithm. To facilitate comparison, imaging contrast is defined, which calibrates the difference between the peak value of the reconstructed SDH and that of the background. It is clear that the background value is reduced remarkably using the proposed ASA-based algorithm. The imaging contrast value obtained using the ASA-based algorithm is observed as high as 1.5 times the value yielded using TFM for the first specimen, **Figure 4.7(a),** and 2 times the value for the second specimen, **Figure 4.7(b)**.

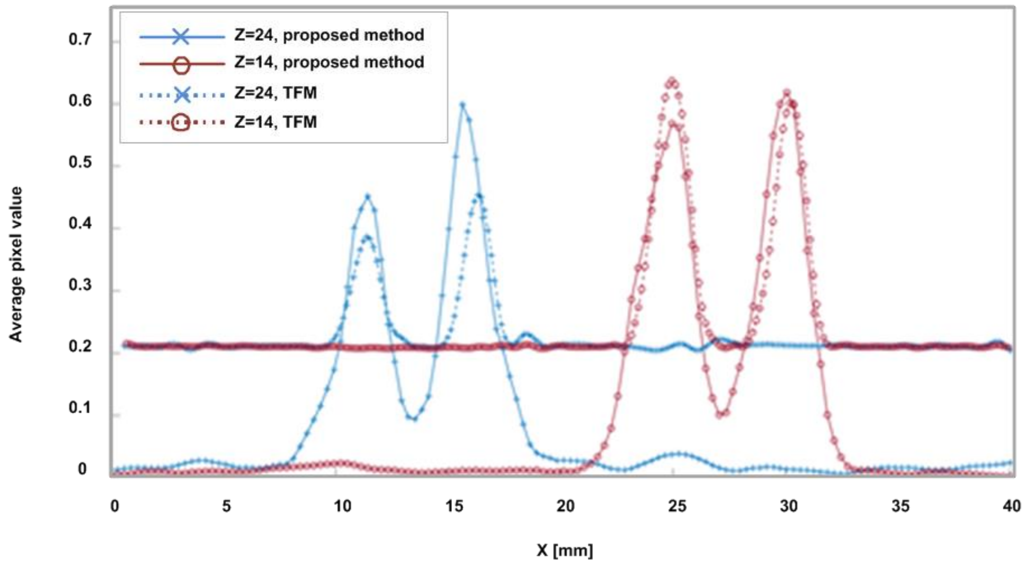

(a)

Figure 4.7 Average values of image pixel within the range of ± 0.5 mm near SDHs: (a) when z = 14 and 24 mm for the specimen with a parabolic curve; and when (b) z = 18 mm for the specimen with a sinusoidal surface.

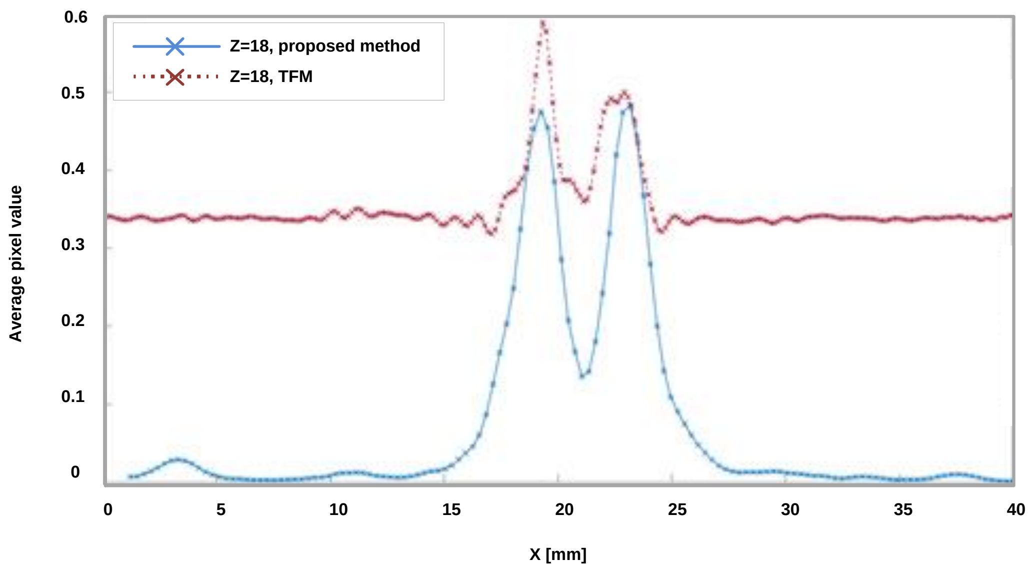

(b)

Figure 4.7 *Cont.*

Although the image resolution of TFM-based or RTM-based imaging does not, in theory, tend to downgrade as depth increases, the quality of reconstructed images may deteriorate due to ultrasonic wave attenuation. **Figure 4.7** argues that the multistep ASA evidently suffers less than TFM from such influence due to wave attenuation, and remains higher image quality for damage at a deeper depth. Such a merit is attributable to the fact that the reflections from the specimen bottom are considered in the wavefield extrapolation.

4.5 Summary

An RTM-based multistep ASA imaging framework is developed for non-destructive testing of a specimen featuring an irregular top surface via water immersion. Multistep ASA calculates forward propagation wavefields of sources and backward propagation wavefields of the received wave signals in the fluid-solid coupled system, with which the transient wavefields at the fluid-solid interface are used as incident waves to the solid. Thanks to the RTM-enhanced algorithm in which multiple wave reflections from the specimen bottom are taken into calculation, the proposed approach demonstrates its capacity of accurately depicting the lower surfaces of multiple damages hidden in the specimen. Experiments are performed to validate the proposed approach, in which multiple SDHs, at different locations in aluminum blocks with various irregular surfaces, are characterized quantitatively. The validation affirms that the multistep ASA shows higher computational efficiency, compared to conventional RTM, and an enhanced imaging contrast against prevailing TFM.

CHAPTER 5

Ameliorated-Multiple Signal Classification (Am-MUSIC) for Damage Imaging Using a Sparse Sensor Network

5.1 Introduction

Multiple signal classification (MUSIC) algorithm is a proven array processing technique for guided wave-based damage characterization. Nevertheless, prevailing MUSIC algorithms are largely bound up with the use of a dense linear array, which fails to access the full planar area of an inspected sample, leaving blind zones to which an array fails to scan. To break the above limitations, the conventional MUSIC algorithm is ameliorated in this study, by manipulating the signal representation matrix at each pixel using the excitation signal series, instead of the scattered signal series, which enables the use of a sparse sensor network with arbitrarily positioned transducers. In the ameliorated MUSIC (Am-MUSIC), the orthogonal attribute between the signal subspace and noise subspace inherent in the signal representation matrix is quantified, in terms of which the Am-MUSIC yields a full spatial spectrum of the inspected sample, and damage, if any, can be visualized in the spectrum.

5.2 Lamb Wave Scattering Theory

Ultrasonic waves guided by a plate-like waveguide, a.k.a. *Lamb waves*, are of a multimodal and dispersive nature. At a given frequency, Lamb waves feature a multitude of wave modes which can be classified as the symmetric and antisymmetric modes. We consider a pure, monochromatic Lamb wave mode in the waveform of a toneburst, as the excitation signal $s(t)$. $s(t)$ is defined in a complex domain as

$$s(t) = u(t)\exp^{i\omega_0 t}, \tag{5.1}$$

where $u(t)$ denotes a window function to regulate the toneburst, t the time, i the imaginary unit, and ω_0 the central frequency of the toneburst. With the attenuation in magnitude as wave propagation in consideration, the Lamb wave, $R(\omega)$, after travelling the distance d can be represented, in the frequency domain, as

$$R(\omega) = \frac{d_0}{\sqrt{d}} S(\omega)\exp^{-ikd}. \tag{5.2}$$

In the above, d_0 signifies an initial distance with regard to which the wave attenuation is calibrated; $S(\omega)$ is the corresponding Fourier representation of $s(t)$; $k = \frac{\omega}{c}$, where k denotes the wavenumber and c represents the propagation velocity of the considered monochromatic Lamb wave mode.

Substituting Eqs. (1) into (2), the Lamb wave $r(t)$ when it arrives at the distance d can be yielded, in the time domain, as

$$r(t) = \frac{d_0}{\sqrt{d}} \mathcal{F}^{-1}\left\{ s(\omega)\exp^{-i\frac{\omega}{c}d} \right\} = \frac{d_0}{\sqrt{d}} s(t - \frac{d}{c}) = \frac{d_0}{\sqrt{d}} u(t - \frac{d}{c})\exp^{i\omega_0 (t - \frac{d}{c})}, \tag{5.3}$$

where $r(t)$ is the inverse Fourier transform of $R(\omega)$ and $\mathcal{F}^{-1}$ is the inverse

Fourier transform.

For an intact waveguide, the captured wave signal, denoted with $r^{\text{measured-intact}}(t)$, is the direct arrival wave $r^{\text{direct}}(t)$ with incoherent noise $w^{\text{measured-intact}}(t)$, as

$$r^{\text{measured-intact}}(t) = r^{\text{direct}}(t) + r^{\text{boundary-reflection}}(t) + w^{\text{measured-intact}}(t), \tag{5.4}$$

where $r^{\text{direct}}(t)$ is the arrival wave propagating along the path from the wave source to the wave receiver. Provided damage is present at an unknown location in the waveguide, the damage can be modeled as a secondary wave source to scatter the incoming Lamb waves. Ignoring mode conversion, the measured signal $r^{\text{measured-damage}}(t)$ comprises the direct arrival wave $r^{\text{direct}}(t)$, boundary-reflection wave $r^{\text{boundary-reflection}}(t)$, additional scattered wave from the damage $r^{\text{scattered}}(t)$, and the incoherent noise $w^{\text{measured-damage}}(t)$, as

$$r^{\text{measured-damage}}(t) = r^{\text{direct}}(t) + r^{\text{boundary-reflection}}(t) + r^{\text{scattered}}(t) + w^{\text{measured-damage}}(t), \tag{5.5}$$

where $r^{\text{scattered}}(t)$ is the arrival wave propagating along a scattered path (namely, the path from the wave source to the damage and then to the wave receiver). Suppose that the direct waves are the same at $r^{\text{measured-intact}}(t)$ and $r^{\text{measured-damage}}(t)$, $r^{\text{scattered}}(t)$ which carries information pertaining to the damage location can be obtained through benchmarking reference signals obtained from the intact status, as

$$r^{\text{measured-damage}}(t) - r^{\text{measured-intact}}(t) = r^{\text{scattered}}(t) + w(t) = r^{\text{residual}}(t), \tag{5.6}$$

where $w(t)$ is the difference between the two noise terms $w^{\text{measured-intact}}(t)$ and $w^{\text{measured-damage}}(t)$ in the intact and current statuses. Here, for convenience of discussion, the terms of $r^{\text{scattered}}(t) + w(t)$ is referred to as the *residual signal*.

5.3 Near-Field MUSIC Algorithm

As schematically illustrated in **Figure 5.1**, Lamb wave is excited at a foreknown position *P*, scattered by the damage, and then received by a linear sensor array that consisting of *K* transducing elements with a uniform element spacing *l*. Based on Fresnel region theory, the near-field monitoring scenario is defined when the distance between the array and the damage site satisfies[161]:

$$0.62\sqrt{\frac{D^3}{\lambda}} < R_{near} < \frac{2D^2}{\lambda}, \tag{5.7}$$

where $D = (K-1)\cdot l$ the array aperture and λ is the wavelength. Under this situation, the wavefront scattered by the damage is naturally spherical, which is characterized by the azimuth θ and the range *d*.

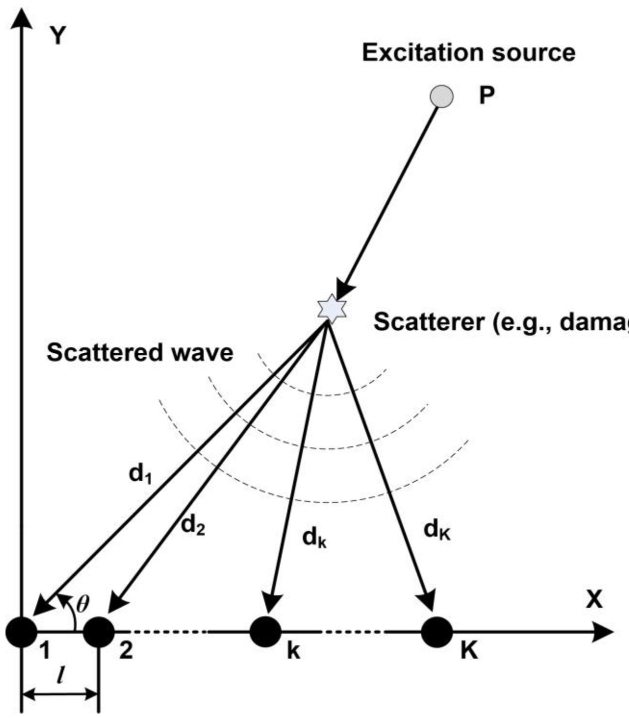

Figure 5.1 Use of a linear array with *K* PZT wafers for evaluation of damage in a near-field inspection region.

According to Equation (5.3), the scattered signal received by the first array element, $r_1^{\text{scattered}}(t)$, is expressed as

$$r_1^{\text{scattered}}(t) = \frac{d_0}{\sqrt{d_1}} s(t - \frac{d_1}{c}) = \frac{d_0}{\sqrt{d_1}} u(t - \frac{d_1}{c}) \exp^{i\omega_0 (t - \frac{d_1}{c})}, \tag{5.8}$$

where d_0 signifies an initial distance with regard to which the wave attenuation is calibrated, d_1 signifies the distance from the wave source through the damage and then to the first array element. Let $\tau_k = \frac{d_1 - d_k}{c}$ (*i.e.*, the time delay between two arrival signals captured by the first and the k^{th} (k=1, 2, …, K) element in the array), and then the scattered wave signal received by the k^{th} element, $r_k^{\text{scattered}}(t)$, can be expressed as

$$r_k^{\text{scattered}}(t) = \frac{d_0}{\sqrt{d_k}} s(t - \frac{d_k}{c}) = \frac{d_0}{\sqrt{d_k}} u(t - \frac{d_k}{c}) \exp^{i\omega_0 (t - \frac{d_k}{c})} = \frac{d_0}{\sqrt{d_k}} u(t - \frac{d_1}{c} + \tau_k) \exp^{i\omega_0 (t - \frac{d_1}{c} + \tau_k)}, \quad (k = 1, 2, \ldots, K). \tag{5.9}$$

With the assumption that the array element spacing l is sufficiently small (namely, $l \le \lambda / 2$, where λ is the wavelength of wave signal), $r_k^{\text{scattered}}(t)$ can be obtained based on the first element scattered signal $r_1^{\text{scattered}}(t)$ (defined in Equation (5.8)) as

$$\begin{aligned} r_k^{\text{scattered}}(t) &= \frac{d_0}{\sqrt{d_k}} u(t - \frac{d_1}{c} + \tau_k) \exp^{i\omega_0 (t - \frac{d_1}{c} + \tau_k)} \\ &\approx \frac{d_0}{\sqrt{d_k}} u(t - \frac{d_1}{c}) \exp^{i\omega_0 (t - \frac{d_1}{c} + \tau_k)} \\ &= \sqrt{\frac{d_1}{d_k}} r_1^{\text{scattered}}(t) \exp^{i\omega_0 \tau_k}. \end{aligned} \tag{5.10}$$

According to the cosine theorem [162] and second-order Taylor expansion [163], τ_k can be re-written as

$$\tau_k = \frac{d_1 - d_k}{c} = \frac{d_1 - \sqrt{d_1^{\,2} + (k-1)^2 l^2 - 2d_1(k-1)l\cos\theta}}{c}$$
$$= \frac{l\cos\theta}{c}(k-1) + (\frac{-l^2}{2cd_1}\sin^2\theta)(k-1)^2 + O(\frac{l^2}{d_1^{\,2}}), \tag{5.11}$$

where $O(\frac{l^2}{d_1^{\,2}})$ denotes those terms, the order of which is greater than or equal to $\frac{l^2}{d_1^{\,2}}$. Using the second-order Taylor series approximation, the scattered wave signal received by the k^{th} element retreats to

$$r_k^{\text{scattered}}(t) = \sqrt{\frac{d_1}{d_k}} r_1^{\text{scattered}}(t)\exp^{i\omega_0\tau_k}$$
$$= \sqrt{\frac{d_1}{d_k}} r_1^{\text{scattered}}(t)\exp^{i\omega_0(\frac{l\cos\theta}{c}(k-1)+(\frac{-l^2}{2cd_1}\sin^2\theta)(k-1)^2)}. \tag{5.12}$$

Letting $b_k(d_1,\theta) = \sqrt{\frac{d_1}{d_k}}\exp^{i\omega_0(\frac{l\cos\theta}{c}(k-1)+(\frac{-l^2}{2cd_1}\sin^2\theta)(k-1)^2)}$, as the array steering factor for the k^{th} scattered signal, and recalling the noise term in Equation (5.6), the k^{th} residual signal, $r_k^{\text{residual}}(t)$, can be expressed as

$$r_k^{\text{residual}}(t) = b_k(d_1,\theta) r_1^{\text{scattered}}(t) + w_k(t). \tag{5.13}$$

For the linear array with *K* elements, the residual signal vector $\mathbf{R}^{\text{residual}}(t)$ can thus be obtained and expressed in a signal representation matrix, which reads

$$\mathbf{R}^{\text{residual}}(t) = \mathbf{B}(d_1,\theta) r_1^{\text{scattered}}(t) + \mathbf{W}(t), \tag{5.14}$$

where

$$\mathbf{R}^{\text{residual}}(t) = [r_1^{\text{residual}}(t), \cdots, r_k^{\text{residual}}(t), \cdots, r_K^{\text{residual}}(t)]^T,$$

$$\mathbf{B}(d_1,\theta)=[b_1(d_1,\theta),\cdots,b_k(d_1,\theta),\cdots,b_K(d_1,\theta)]^T$$

$$=\begin{bmatrix} 1 \\ \vdots \\ \sqrt{\dfrac{d_1}{d_k}}\exp^{i\omega_0(\frac{l\cos\theta}{c}(k-1)+(\frac{-l^2}{2cd_1}\sin^2\theta)(k-1)^2)} \\ \vdots \\ \sqrt{\dfrac{d_1}{d_K}}\exp^{i\omega_0(\frac{l\cos\theta}{c}(K-1)+(\frac{-l^2}{2cd_1}\sin^2\theta)(K-1)^2)} \end{bmatrix},$$

$$\mathbf{W}(t)=[w_1(t),\cdots,w_k(t),\cdots,w_K(t)]^T\ .$$

Prevailing MUSIC-based damage imaging approaches have been developed by virtue of the signal representation matrix as defined in Equation (5.14). They, in general, present the following limitations during practical implementation:

i) In Equation (5.10), the operation of approximation, $u(t-\frac{d_1}{c}+\tau_k)\approx u(t-\frac{d_1}{c})$, lies in the premise that τ_k is negligibly small. To accommodate such a pre-requisite, the element spacing in the phased array must be sufficiently small ($l \le \lambda/2$), leading to a uniform and dense configuration of the transducing elements. The dense configuration incurs challenge in scanning the entire inspection region with an azimuth ranging from 0° to 180°, because the beamforming efficiency is severely degraded at the angles which are close to 0° or 180°. In most circumstances, those regions where the scanning angles are in the range of [0, 30] or [150, 180] are deemed blind zones [33], in which damage may be overridden; and

ii) In Equation (5.12), the steering vector is approximated using the second-order Taylor approximation, and the range error introduced by such approximation is remarkable when the damage is close to the array. For a range that is smaller than twice the array length (*i.e.*, the length from the first element to the k^{th} element), such error could be 10% or above due to such approximation [164]. In addition, the steering vectors at the scanning angles θ and $-\theta$ have the same value in Equation (5.12), resulting in a mirrored dummy of the true damage which is located symmetrically with regard to the array surface.

5.4 Am-MUSIC with A Sparse Sensor Network

Aimed at circumventing the above key limitations that conventional MUSIC-based damage imaging possesses, the original MUSIC algorithm is revamped. Different from the use of a linear phased array, we allow a sparse sensor network with individual transducers that are randomly positioned. Without loss of generality, consider a sparse sensor network comprising Q PZT wafers (labelled as PZT-*1*, PZT-*2*, …, PZT-*j*, …, PZT-*Q*), as shown in **Figure 5.2**. Positioned at an arbitrary location within the inspection region, each PZT wafer acts as either a wave transmitter or a wave receiver, leading to $M = Q(Q-1)$ transmitter–receiver sensing paths in the sensor network. Provided damage exists at pixel (x, y) within the inspection area, the propagation distance, d_{mxy}, for a Lamb wave, which is generated by the i^{th} transmitter at (x_i, y_i), scattered by damage at (x, y) and then propagates to the j^{th} receiver at (x_j, y_j), is

$$d_{mxy} = \sqrt{(x-x_i)^2+(y-y_i)^2} + \sqrt{(x-x_j)^2+(y-y_j)^2} = c \cdot t_{mxy}, \tag{5.15}$$

and t_{mxy} is the time for the wave traveling along the scattered path.

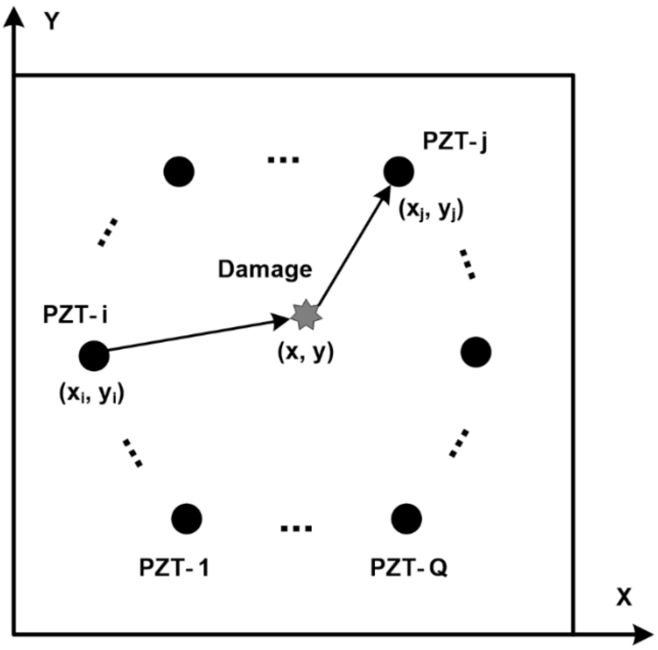

Figure 5.2 A plate waveguide with a sparse sensor network of Q PZT wafers.

Therefore, the scattered signal received by the m^{th} transmitter–receiver pair, $r_m^{\text{scattered}}(t)$, can be written according to Equation (5.3) as

$$r_m^{\text{scattered}}(t) = \frac{d_0}{\sqrt{d_{mxy}}} s(t - \frac{d_{mxy}}{c}) \quad (m = 1, 2, \cdots, M). \tag{5.16}$$

Equation (5.16) argues that for M transmitter–receiver pairs rendered by the sensor network, different scattering paths feature different degrees of time delay. A time shift, t_{mxy}, is then applied to the m^{th} scattered signal $r_m^{\text{scattered}}(t)$ in Equation (5.16), as

$$r_m^{\text{scattered}}(t + t_{mxy}) = \frac{d_0}{\sqrt{d_{mxy}}} s(t - \frac{d_{mxy}}{c} + t_{mxy}) = \frac{d_0}{\sqrt{d_{mxy}}} s(t). \tag{5.17}$$

Letting $a_{mxy} = \frac{d_0}{\sqrt{d_{mxy}}}$ (a_{mxy} is referred to as the *array steering factor* for the m^{th} scattered signal in what follows), Equation (5.17) can be rewritten as

$$r_m^{\text{scattered}}(t + t_{mxy}) = a_{mxy} s(t). \tag{5.18}$$

With the noise term ($w(t)$ in Equation (5.6)) in consideration, the residual signal vector for a total of M received signals which are respectively scattered by the damage at the pixel (x, y), $\mathbf{R}_{xy}^{\text{residual}}(t)$, can be expressed as the signal representation matrix

$$\mathbf{R}_{xy}^{\text{residual}}(t) = \mathbf{A}_{xy} s(t) + \mathbf{W}(t), \tag{5.19}$$

where

$$\mathbf{R}_{xy}^{\text{residual}}(t) = [r_1^{\text{residual}}(t + t_{1xy}), \cdots, r_m^{\text{residual}}(t + t_{mxy}), \cdots, r_M^{\text{residual}}(t + t_{Mxy})]^T,$$

$$\mathbf{A}_{xy} = [a_{1xy}, \cdots, a_{mxy}, \cdots, a_{Mxy}]^T,$$

$$\mathbf{W}(t) = [w_1(t + t_{1xy}), \cdots, w_m(t + t_{mxy}), \cdots, w_M(t + t_{Mxy})]^T.$$

Equation (5.19) implies that after compensating for the time delay to each residual signal, the residual signal vector can be defined using the excitation signal series, instead of using the scattered signal series as a conventional MUSIC algorithm does (Equation (5.14)). It is such a merit of the ameliorated MUSIC (Am-MUSIC) algorithm that enables the use of a sparse sensor network with arbitrarily positioned transducers.

Recalling the MUSIC algorithm, the covariance matrix $\mathbf{C}$ of the residual signal vector at pixel (x, y) within the inspection region yields as

$$\begin{aligned}\mathbf{C} &= E[\mathbf{R}_{xy}^{\text{residual}}(t)\mathbf{R}_{xy}^{\text{residual}}(t)^H] \\ &= \mathbf{A}_{xy} E\left[s(t) \bullet s(t)^H\right]\mathbf{A}_{xy}{}^H + \mathbf{A}_{xy} E\left[s(t) \bullet \mathbf{W}(t)^H\right] \\ &\quad + E\left[\mathbf{W}(t) \bullet s(t)^H\right]\mathbf{A}_{xy}{}^H + E\left[\mathbf{W}(t) \bullet \mathbf{W}(t)^H\right],\end{aligned} \tag{5.20}$$

where $E[\ ]$ denotes covariance computation, and superscript H represents the complex conjugate transpose.

As the source signal and noise signal are uncorrelated and mutually independent, the covariance matrix $\mathbf{C}$ can be simplified as

$$\mathbf{C} = \mathbf{A}_{xy}\mathbf{R}_s\mathbf{A}_{xy}{}^H + \sigma^2\mathbf{I}, \tag{5.21}$$

where $\mathbf{R}_s = E\left[s(t) \bullet s(t)^H \right]$, and it signifies the covariance matrix of the source signal. σ^2 is noise power and $\mathbf{I}$ the covariance matrix of the noise signal. The covariance matrix $\mathbf{C}$ can be decomposed into two parts: namely a signal-related part and a noise-related part, as

$$\mathbf{C} = \mathbf{U\Sigma U}^H = \mathbf{U}_S\mathbf{\Sigma U}_S{}^H + \mathbf{U}_N\mathbf{\Sigma U}_N{}^H, \tag{5.22}$$

where $\mathbf{U} = [\mu_1, \mu_2, \cdots, \mu_M]$, and the columns of $\mathbf{U}$ are the singular vectors; $\mathbf{\Sigma}$ is a diagonal matrix with singular values arranged in descending order of magnitudes. Considering that $\mathbf{A}_{xy}$ is the steering vector at pixel (x, y) with the dimension of $M \times 1$ and $\mathbf{A}_{xy}\mathbf{R}_s\mathbf{A}_{xy}{}^H$ in Equation (5.21) is decomposed as $\mathbf{U}_S\mathbf{\Sigma U}_S{}^H$ in Equation (5.22), $\mathbf{U}_S = [\mu_1]$ denoting the signal subspace spanned by the eigenvectors corresponding to the first largest eigenvalue; and $\mathbf{U}_N = [\mu_2, \mu_3, \cdots, \mu_M]$, representing the noise subspace spanned by the eigenvectors corresponding to the remaining $M-1$ eigenvalues.

Based on Equations (5.21) and (5.22), the following expression can be obtained after multiplying the covariance matrix $\mathbf{C}$ with the noise subspace $\mathbf{U}_N$

$$\mathbf{A}_{xy}\mathbf{R}_s\mathbf{A}_{xy}{}^H\mathbf{U}_N = \mathbf{0}. \tag{5.23}$$

As $\mathbf{R}_s$ is a full rank matrix, Equation (5.23) is further simplified as

$$\mathbf{A}_{xy}\mathbf{R}_s\mathbf{A}_{xy}{}^H\mathbf{U}_N = \mathbf{0}. \tag{5.24}$$

Equation (5.24) argues that the steering vector $\mathbf{A}_{xy}$ at the position of damage is orthogonal with the noise subspace $\mathbf{U}_N$. This characteristic makes it possible for the Am-MUSIC to calculate the steering vector at each pixel across the entire inspection region and calibrate the degree of orthogonality between the steering vector and the noise subspace with the squared norm of vector $\mathbf{A}_{xy}{}^H\mathbf{U}_N$ as

$$\beta^2 = \left\|\mathbf{A}_{xy}{}^H\mathbf{U}_N\right\|^2 = \mathbf{A}_{xy}{}^H(\mathbf{U}_N\mathbf{U}_N{}^H)\mathbf{A}_{xy} \quad . \tag{5.25}$$

Taking a reciprocal of the squared norm expression creates a peak in the spatial spectrum that corresponds to the damage location. Am-MUSIC algorithm defines the pixel value ($P_{\text{Am-MUSIC}}(x, y)$) within the inspection region as

$$P_{\text{Am-MUSIC}}(x, y) = \frac{1}{\mathbf{A}_{xy}{}^H(\mathbf{U}_N\mathbf{U}_N{}^H)\mathbf{A}_{xy}} \; . \tag{5.26}$$

Equation (5.26) yields a full spatial spectrum for the inspection region, in which $P_{\text{Am-MUSIC}}(x, y)$ culminates at the damage location.

In summary, the complete procedure of the proposed Am-MUSIC algorithm is flowcharted in a nutshell in **Figure 5.3**.

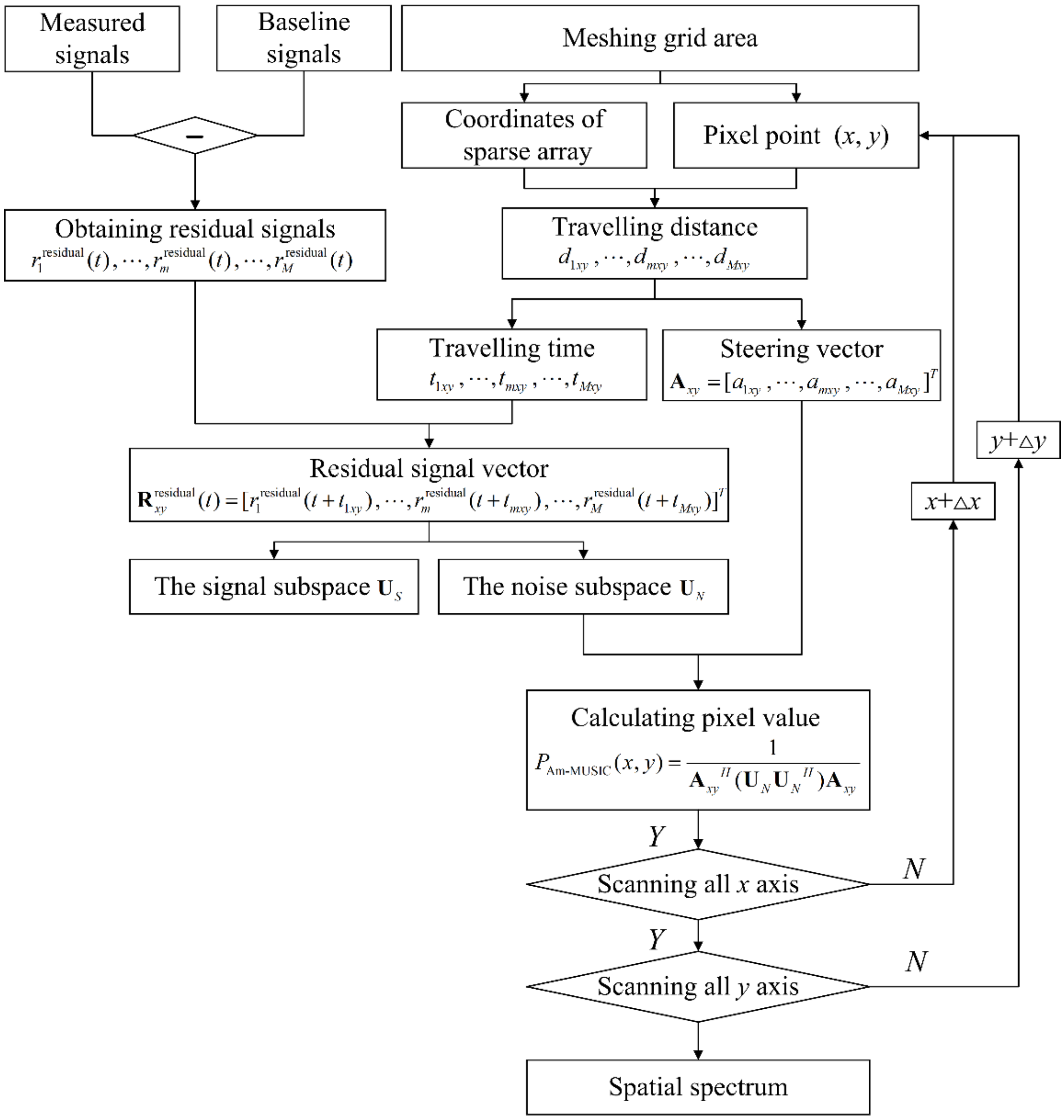

Figure 5.3 Key steps of Am-MUSIC algorithm.

5.5 Numerical Validation

To validate the developed Am-MUSIC algorithm for damage imaging, numerical simulation is implemented first. Consider a homogeneous, isotropic plate-like waveguide (density: ρ=2,700 kg/m^3; Young modulus: E=71 GPa; Poisson's ratio ν=0.33), measuring 500 mm × 500 mm × 2 mm. Atop the waveguide, there is a sparse sensor network with eight PZT wafers, as illustrated in **Figure 5.4(a)**. Each PZT wafer functions as either a wave transmitter or a wave receiver, leading to 56 transmitter-receiver sensing paths in the sensor network. For comparison against conventional MUSIC, another seven PZT wafers are arranged in a linear array as sensors, in **Figure 5.4(b)**, along with an additional PZT wafer as wave actuator placed at the position (250 mm, 400 mm). In all cases, a 5-cycle Hanning window toneburst with a central frequency 200 kHz signal is selected as the excitation signal to obtain S_0 wave mode, considering wave sensitivity and excitability. Total duration of 150 μs time length is analyzed for all numerical cases.

Damage in the simulation is introduced to the waveguide by enforcing the material local stiffness to be zero. Three damage sites, labelled as D1-D3, are simulated in the waveguide, with respective positions highlighted in **Figure 5.4**. With these damage sites, three damage cases (C-I – C-III) are created by including different damage sites, **Table 5.1**.

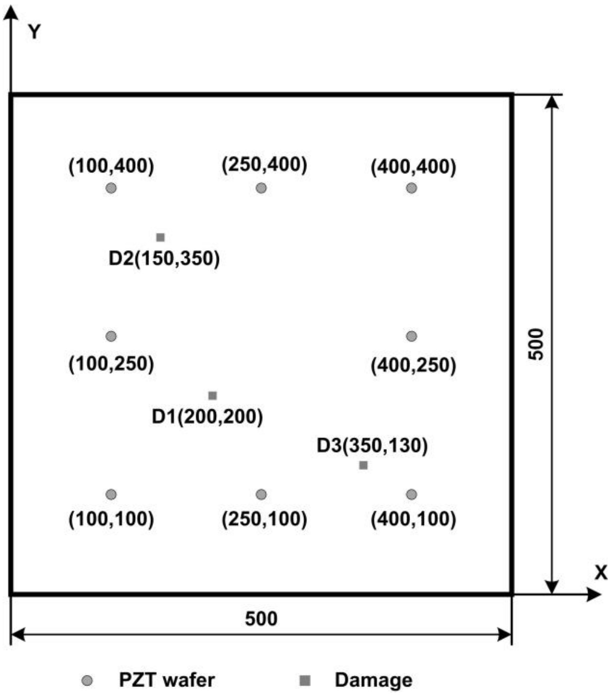

(a)

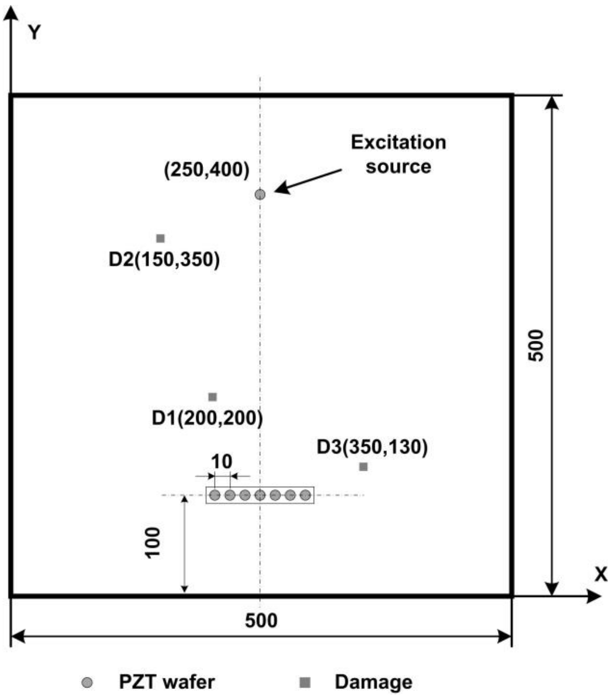

(b)

Figure 5.4 Schematics of the plate waveguide in simulation (all dimensions in mm): (a) with a sparse sensor network for Am-MUSIC algorithm; and (b) with a linear array for conventional MUSIC algorithm.

Table 5.1 Three damage cases in simulation

Damage case	Damage site	Position	
		x [mm]	y [mm]
C-I	D1	200	200
C-II	D2	150	350
C-III	D3	350	130

Figure 5. 5 (a) displays the spatial spectrum obtained using the Am-MUSIC algorithm, for C-I – the case with the damage site (D1), accurately pinpointing the damage location (200 mm, 200 mm). For comparison, the image constructed using the conventional MUSIC algorithm is shown in **Figure 5.5(b)**, indicating the damage location at (204 mm, 203 mm), which represents an error of (4 mm, 3 mm), in addition to an elongation artifact along the damage direction – a common deficiency for conventional MUSIC algorithms as illustrated elsewhere [36, 37, 150, 151, 155, 165]. The degree of such artifact depends on the point-spread function of the phased array at the location of the scatterer [166].

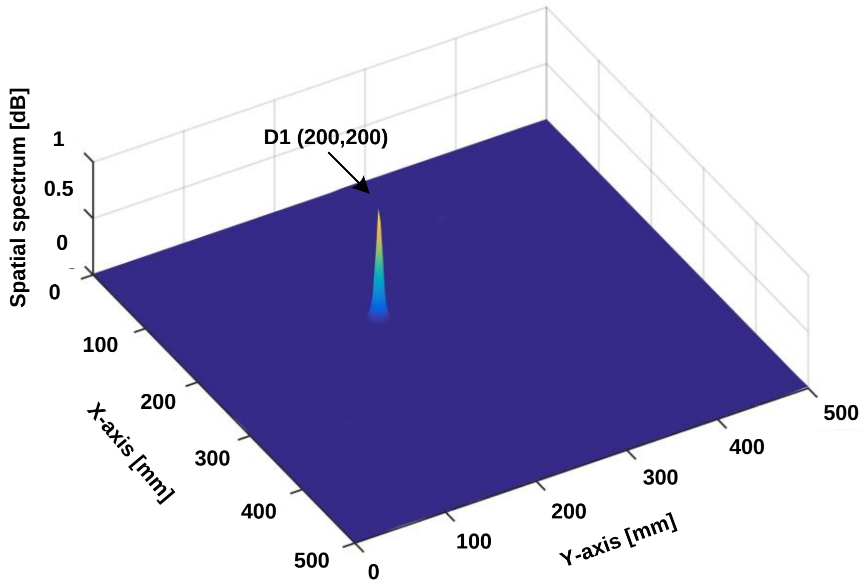

(a)

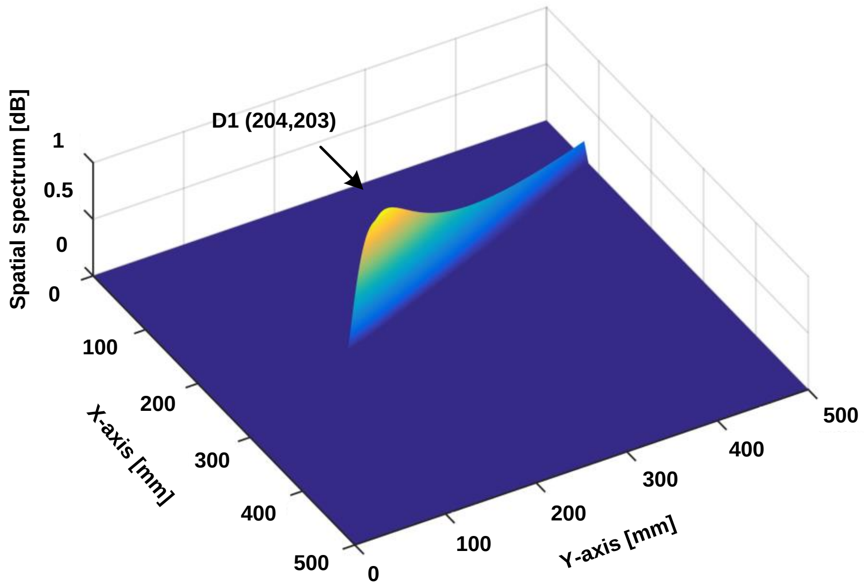

(b)

Figure 5.5 Spatial spectra for C-I obtained by (a) Am-MUSIC algorithm; and (b) conventional MUSIC algorithm.

Figure 5.6(a) shows the spectrum for C-II obtained using the Am-MUSIC. Again, the identified results are observed to coincide exactly with actual damage sites, contrasting the spatial spectrum obtained using the conventional MUSIC algorithm in **Figure 5.6(b)**, in which only the azimuth of damage is predicted. This is because the damage D2 fails to meet the near-field condition in Equation (5.7), which is located in the far-field inspection region ($R_{far} > \frac{2D^2}{\lambda}$), and Lamb wave emanating from the scatterer in the far-field region is treated as a plane wave when they arrive at the array (*i.e.*, only direction-of-arrival (DOA) can be estimated).

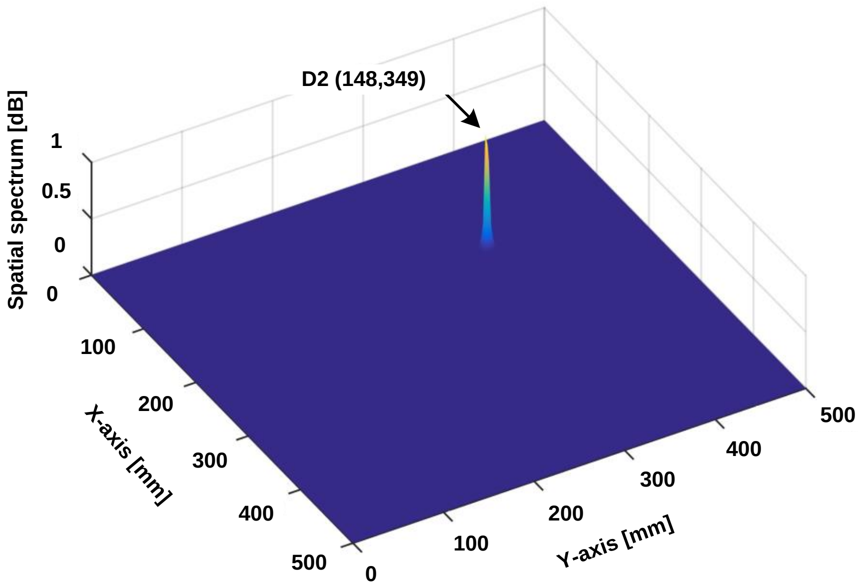

(a)

Figure 5.6 Spatial spectra for C-II obtained by (a) Am-MUSIC algorithm; and (b) conventional MUSIC algorithm.

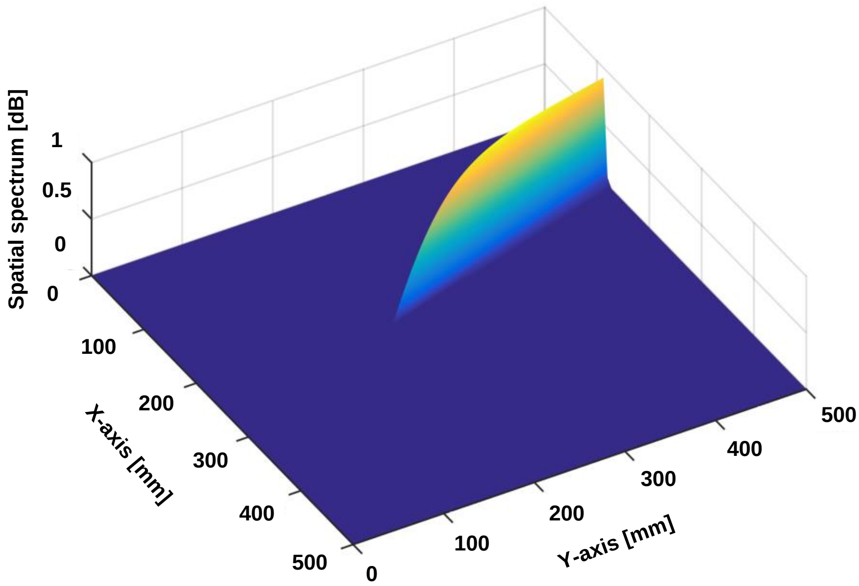

(b)

Figure 5.6 *Cont.*

Provided that damage site D3 at an angle of 16.7° with regard to the linear array – the case of C-III, the constructed spatial spectra using the Am-MUSIC method and conventional MUSIC method are compared in **Figure 5.7**. In **Figure 5.7(a)**, the damage site is localized precisely, in good agreement with the actual positions; however, the damage can barely be identified by the conventional MUSIC algorithm due to remarkable artifacts, in **Figure 5.7(b)**, implying that the conventional MUSIC method may fail to detect the damage site which is in the blind zone.

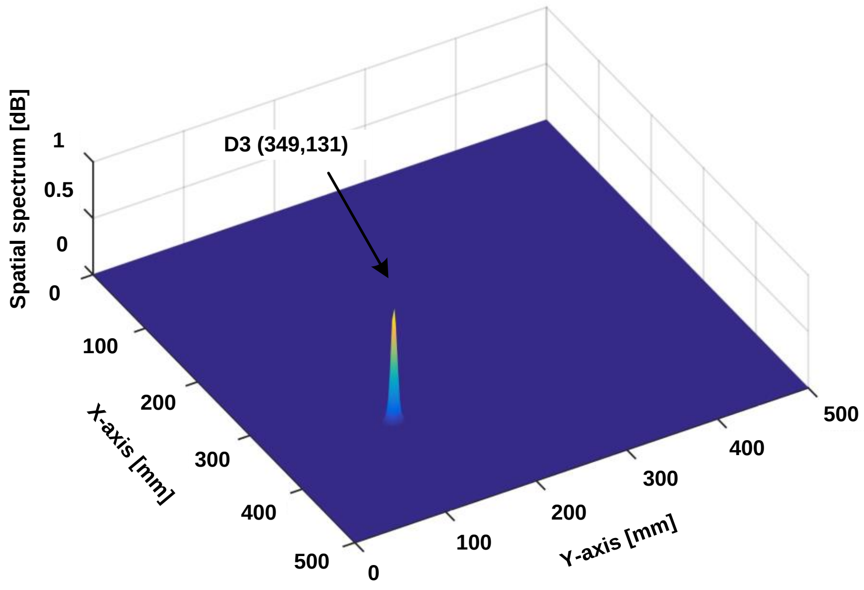

(a)

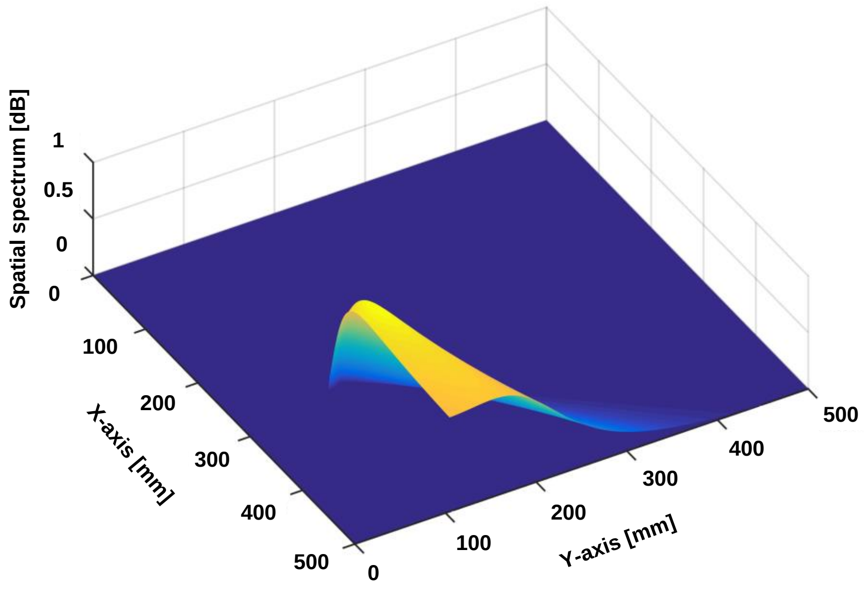

(b)

Figure 5.7 Spatial spectra for C-III obtained by (a) Am-MUSIC algorithm; and (b) conventional MUSIC algorithm.

5.6 Experimental Validation

Subsequent to numerical simulation, the effectiveness and accuracy of the Am-MUSIC-driven anomaly imaging are validated experimentally. A 2 mm-thick aluminum plate (dimensions: 1000 mm × 1000 mm × 2 mm; density: ρ=2700 kg/m^3; Young modulus: E=71 GPa; Poisson's ratio ν=0.33) is prepared. A sparse sensor network, consisting of eight PZT wafers (labelled as PZT-1, PZT-2, …, PZT-8), is surface-adhered on the plate, with the location of each wafer indicated in **Figure 5.8(a)**. The experimental set-up is shown in **Figure 5.8(b)**. The excitation signal – a Hanning-window-modulated 5-cycle toneburst at a central frequency of 200 kHz – is generated with an arbitrary waveform generator (NI® PXI-5412) and amplified by a linear power amplifier (Ciprian® US-TXP-3). The excitation signal is applied on each PZT wafer, in turn, to emit Lamb waves into the plate. S_0 mode Lamb wave signals, each in 300 μs, are acquired with a digital oscilloscope (NI® PXI-5105) at a sampling rate of 60 MHz.

Similar to the simulation in Section 5.5, three damage sites are considered in the experiment, as recapped in **Table 5.2**.

Table 5.2 Damage cases in experiments

Damage Case	Damage
E-I	A through-hole D1 at (400 mm, 400 mm) (Ø: 10 mm)
E-II	A through-hole D2 at (300 mm, 700 mm) (Ø: 10 mm)
E-III	A through-hole D3 at (740 mm, 250 mm) (Ø: 10 mm)

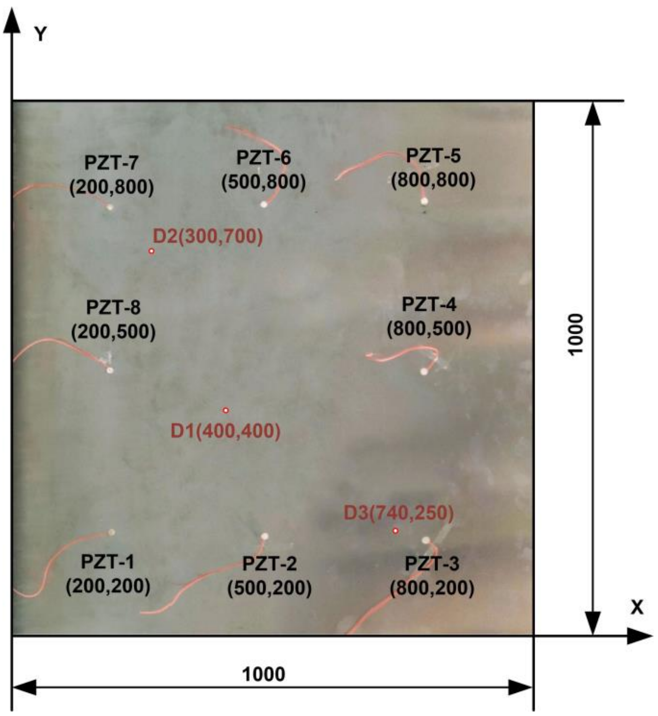

(a)

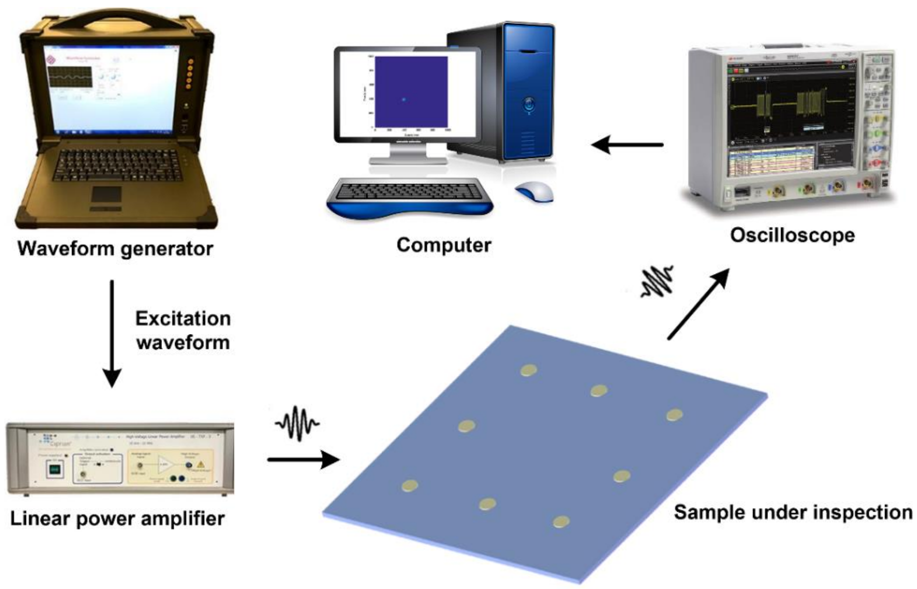

(b)

Figure 5.8 (a) An aluminum plate with a surface-adhered sparse sensor network consisting of eight PZT wafers in the experiment (red 'o': actual damage and all dimensions in mm); and (b) Experimental set-up.

The spatial spectra constructed using the Am-MUSIC algorithm for three damage cases are presented in **Figure 5.9**, in which all damage sites are accurately located with precise depiction of the damage shape, demonstrating the great capacity of the developed Am-MUSIC algorithm towards damage identification.

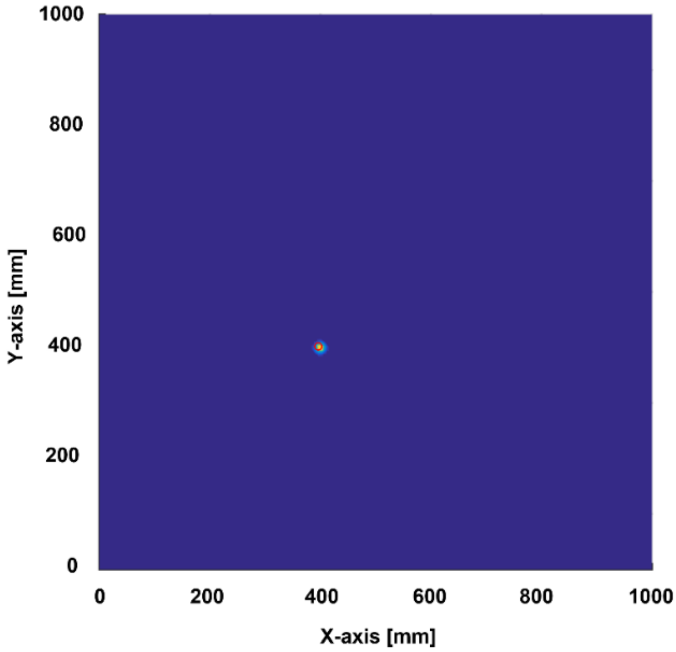

(a)

Figure 5.9 Spatial spectra constructed using Am-MUSIC algorithm for damage case (a) E-I; (b) E-II; (c) E-III (red ‘o’: actual damage).

Figure 5.9 Cont.

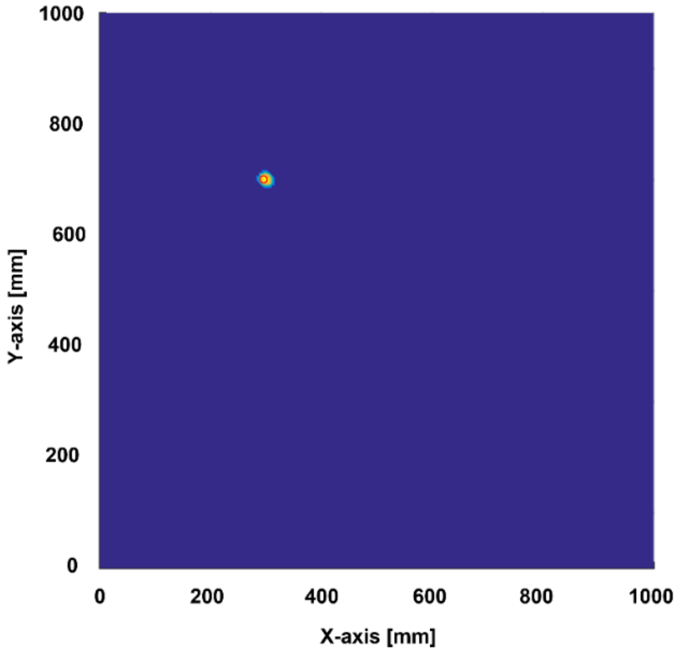

(b)

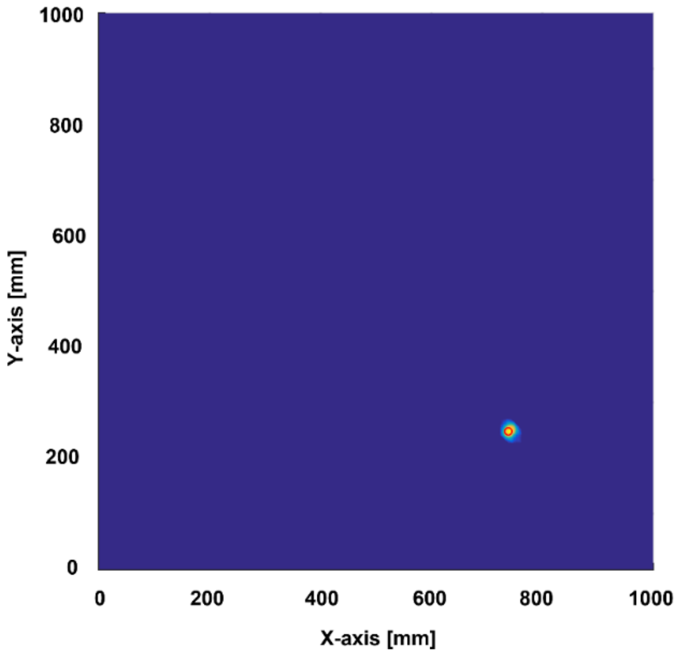

(c)

Figure 5.9 *Cont.*

To take a step further, the conventional MUSIC algorithm in junction with the use of a linear array is recalled for comparison. Seven PZT wafers are configured in a linear array as receivers, in **Figure 5.10**, along with an additional PZT wafer as a wave actuator placed at the position (500 mm, 800 mm). For the same damage cases, the spatial spectra constructed using the conventional MUSIC algorithm are shown in **Figure 5.11**, showing inferior accuracy in damage localization and sizing; moreover, it fails to identify damage D3 in E-III that is located in the blind zone for a conventional MUSIC algorithm.

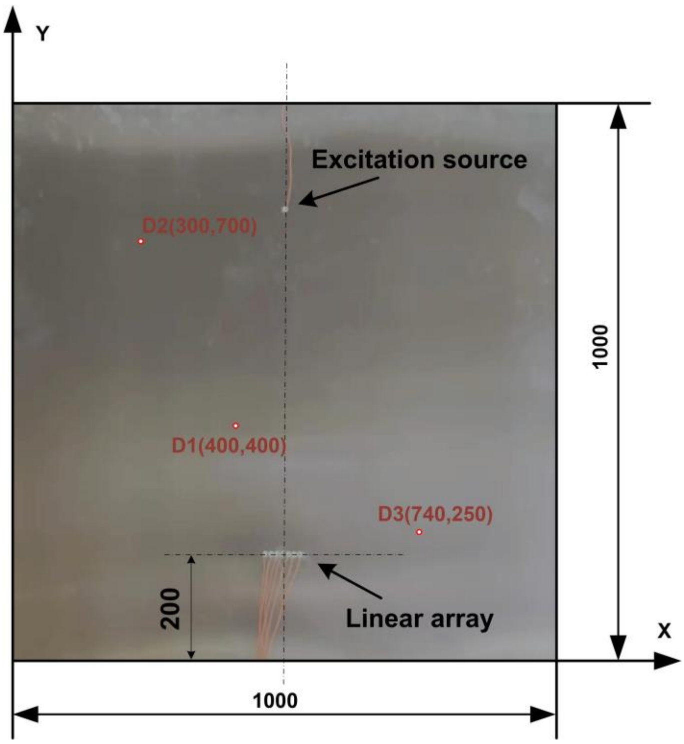

Figure 5.10 An aluminum plate with a surface-adhered linear array consisting of 7 PZT wafers in the experiment (red ‘o’: actual damage and all dimensions in mm).

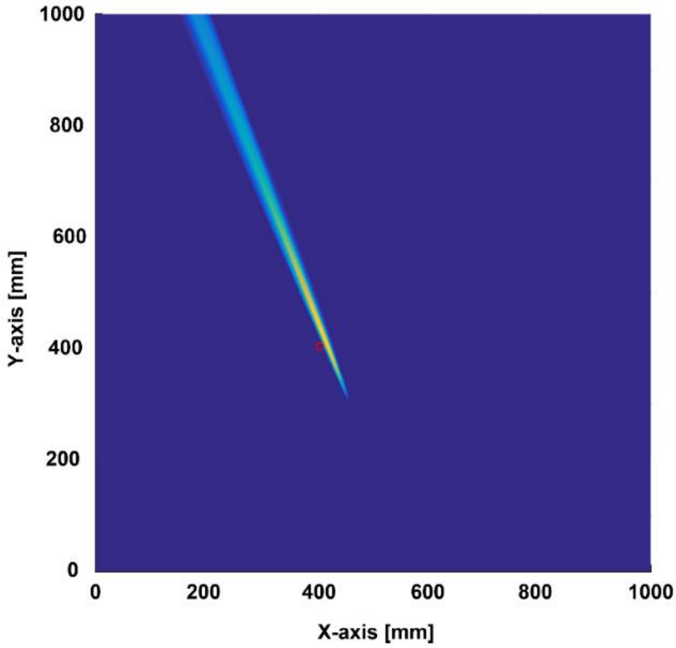

(a)

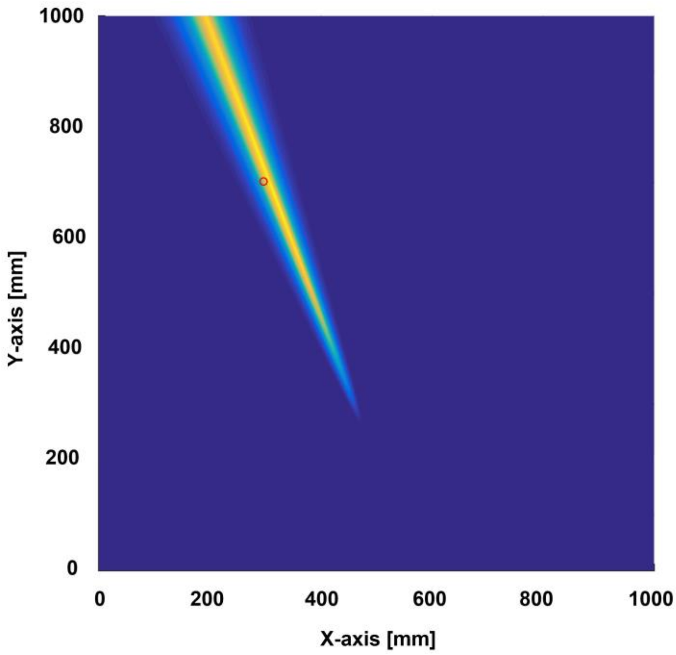

(b)

Figure 5.11 Spatial spectra constructed using conventional MUSIC algorithm for damage case (a) E-I; (b) E-II; and (c) E-III (red ‘o’: actual damage).

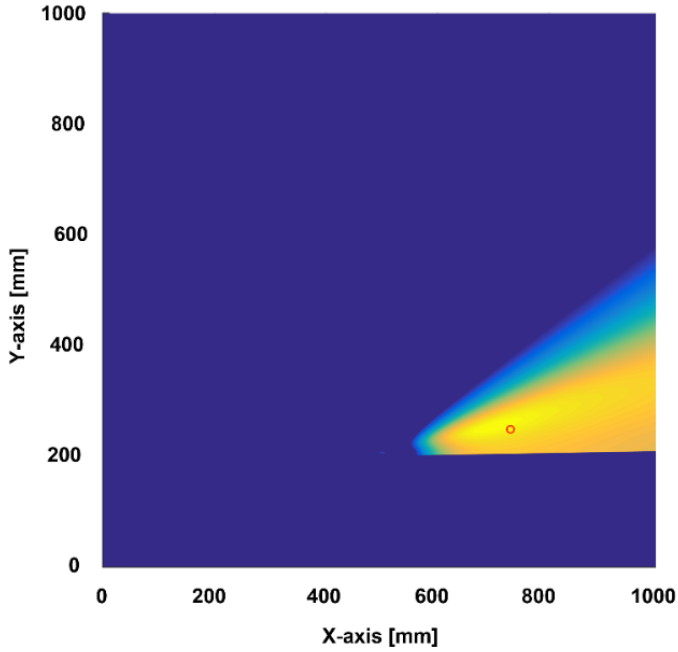

(c)

Figure 5.11 *Cont.*

5.7 Summary

Aimed to circumvent some critical limitations of the conventional MUSIC algorithm-based damage imaging, an ameliorated MUSIC algorithm is developed. In the Am-MUSIC algorithm, the signal representation matrix at each pixel is manipulated by the excitation signal series, instead of the scattered signal series, which enables the use of a sparse sensor network with arbitrarily positioned transducers rather than a linear array featuring a dense configuration of transducing elements with a uniform element pitch. By quantifying the orthogonal attributes between the signal subspace and noise subspace inherent in the signal representation matrix, a full spatial spectrum of the inspected sample can be generated, to visualize damage in the sample. The effectiveness and accuracy of the Am-MUSIC algorithm are verified in both simulation and experiment. Results show that compared with the conventional MUSIC methods, the Am-MUSIC algorithm is capable of improving the detectability and eliminating blind zones, conducive to expanding conventional MUSIC from phased array-facilitated nondestructive evaluation to *in-situ* health monitoring using built-in sparse sensor networks.

CHAPTER 6

Imaging Damage in Plate Waveguides Using Frequency-domain Multiple Signal Classification (F-MUSIC)

6.1 Introduction

In the previous chapter, an ameliorated MUSIC (Am-MUSIC) algorithm is developed, aimed at expanding conventional MUSIC algorithm from linear array-facilitated nondestructive evaluation to *in-situ* health monitoring with a sparse sensor network. Yet, Am-MUSIC leaves a twofold issue to be improved: i) the signal representation equation is constructed at each pixel across the inspection region, incurring high computational cost; and ii) the algorithm is applicable to monochromatic excitation only, ignoring signal features scattered out of the excitation frequency band which also carry information on structural integrity. With this motivation, a multiple-damage-scattered wavefield model is developed, with which the signal representation equation is constructed in the frequency domain, avoiding computationally expensive pixel-based calculation – referred to as frequency-domain MUSIC (F-MUSIC). F-MUSIC quantifies the orthogonal attributes between the signal subspace and noise subspace inherent in the signal representation equation, and generates a full spatial spectrum of the inspected sample to visualize damage. Modeling in the frequency domain endows F-MUSIC with the capacity to fuse rich information scattered in a broad band and therefore enhances imaging precision. Both simulation and experiment are performed to validate F-MUSIC when used for imaging single and multiple sites of damage in a plate waveguide with a sparse sensor network.

6.2 Principle of Methodology

Consider a monochronic Lamb wave guided by a plate waveguide, $f(t)$. Upon propagating the distance of *d*, without considering the attenuation, the received signal, $r(t)$, is governed by

$$r(t)=\int_{-\infty}^{\infty} F(\omega) e^{-ik(\omega)d} \exp^{i\omega t} \, d\omega, \tag{6.1}$$

where $F(\omega)$ is the Fourier transform of $f(t)$ in the frequency domain, *t* the time, ω the angular frequency, i the imaginary unit, and $k(\omega)$ the wavenumber of the Lamb wave ($k(\omega)=\omega/c_p(\omega)$, where $c_p(\omega)$ is the phase velocity). Applying Fourier transform on Equation (6.1), $r(t)$ in the frequency domain, $R(\omega)$, is obtained by

$$R(\omega)=F(\omega)\exp^{-ik(\omega)d}=F(\omega)\exp^{-i\omega d/c_p(\omega)}. \tag{6.2}$$

Assuming a wave scatterer (*e.g.,* damage) in the waveguide, the scatterer can be modeled as a secondary wave source to scatter incoming $f(t)$ and interfere with the original wavefield of signal $f(t)$; and the scattered wavefield $R^{\text{scattered}}(\omega)$ in the frequency domain can be defined by modulating the original wavefield with a scattering coefficient related to the scatterer, as

$$R^{\text{scattered}}(\omega)=\alpha(\omega)F(\omega)\exp^{-i\omega d^{\text{scattered}}/c_p(\omega)}, \tag{6.3}$$

where $\alpha(\omega)$ is the scattering coefficient in the frequency domain [160], and $d^{\text{scattered}}$ is the distance from the excitation source to the scatterer and then to the wave receiver.

Discuss a sparse sensor network with Q piezoelectric lead zirconate titanate (PZT) wafers (labelled as PZT-*1*, …, PZT-*i*, …, PZT-*Q*) ($i=1,2,\ldots,Q$) surface-mounted on the plate waveguide, as shown schematically in **Figure 6.1**. With an arbitrary position on the waveguide, each wafer functions as a wave transmitter and a wave receiver as well. Thus, this sensor network renders $M=Q(Q-1)$ transmitter–receiver paths, and the m^{th} transmitter–receiver path ($m=1,2,\ldots,M$) links PZT-*i* (as wave transmitter) and PZT-*j* (as wave receiver).

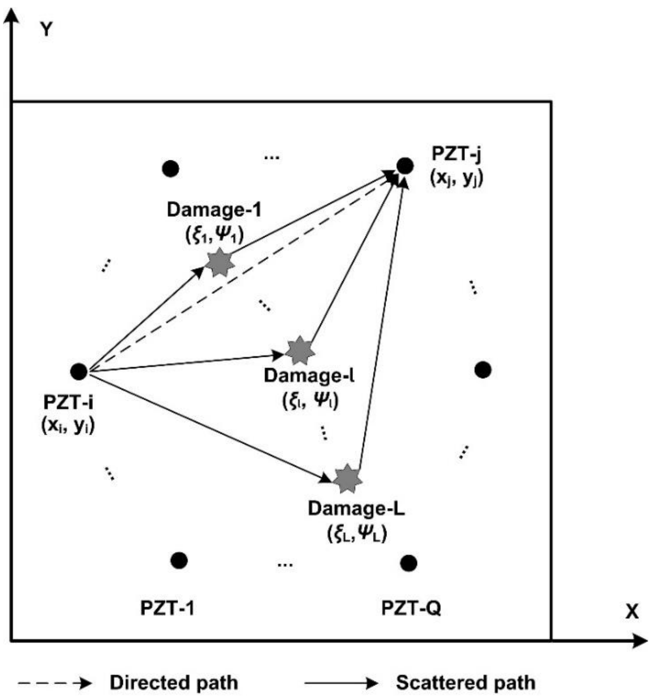

Figure 6.1 A plate waveguide with a sparse sensor network of *Q* PZT wafers and *L* damage sites.

For an intact waveguide, the wave signal, captured by the m^{th} transmitter–receiver path (denoted with $r_m^{\text{measured-intact}}(t)$), is the direct arrival wave $r_m^{\text{direct}}(t)$, boundary-reflection wave $r_m^{\text{boundary-reflection}}(t)$ with incoherent noise $w_m^{\text{measured-intact}}(t)$, as

$$r_m^{\text{measured-intact}}(t) = r_m^{\text{direct}}(t) + r_m^{\text{boundary-reflection}}(t) + w_m^{\text{measured-intact}}(t), \quad \left(m = 1, 2, \ldots, M\right). \quad (6.4)$$

Assume that up to L damage sites co-exist in the waveguide which are respectively located at $(\xi_1, \psi_1), \cdots, (\xi_l, \psi_l), \cdots, (\xi_L, \psi_L)$. Ignoring mode conversion and multiple reflections among damage sites, the wave signal captured by the same transmitter-receiver path, $r_m^{\text{measured-damage}}(t)$, embraces the direct arrival waves $r_m^{\text{direct}}(t)$, boundary-reflection wave $r_m^{\text{boundary-reflection}}(t)$, damage-scattered waves $r_m^{\text{scattered},l}(t), \left(l = 1, 2, \ldots, L\right)$ from all damage sites, and the incoherent noise $w_m^{\text{measured-damage}}(t)$, as

$$r_m^{\text{measured-damage}}(t) = r_m^{\text{direct}}(t) + r_m^{\text{boundary-reflection}}(t) + \sum_{l=1}^{L} r_m^{\text{scattered},l}(t) + w_m^{\text{measured-damage}}(t), \quad \left(m = 1, 2, \ldots, M\right), \quad (6.5)$$

where $r_m^{\text{scattered},l}(t)$ represents the wave signal that propagates from PZT-*i* (as wave transmitter) to the l^{th} damage site and then to PZT-*j* (as wave receiver).

Benchmarking against the intact waveguide, one has,

$$r_m^{\text{measured-damage}}(t) - r_m^{\text{measured-intact}}(t) = \sum_{l=1}^{L} r_m^{\text{scattered},l}(t) + w_m(t) = r_m^{\text{residual}}(t), \quad \left(m = 1, 2, \ldots, M\right) \quad (6.6)$$

where $w_m(t)$ signifies the difference between two noise terms, $w_m^{\text{measured-damage}}(t) - w_m^{\text{measured-intact}}(t)$. To facilitate discussion in what follows, the term, $\sum_{l=1}^{L} r_m^{\text{scattered},l}(t) + w_m(t)$, is referred to as the m^{th} residual signal $r_m^{\text{residual}}(t)$.

Applying Fourier transform on Equation (6.6) and substituting Equation (6.3) to (6.6), the m^{th} residual signal in the frequency domain, $R_m^{\text{residual}}(\omega)$, is obtained as

$$R_m^{\text{residual}}(\omega) = \sum_{l=1}^{L} \alpha^l(\omega) F(\omega) \exp^{-i\omega d_m^l / c_p(\omega)} + W_m(\omega), \qquad \left(m = 1, 2, \ldots, M\right) \quad (6.7)$$

where $\alpha^l(\omega)$ denotes the scattering coefficient for the l^{th} damage site within the inspection region; $d_m^l = \sqrt{(\xi_l - x_i)^2 + (\psi_l - y_i)^2} + \sqrt{(\xi_l - x_j)^2 + (\psi_l - y_j)^2}$, which represents the distance from the i^{th} wave transmitter to the l^{th} damage and then to the j^{th} wave receiver; $W_m(\omega)$ is the Fourier counterpart of $w_m(t)$ in the frequency domain.

Defining that $\hat{F}_l(\omega) = \alpha^l(\omega) F(\omega)$ and $a_m^l(\omega) = \exp^{-i\omega d_m^l / c_p(\omega)}$, both of which are related to the l^{th} damage site, the residual signal $R_m^{\text{residual}}(\omega)$ can be rewritten, in the frequency domain, as

$$R_m^{\text{residual}}(\omega) = \sum_{l=1}^{L} a_m^l(\omega) \hat{F}_l(\omega) + W_m(\omega). \qquad \left(m = 1, 2, \ldots, M\right) \quad (6.8)$$

Extending the above manipulation to all the available M transmitter–receiver paths in the sensor network, it has

$$\mathbf{R}^{\text{residual}}(\omega) = \begin{bmatrix} R_1^{\text{residual}}(\omega) \\ \vdots \\ R_m^{\text{residual}}(\omega) \\ \vdots \\ R_M^{\text{residual}}(\omega) \end{bmatrix}_{M\times 1} = \begin{bmatrix} a_1^1(\omega) & \cdots & a_1^l(\omega) & \cdots & a_1^L(\omega) \\ \vdots & & \vdots & & \vdots \\ a_m^1(\omega) & \cdots & a_m^l(\omega) & \cdots & a_m^L(\omega) \\ \vdots & & \vdots & & \vdots \\ a_M^1(\omega) & \cdots & a_M^l(\omega) & \cdots & a_M^L(\omega) \end{bmatrix}_{M\times L} \begin{bmatrix} \hat{F}_1(\omega) \\ \vdots \\ \hat{F}_l(\omega) \\ \vdots \\ \hat{F}_L(\omega) \end{bmatrix}_{L\times 1} + \begin{bmatrix} W_1(\omega) \\ \vdots \\ W_m(\omega) \\ \vdots \\ W_M(\omega) \end{bmatrix}_{M\times 1} .$$

(6.9)

where $\mathbf{R}^{\text{residual}}(\omega) = [R_1^{\text{residual}}(\omega), \cdots, R_m^{\text{residual}}(\omega), \cdots, R_M^{\text{residual}}(\omega)]^T$ the residual signal vector for the entire sensor network. Defining that

$\mathbf{a}_l(\omega)=[a_1^l(\omega),\cdots,a_m^l(\omega),\cdots,a_M^l(\omega)]^T$ as the steering vector for the l^{th} damage site, $\mathbf{A}(\omega)=[\mathbf{a}_1(\omega),\cdots,\mathbf{a}_l(\omega),\cdots,\mathbf{a}_L(\omega)]$ as the steering vector dictionary for all damage sites, $\mathbf{F}(\omega)=[\hat{F}_1(\omega),\cdots,\hat{F}_l(\omega),\cdots,\hat{F}_L(\omega)]^T$ as the excitation signal vector, and $\mathbf{W}(\omega)=[W_1(\omega),\cdots,W_m(\omega),\cdots,W_M(\omega)]^T$ as the noise term, Equation (6.9) is

$$\mathbf{R}^{\text{residual}}(\omega)=\mathbf{A}(\omega)\mathbf{F}(\omega)+\mathbf{W}(\omega). \tag{6.10}$$

Equation (6.10) defines all wave signals received by the entire sensor network, containing multiple damage-scattered wave components. It is referred to as a *multiple-damage-scattered wavefield model* over the frequency domain. With this model, the residual signal series can be expressed with the excitation signal series, which is independent of the location of a wave receiver. It is such merit that allows arbitrarily positioning sensors in the sensor network – difficult to fulfill by conventional MUSIC algorithms which are largely bound up with the use of a dense, linear array with a uniform element pitch. Equation (6.10) also serves as the theoretical cornerstone for the F-MUSIC, as detailed as below.

Recalling the conventional MUSIC algorithm, the covariance matrix $\mathbf{C}(\omega)$ of the residual signal vector $\mathbf{R}^{\text{residual}}(\omega)$ is defined as

$$\begin{aligned}\mathbf{C}(\omega)&=E\left[\mathbf{R}^{\text{residual}}(\omega)\bullet\mathbf{R}^{\text{residual}}(\omega)^H\right]\\&=\mathbf{A}(\omega)E\left[\mathbf{F}(\omega)\bullet\mathbf{F}(\omega)^H\right]\mathbf{A}(\omega)^H+\mathbf{A}(\omega)E\left[\mathbf{F}(\omega)\bullet\mathbf{W}(\omega)^H\right]\\&\quad+E\left[\mathbf{W}(\omega)\bullet\mathbf{F}(\omega)^H\right]\mathbf{A}(\omega)^H+E\left[\mathbf{W}(\omega)\bullet\mathbf{W}(\omega)^H\right],\end{aligned} \tag{6.11}$$

where $E[\bullet]$ is covariance computation and the superscript H the complex conjugate transpose. As the source signal is un-correlated to a noise signal, both $E\left[\mathbf{F}(\omega)\bullet\mathbf{W}(\omega)^H\right]$ and $E\left[\mathbf{W}(\omega)\bullet\mathbf{F}(\omega)^H\right]$ retreat to zero. The noise, $\mathbf{W}(\omega)$, is commonly a Gaussian white noise which satisfies $E\left[\mathbf{W}(\omega)\bullet\mathbf{W}(\omega)^H\right]=\sigma^2\mathbf{I}(\omega)$, where σ^2 is noise power and $\mathbf{I}(\omega)$ the identity matrix. Therefore, Equation (6.11) can be rewritten as

$$\mathbf{C}(\omega)=\mathbf{A}(\omega)\mathbf{C_f}(\omega)\mathbf{A}(\omega)^H+\sigma^2\mathbf{I}(\omega), \qquad (6.12)$$

where $\mathbf{C_f}(\omega)=E\left[\mathbf{F}(\omega)\bullet\mathbf{F}(\omega)^H\right]$, denoting the covariance matrix of the source signal.

Applied with eigenvalue decomposition, the covariance matrix $\mathbf{C}(\omega)$ in Equation (6.12) is decomposed into two orthogonal subspaces, viz., signal subspace and noise subspace, as

$$\mathbf{C}(\omega)=\mathbf{U}(\omega)\mathbf{\Sigma}(\omega)\mathbf{U}(\omega)^H=\mathbf{U}_S(\omega)\mathbf{\Sigma}_S(\omega)\mathbf{U}_S(\omega)^H+\mathbf{U}_N(\omega)\mathbf{\Sigma}_N(\omega)\mathbf{U}_N(\omega)^H, \qquad (6.13)$$

where $\mathbf{U}(\omega)=[\mu_1(\omega),\mu_2(\omega),\cdots,\mu_M(\omega)]$ (the eigenvectors), and $\mathbf{\Sigma}(\omega)=\mathrm{diag}[\lambda_1,\lambda_2,...,\lambda_M]$ (the eigenvalues with $\lambda_1>\lambda_2>\cdots>\lambda_j>\lambda_{j+1}=\lambda_{j+2}=\cdots=\lambda_M=\sigma^2$). $\mathbf{U}_S(\omega)=[\mu_1(\omega),\mu_2(\omega),\cdots,\mu_j(\omega)]$ (*i.e.*, the signal subspace spanned by the eigenvectors corresponding to the *j* largest eigenvalues $\mathbf{\Sigma}_S(\omega)=\mathrm{diag}[\lambda_1,\lambda_2,...,\lambda_j]$); $\mathbf{U}_N(\omega)=[\mu_{j+1}(\omega),\mu_{j+1}(\omega),\cdots,\mu_M(\omega)]$ (namely, the noise subspace spanned by those eigenvectors corresponding to the remaining eigenvalues $\mathbf{\Sigma}_N(\omega)=\mathrm{diag}[\lambda_{j+1},\lambda_{j+2},...,\lambda_M]$).

Multiplying $\mathbf{U}_N(\omega)$ with $\mathbf{C}(\omega)$ in Equation (6.12) results in

$$\mathbf{C}(\omega)\mathbf{U}_N(\omega)=\mathbf{A}(\omega)\mathbf{C_f}(\omega)\mathbf{A}(\omega)^H\mathbf{U}_N(\omega)+\sigma^2\mathbf{U}_N(\omega). \qquad (6.14)$$

As $\mathbf{C}(\omega)\mathbf{U}_N(\omega)=\sigma^2\mathbf{U}_N(\omega)$ (according to Equation (6.13)), substituting $\sigma^2\mathbf{U}_N(\omega)$ into Equation (6.14) leads to

$$\mathbf{A}(\omega)\mathbf{C_f}(\omega)\mathbf{A}(\omega)^H\mathbf{U}_N(\omega)=\mathbf{0}. \tag{6.15}$$

Due to the full rank of $\mathbf{C_f}(\omega)$, Equation (6.15) can be simplified as

$$\mathbf{A}(\omega)^H\mathbf{U}_N(\omega)=[\mathbf{a}_1(\omega)^H\mathbf{U}_N(\omega),\cdots,\mathbf{a}_l(\omega)^H\mathbf{U}_N(\omega),\cdots,\mathbf{a}_L(\omega)^H\mathbf{U}_N(\omega)]=\mathbf{0}. \tag{6.16}$$

Equation (6.16) indicates that the steering vectors at a damage site are orthogonal with regard to the noise subspace, because $\mathbf{a}_l(\omega)^H\mathbf{U}_N(\omega)=\mathbf{0}$. With that, the F-MUSIC algorithm is defined in terms of the degree of orthogonality between the steering vector at each pixel and the noise subspace $\mathbf{U}_N(\omega)$, as

$$P_{F-MUSIC}(x,y,\omega)=\frac{1}{\left\|\mathbf{a}_{xy}(\omega)^H\mathbf{U}_N(\omega)\right\|^2}=\frac{1}{\mathbf{a}_{xy}(\omega)^H\mathbf{U}_N(\omega)\mathbf{U}_N(\omega)^H\mathbf{a}_{xy}(\omega)}, \tag{6.17}$$

where

$$\mathbf{a}_{xy}(\omega)=[\exp^{-i\omega d_{xy}^1/c_p(\omega)},\cdots,\exp^{-i\omega d_{xy}^m/c_p(\omega)},\cdots,\exp^{-i\omega d_{xy}^M/c_p(\omega)}]^T,$$

$$d_{xy}^m=\sqrt{(x-x_i)^2+(y-y_i)^2}+\sqrt{(x-x_j)^2+(y-y_j)^2}.$$

By varying (x,y) in Equation (6.17), the entire inspection region of the sample under inspection is scanned, and a spatial spectrum is obtained. In the presence of damage at a particular location, the steering vector $\mathbf{a}_{xy}(\omega)$ is orthogonal to the noise subspace $\mathbf{U}_N(\omega)$, as a result of which the denominator of Equation (6.17) tends to be zero, resulting in a steep peak in the spatial spectrum, to indicate the damage presence and its location. It is noteworthy that on the basis of the multiple-damage-scattered wavefield model, the eigenvalue decomposition in Equation (6.13) is calculated only once, and then the calculated $\mathbf{U}_N(\omega)$ is applicable to all pixels. It is such a feature of the F-MUSIC algorithm that avoids time-consuming pixel-based calculation – a demerit of the AM-MUSIC algorithm developed earlier [167], and remarkably lowers the computational costs.

On the other hand, the residual wave signals, $\mathbf{R}^{\text{residual}}(\omega)$, are distributed over a broad band ($\boldsymbol{\omega}$) rather than confined at the frequency of wave excitation. The broadband signals embrace rich information on damage or material degradation along the wave propagation path. With this in mind, the F-MUSIC algorithm is further refined by integrating the calculation conducted by Equation (6.17) over a broad frequency band ($\boldsymbol{\omega}$), as

$$P_{F-MUSIC}(x, y) = \frac{1}{\sum_{\omega \in \boldsymbol{\omega}} \left| \frac{1}{P_{F-MUSIC}(x, y, \omega)} \right|}. \tag{6.18}$$

Compared with conventional MUSIC algorithms manipulated in the time domain solely at the monochromatic excitation frequency, Equation (6.18) suggests that the F-MUSIC algorithm, based on the analysis of the multiple-damage-scattered wavefield over the frequency domain, fuses rich wave components over a broad frequency band, consequently enhancing imaging precision (to be demonstrated in what follows).

6.3 Numerical Validation

6.3.1 Modeling and Results

To verify the developed multiple-damage-scattered wavefield model and proposed F-MUSIC algorithm, numerical simulation is implemented first. A homogeneous, isotropic plate (density: ρ=2700 kg/m^3; Young modulus: E=71 GPa; Poisson's ratio:

ν=0.33; dimension: 300 mm × 300 mm × 2 mm) is modeled. Eight PZT wafers (labelled as P1, P2, …, P8) that are on the surface of the plate form a sparse sensor network for wave generation and acquisition (a total of $8(8-1)=56$ sensing paths), as illustrated schematically in **Figure 6.2**.

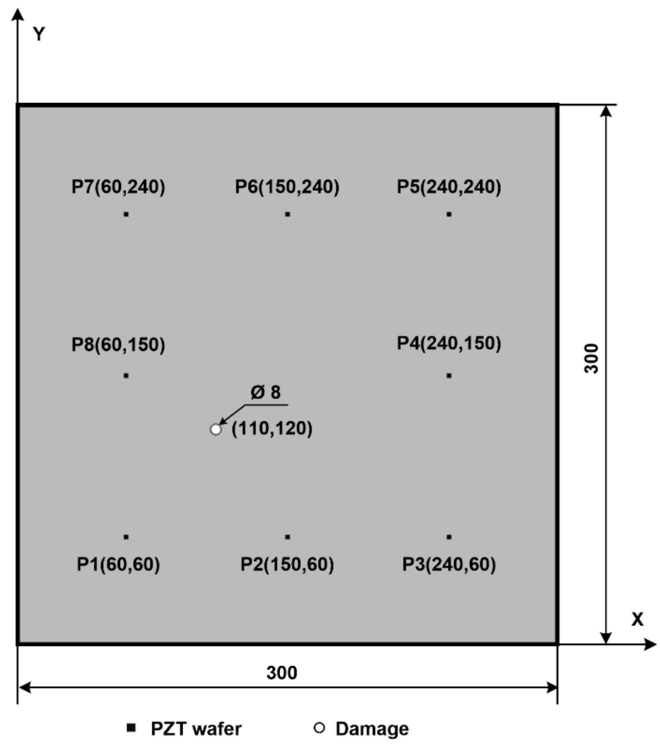

Figure 6.2 Schematic of a plate waveguide in simulation with a sparse sensor network (all dimensions in mm).

Two scenarios are comparatively modeled: one is the benchmark that is free of damage, and the other contains a through-hole of a diameter of 8 mm at (110 mm, 120 mm). Considering wave sensitivity and excitability, a 5-cycle Hanning windowed toneburst at 200 kHz, **Fig. 6.3**, is generated by each PZT wafer in turn to obtain S_0 wave mode, and in the meantime, the rest wafers serve as wave receivers to capture wave signals in a time window of 150 μs. In **Figure 6.3** the bandwidth of the excitation, centralized at 200 kHz, is observed to span from 100 to 300 kHz. The 56 sets of residual signals,

$r_m^{\text{residual}}(t), (m = 1, 2, \ldots, 56)$ in Equation (6.6), are obtained and shown in a waterfall view in **Figure 6.4**.

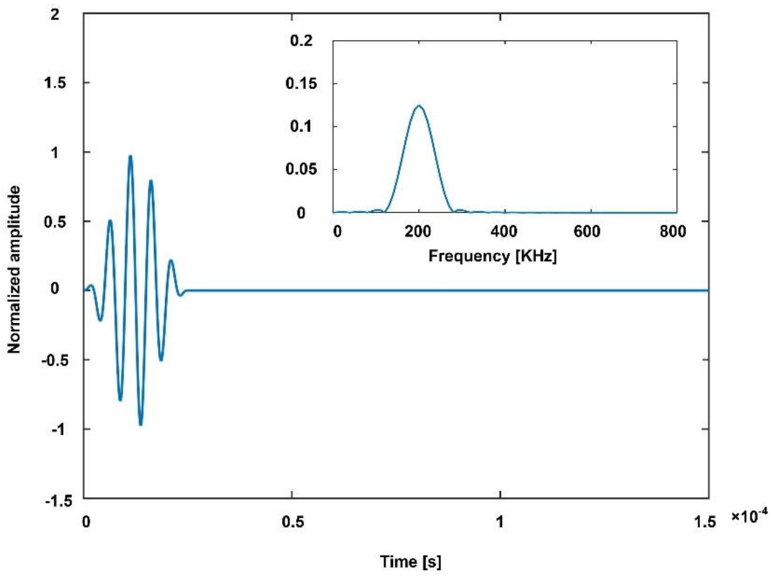

Figure 6.3 Excitation signal and frequency domain spectrum.

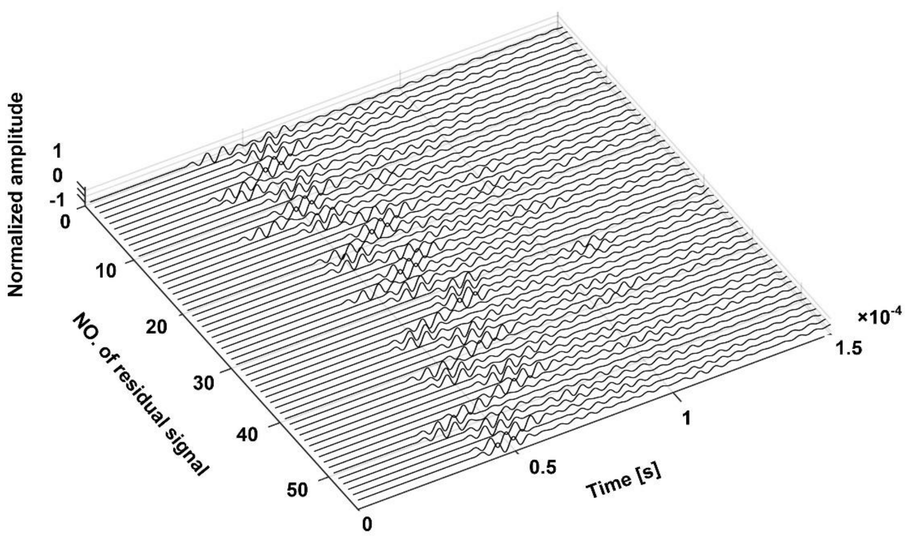

Figure 6.4 Waterfall view of 56 sets of residual signals.

Applying the F-MUSIC algorithm on all residual signals at the excitation frequency of 200 kHz using Equation (6.17), the spatial spectrum of the plate containing the through-hole is displayed in **Figure 6.5(a)**, in which, however, the damage can barely be visualized. Further, upon taking into account wave components scattered in the whole frequency band of excitation (100–300 kHz, as observed in **Figure 6.3** with Equation (6.18), the reconstructed image is shown in **Figure 6.5(b)**, which explicitly indicates the damage site and depicts the damage geometry with reduced artifacts, compared with **Figure 6.5(a)**.

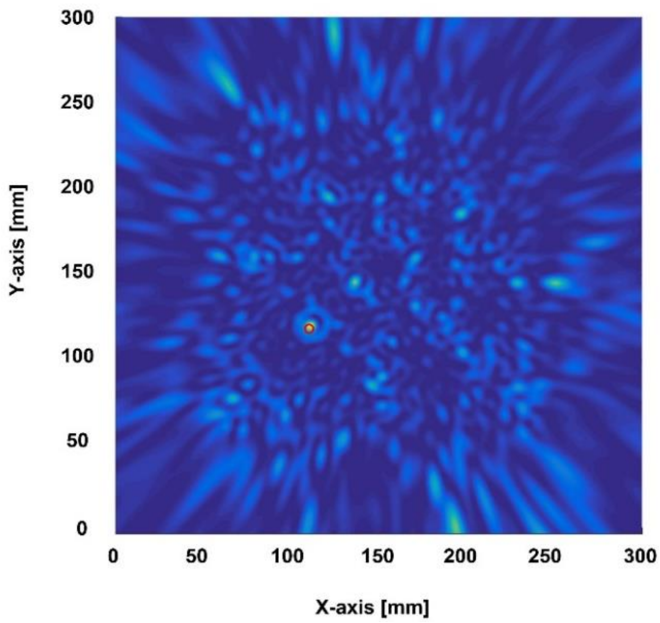

(a)

Figure 6.5 Spatial spectra obtained with F-MUSIC algorithm: (a) at the excitation frequency of 200 kHz; and (b) over the whole excitation band of 100–300 kHz (red ‘o’: actual damage).

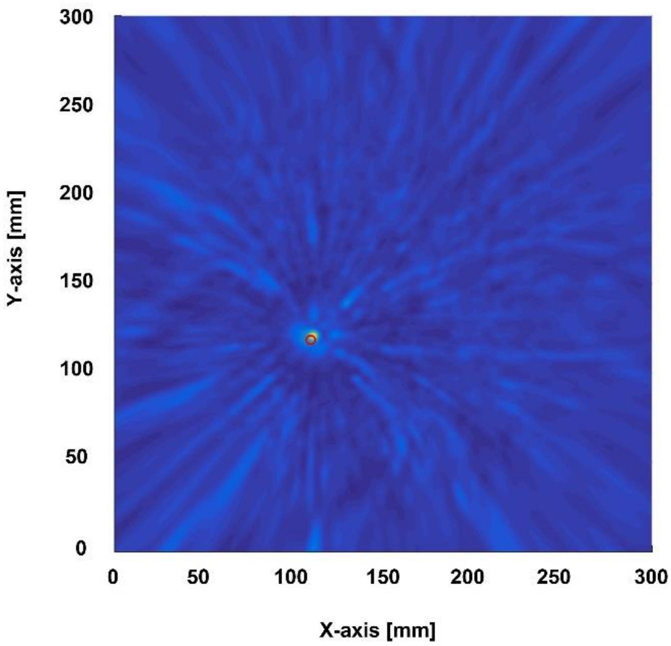

(b)

Figure 6.5 *Cont.*

6.3.2 Discussion

6.2.2.1 *Different Patterns of Sensor Distribution in Sparse Sensor Network*

To examine the performance of the F-MUSIC algorithm when the sensors are arranged in different patterns in the sparse sensor network, parametric studies respectively using six PZT wafers (namely, P1, P2, P4, P5, P6, P8) and using four PZT wafers (P2, P4, P6, P8), **Figure 6.2**, are conducted, and correspondingly imaged spatial spectra are in **Figures 6.6** and **6.7**, respectively. Comparison with the spectrum in **Figure 6.5(b)** constructed when eight PZT wafers are used, these results obtained using partial sensors of the sparse sensor network with different sensor distribution patterns still show a high degree of detectability, and this implies the high flexibility in sensor network configuration endowed by the F-MUSIC algorithm: not only in number of sensors, but in sensor distribution.

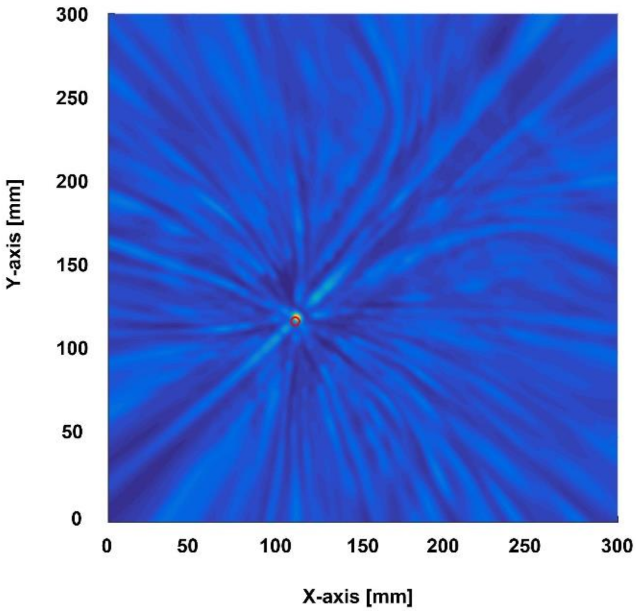

Figure 6.6 Spatial spectrum obtained with F-MUSIC algorithm using six PZT wafers (P1, P2, P4, P5, P6, P8) (red 'o': actual damage).

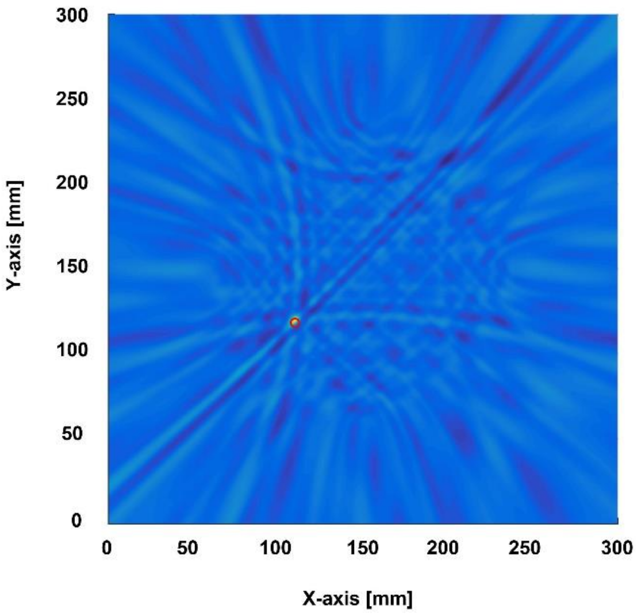

Figure 6.7 Spatial spectrum obtained with F-MUSIC algorithm using four PZT wafers (P2, P4, P6, P8) (red 'o': actual damage).

6.2.2.2 *Multiple Damage Sites*

The capability of identifying multiple damage sites in the inspection region using the F-MUSIC algorithm is studied. Two damage sites are included in the plate waveguide at (110 mm, 120 mm) and (190 mm, 180 mm), respectively. The spatial spectrum constructed using the F-MUSIC algorithm is shown in **Figure 6.8**, to observe a quantitative match between identified and actual damage sites.

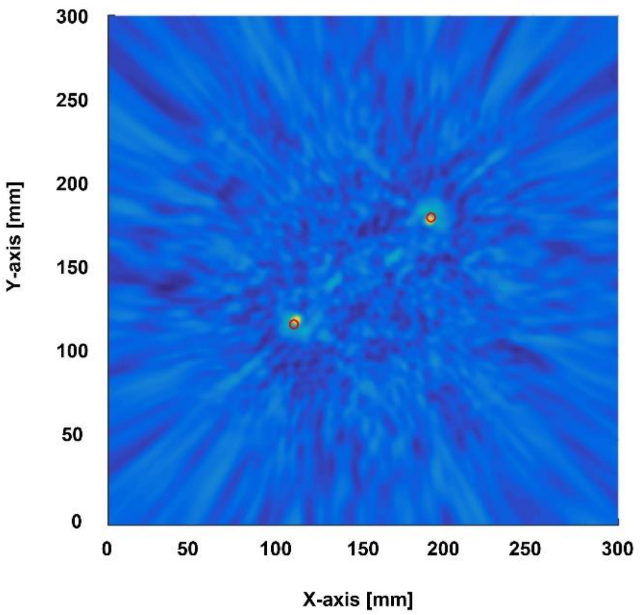

Figure 6.8 Spatial spectrum obtained with F-MUSIC algorithm for a plate waveguide containing multi-damage (red ‘o’: actual damage).

6.2.2.3 *Comparison with Conventional MUSIC Algorithm*

The conventional MUSIC algorithm [36, 152, 165] is recalled for comparison. To this end, seven PZT wafers are configured in a linear array as wave receivers, **Figure 6.9**, along with another PZT wafer at (150 mm, 240 mm) as wave transmitter. Similar to the above damage cases, two typical damage scenarios were illustrated. In the first case, a damage site D1 was located at (110 mm, 120 mm) as the single damage case. After then the multiple damage case is studied by adding another damage site D2 at the position (190 mm, 180 mm).

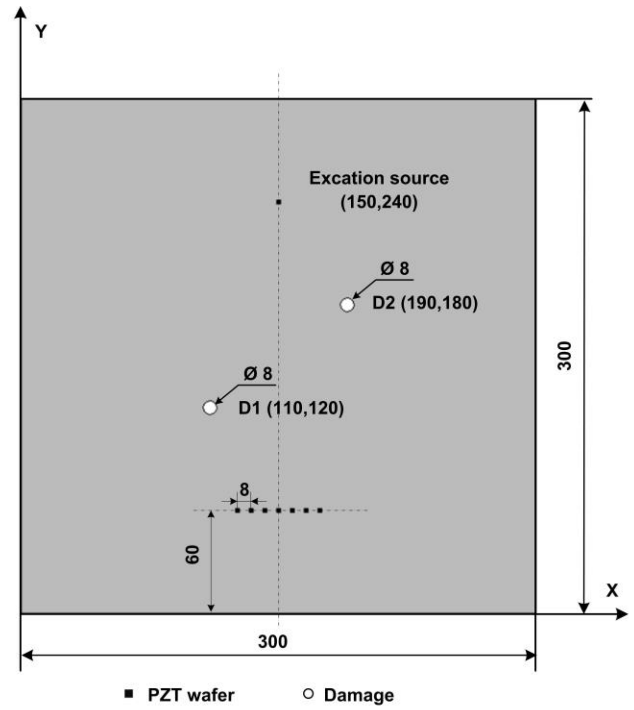

Figure 6.9 Schematic of a plate waveguide in simulation with a linear sensor array to implement conventional MUSIC algorithm (all dimensions in mm).

The images of two damage scenarios constructed using the conventional MUSIC algorithm are presented in **Figures 6.10(a) and (b)**, respectively, showing inferior accuracy in damage localization and sizing; In addition, elongation artifacts are spotted along with the scanning directions toward the damage sites, which further degrade the resolution and efficiency of identification.

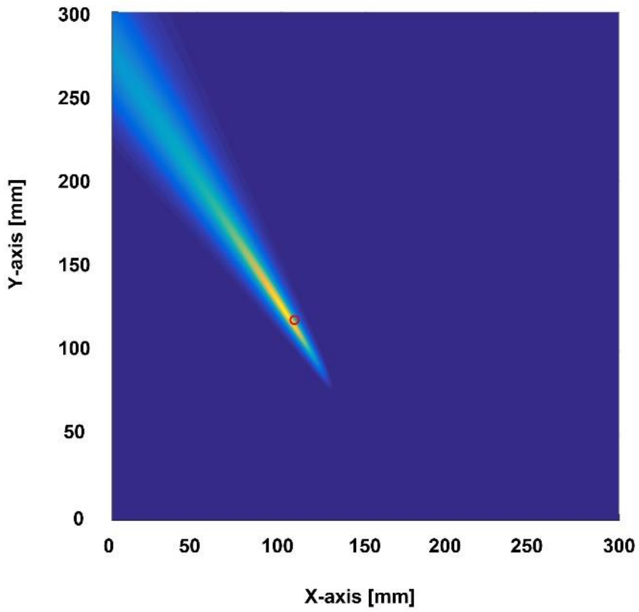

(a)

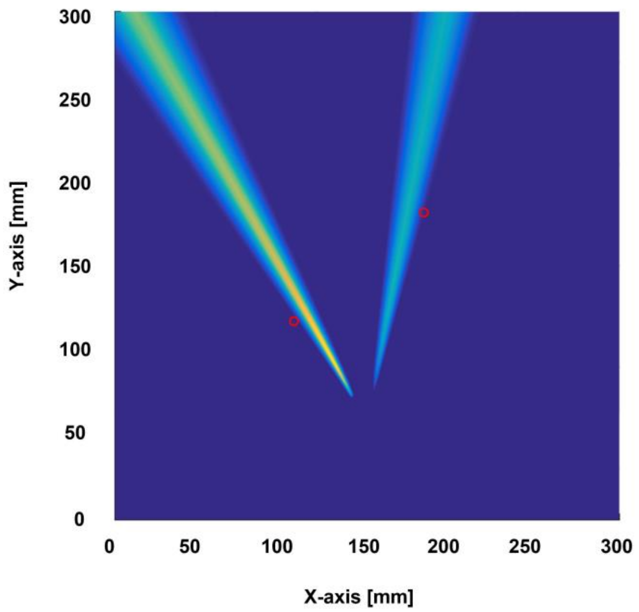

(b)

Figure 6.10 Spatial spectra constructed using conventional MUSIC algorithm for (a) single damage case and (b) multiple damage case (red 'o': actual damage).

6.4 Experimental Validation

Experimental validation is conducted. An aluminum plate (density: ρ=2700 kg/m^3; Young modulus: E=71 GPa; Poisson's ratio: ν=0.33; dimension: 1000 mm × 1000 mm × 2 mm) is prepared, on which a sparse sensor network, consisting of eight PZT wafers (labelled as PZT-1, PZT-2, …, PZT-8), is surface-adhered, with respective locations indicated in **Figure 6.11(a)**. The excitation wave is generated with a NI PXI-5412 arbitrary waveform generation unit, in the form of a five-cycle Hanning-windowed toneburst at the central frequency 200 kHz and amplified by a Ciprian US-TXP-3 linear power amplifier before being applied in turn to each PZT wafer. S_0 mode Lamb wave signals captured by remaining PZT wafers are recorded with an Agilent MSOX 3014A oscilloscope at the sampling rate of 60 MHz. The experimental setup is shown schematically in **Figure 6.11(b)**.

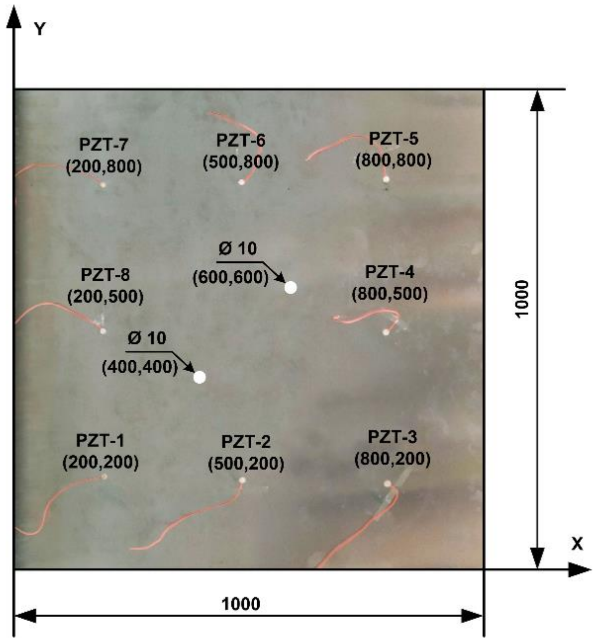

(a)

Figure 6.11 (a) An aluminum plate with a surface-adhered sparse sensor network consisting of eight PZT wafers in the experiment (all dimensions in mm); and (b) schematic of the experimental set-up.

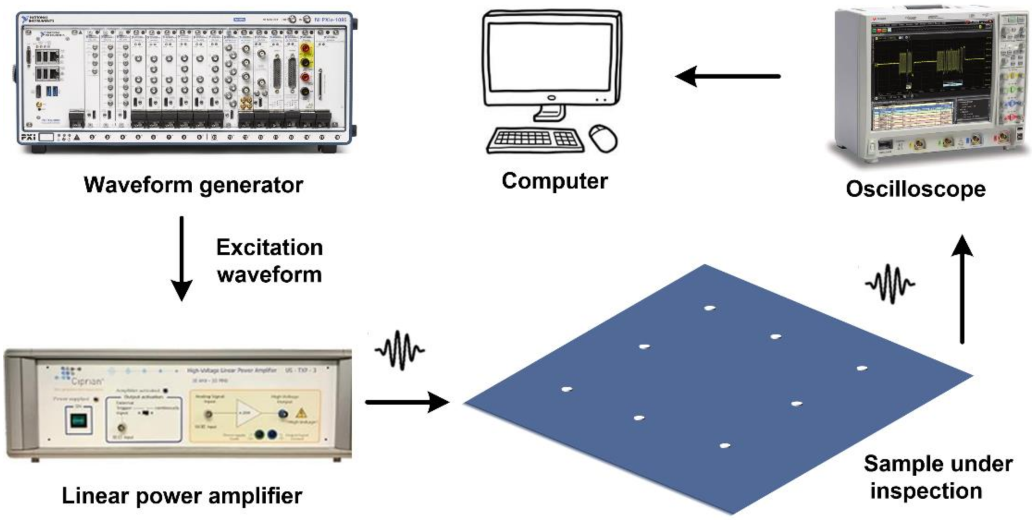

(b)

Figure 6.11 *Cont.*

In line with the simulation in Section 6.3, two damage scenarios are demonstrated in the experiment. In the first case, a through-hole of a diameter of 10 mm is drilled at the location (400 mm, 400 mm) as a single damage case; after then multiple damage case C-II is studied by adding another through-hole of the same diameter at the location (600 mm, 600 mm). The F-MUSIC algorithm is applied to two damage cases to obtain the spatial spectra, in **Figures. 6.12(a)** and **(b)**, in which all damage sites are clearly depicted with high precision and image resolution.

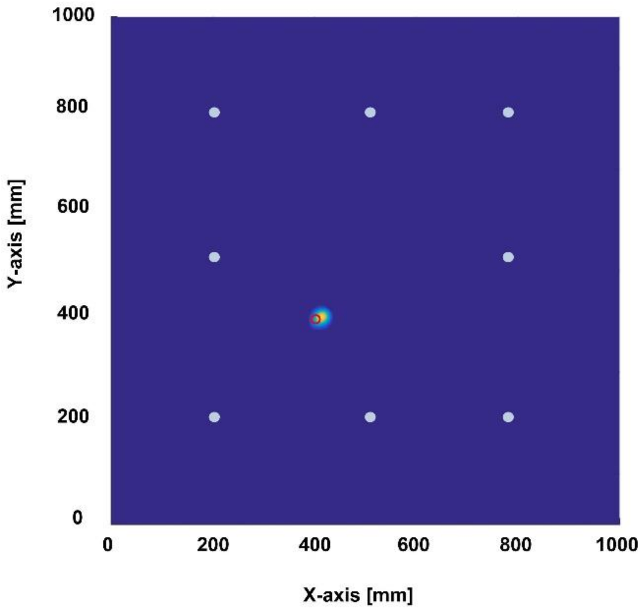

(a)

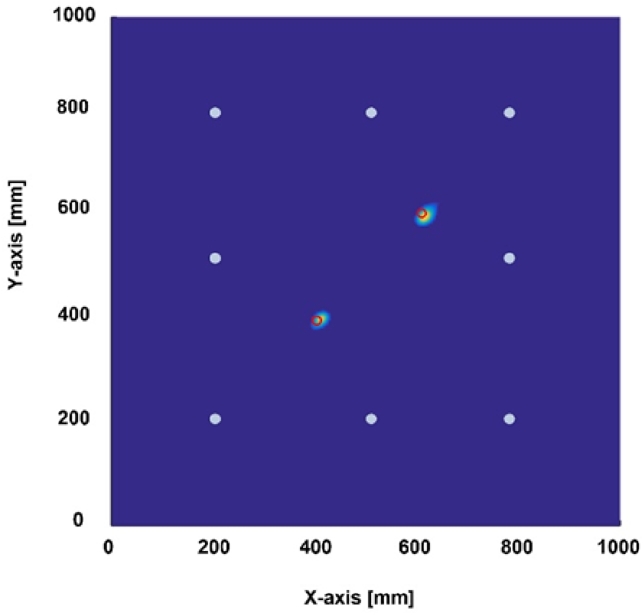

(b)

Figure 6.12 Spatial spectra for (a) the single damage case (b) the multiple damage case (red 'o': actual damage).

6.5 Summary

Aimed at exploiting the merits of the Am-MUSIC algorithm (particularly its flexibility in configuring a sparse sensor network) that is earlier developed based on conventional MUSIC algorithms but surmounting deficiency that the Am-MUSIC algorithm still remains, the F-MUSIC algorithm is developed, based on a multiple-damage-scattered wavefield model over the frequency domain. F-MUSIC avoids computationally expensive pixel-based calculation, and fuses rich information scattered in a broad band to enhance imaging precision. The algorithm is validated using simulation and experiment, and results articulate that the effectiveness of F-MUSIC is not restricted by the quantity of damage, and with it the imaging precision is not sacrificed as a result of the use of a sparse sensor network.

CHAPTER 7

An Application Paradigm: MUSIC-driven Structural Health Monitoring (SHM) Using All-printed Nanocomposite Sensor Array (APNSA)

7.1 Introduction

In spite of proven effectiveness in ultrasonic testing [168, 169], conventional ultrasonic arrays, with a bulky and unwieldy nature, are of a low degree of integrity with the inspected structure, which fails to implement *in-situ*, real-time SHM. To circumvent this deficiency, a new breed of nanocomposite-based ultrasonic sensor – APNSA – is fabricated, in lieu of the conventional transducer array, featuring not only full integration with the inspected structure but also high flexibility, ultralight weight, and broadband responsivity. Supported by such a novel sensor and used in conjunction with the aforementioned MUSIC algorithm, an *in-situ* health diagnosis framework can be implemented for damage identification and health status perception in a real-time manner.

7.2 APNSA: Fabrication and Responsivity

7.2.1 Fabrication of APNSA

The APNSA consists of a multitude of individual sensing elements which are inkjet printed by directly writing nanographene platelets (NGP)/PAA-based nanocomposite sensing ink on a Kapton film substrate. The sensing ink solvent is prepared by a standard solution mixing process, in which 0.2 g ethyl cellulose (EC) (viscosity 4 cP, 5 % in toluene/ethanol, Aldrich Chemistry) and 0.3 g polyvinyl pyrrolidone (PVP) (PVP K-30, Sigma-Aldrich®) are dissolved into 100 mL anhydrous n-methyl-2-pyrrolidone (NMP) (Aladdin®). By adding the Graphite powder (Aladdin®; 2.0 g) to the prepared solvent and processing a high-shear liquid phase exfoliation (LPE) with a high shear laboratory mixer (L5M, Silverson®), bulk natural graphite is exfoliated to few-layer graphene platelets, and the graphene dispersion is regulated to best fit the printing process. NGP dispersion is then centrifugated at 5,000 rpm for 20 min, and the top 80% of the supernatant is collected as NGP ink. Upon mixing the as-prepared NGP ink with PAA solution (12.8 wt% (80% NMP/20% aromatic hydrocarbon), Sigma-Aldrich; 1.6 g) and then magnetically stirring for 30 min, the NGP/PAA sensing ink is produced.

With the direct-writable NGP/PAA sensing ink, the printing process is deployed on a desktop inkjet printing platform which consists of a PiXDRO LP50 inkjet printer (OTB Solar-Roth & Rau) and a DMC-11610 cartridge (Dimatix-Fujifilm Inc.). Prior to the printing process, the NGP/PAA sensing ink is filtered to screen out large NGPs, and the Kapton film is pre-treated with O2 plasma to warrant good adhesion. After printing, the APNSA is annealed at 400 ^{o}C for 20 min, to ensure imidization of the PAA and remove the residual solvent and stabilizers. The parameters of APNSA including the size of the sensing element, the number of sensing elements, and the pitch of adjacent elements, can be customised to flexibly accommodate various applications. In this research, an APNSA with 8 sensing elements, **Figure 7.1(a)**, is applied, in which each element is printed on the substrate as a square with the size of 12 mm×12 mm, **Figure 7.1(b)**, and the pitch between the centres of two neighboring elements is 16 mm to avoid the spatial aliasing.

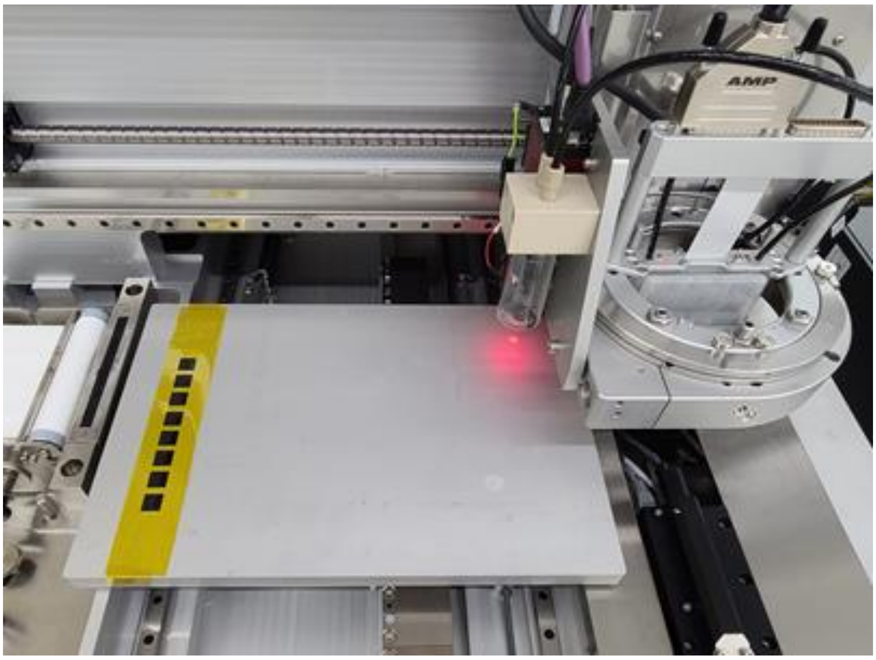

(a)

Figure 7.1 (a) APNSA on a Kapton film substrate, printed by a desktop inkjet printing platform; and (b) a typical sensing element of an APNSA.

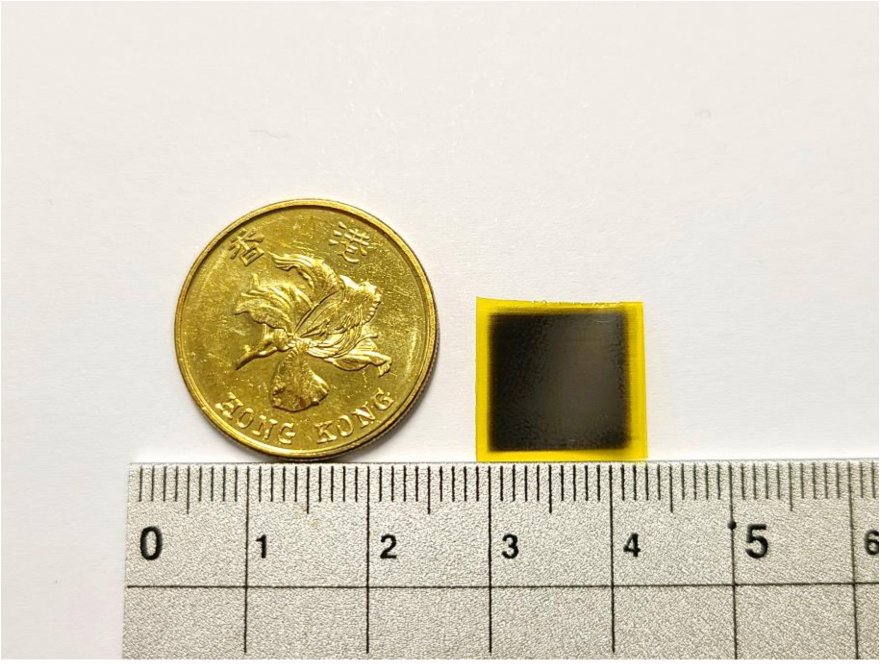

(b)

Figure 7.1 *Cont.*

7.2.2 Responsivity of APNSA

The performance of an embedded sensor is substantially subject to the responsivity of the individual sensing element to broadband acousto-ultrasonic waves. To this end, the responsive capability of the APNSA sensing element is examined using an ultrasonic measurement system, as shown in **Figure 7.2**. A 2 mm-thick glass fibre/epoxy-composite laminate plate (dimensions: 600 mm × 600 mm × 2 mm) is prepared, and a piezoelectric PZT wafer (Ø12 mm, 1 mm thick) is surface-bonded at the plate centre, functioning as an ultrasonic wave transmitter to emit waves into the laminate. A series of five-cycle Hanning-function-modulated sinusoidal tonebursts with the central frequency ranging from 50 to 500 kHz (with a stepping of 50 kHz) is generated with a waveform generator (NI® PXIe-1071), amplified with the power amplifier (Ciprian® US-TXP-3), and applied on the PZT wafer to emit acousto-ultrasonic waves into the laminate plate. Four APNSA sensing elements are adhered on the plate, and each is 150 mm apart from the transmitter for signal perception. Alongside each sensing element is a PZT wafer (Ø12 mm, 1 mm thick) which is used to capture wave signals for calibration and comparison with APNSA elements. Each APNSA sensing element is connected to a self-developed signal amplification and conditioning module via shielding cables. The module is powered by a GW INSTEK® GPC-3030D power supply, and consists of a resistance-adjustable R-V circuit that converts piezoresistive variations to electrical signals [170]. The signals captured by the APNSA sensing elements, as well as the counterpart signals acquired by PZT wafers, are simultaneously recorded using an Agilent® MSOX 3014A oscilloscope.

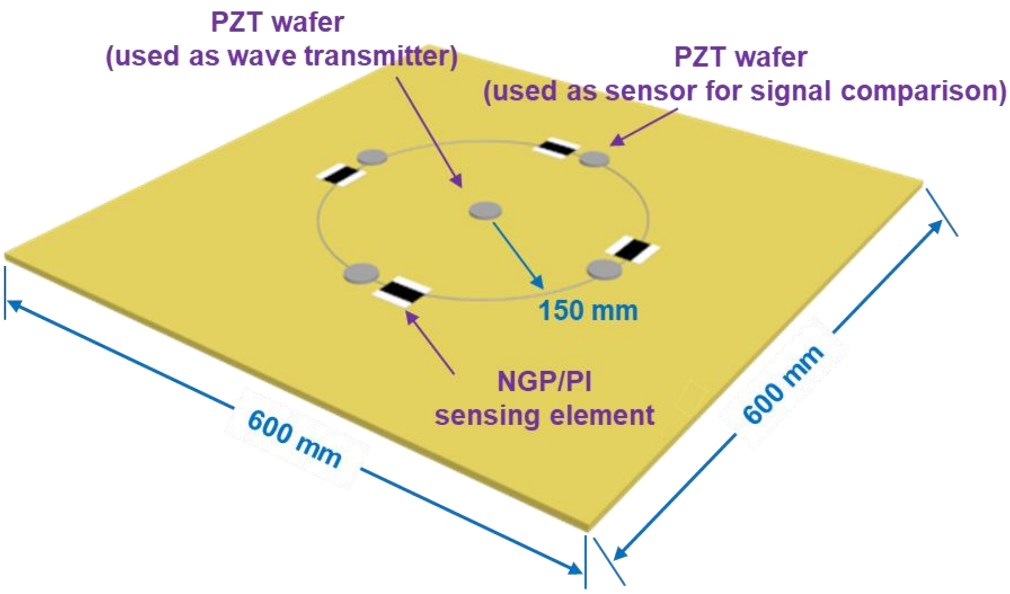

Figure 7.2 Experimental set-up for APNSA sensing element responsivity calibration (unit: mm).

At a representative frequency of 200 kHz, the wave signals captured by the APNSA sensing element and PZT wafer are displayed in **Figure 7.3**. It can be seen that the signal acquired the APNSA sensing element explicitly embraces wave components including S_0 (the zeroth-order symmetric plate wave mode guided by the laminate) and A_0 (the zeroth-order anti-symmetric plate wave mode guided by the laminate) modes, with all waveforms in good consistence with those acquired by the PZT wafers. In addition, the frequency analysis via fast Fourier transform is applied on exemplary signals in **Figure 7.4**, revealing that an energy peak at 200 kHz, in consistence with the excitation frequency. Moreover, the relationship between the magnitude of excitation and the response intensity of the sensor is investigated in **Figure 7.5**, in which the sensor response magnitude is subjected to degrees of excitation with a linear relationship, in good consistency with that observed in the PZT wafer. **Figure 7.6** further compares signal magnitudes captured by the APNSA sensing element and by PZT wafer in a sweep frequency from 50 to 500 kHz, arguing a consistent trend for the two types of sensors. Taking a step further, the propagation velocities of S_0 and A_0 wave modes at various excitation frequencies are shown in **Figure 7.7**, to observe a similar performance of two types of sensors in a wide frequency range as high as 500 kHz. All These findings have affirmed good sensitivity, stability, and precision of the APNSA sensing element in ultrasonic waves acquisition.

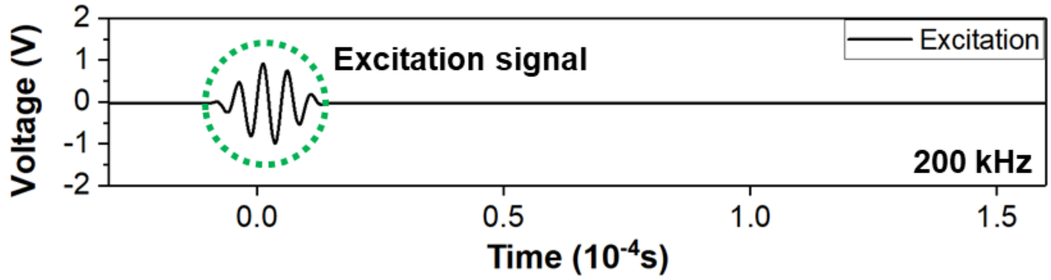

(a)

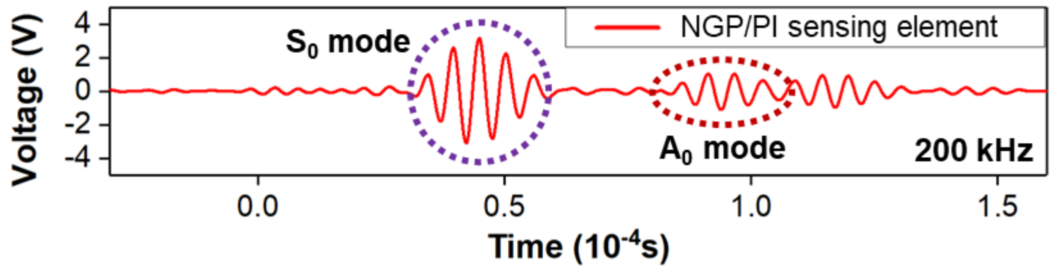

(b)

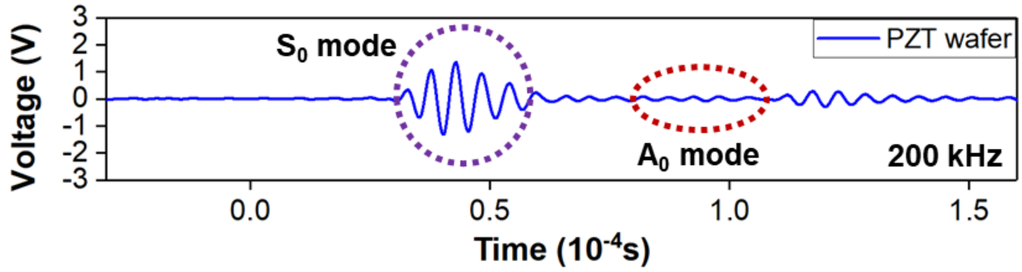

(c)

Figure 7.3 (a) Excitation signal at 200 kHz, as an example; wave signals acquired by (b) an APNSA sensing element, and (c) a PZT wafer; (d) comparison of wave energy envelopes.

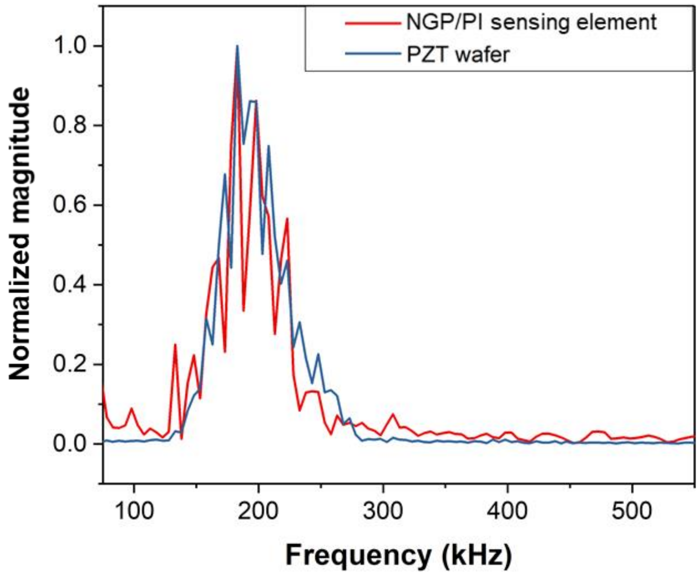

Figure 7.4 Spectra of wave signals captured by an APNSA sensing element and PZT wafer, at 200 kHz.

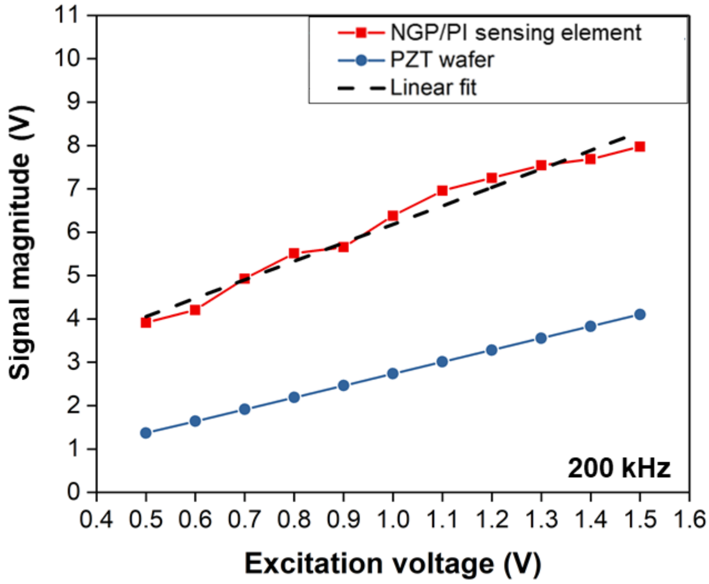

Figure 7.5 Peak-to-peak wave signal magnitude acquired by an APNSA sensing element and PZT wafer under different excitation voltages.

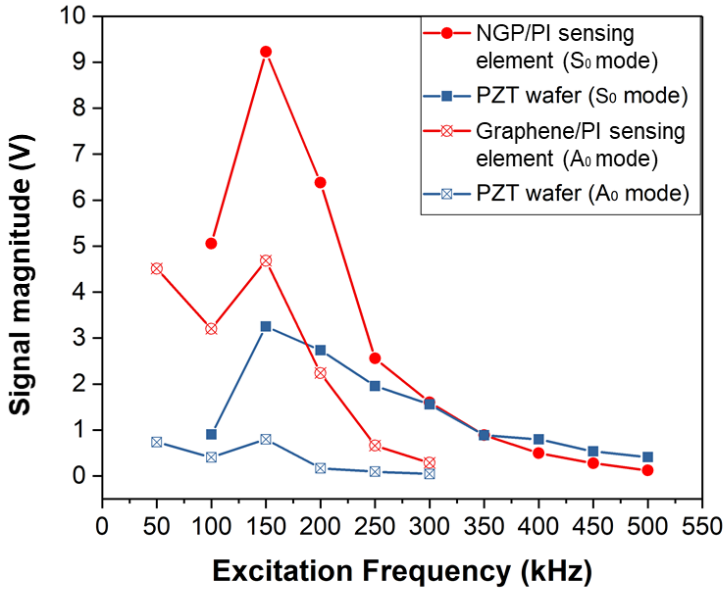

Figure 7.6 Peak-to-peak wave signal magnitudes acquired by APNSA sensing elements and PZT wafers (50-500 kHz).

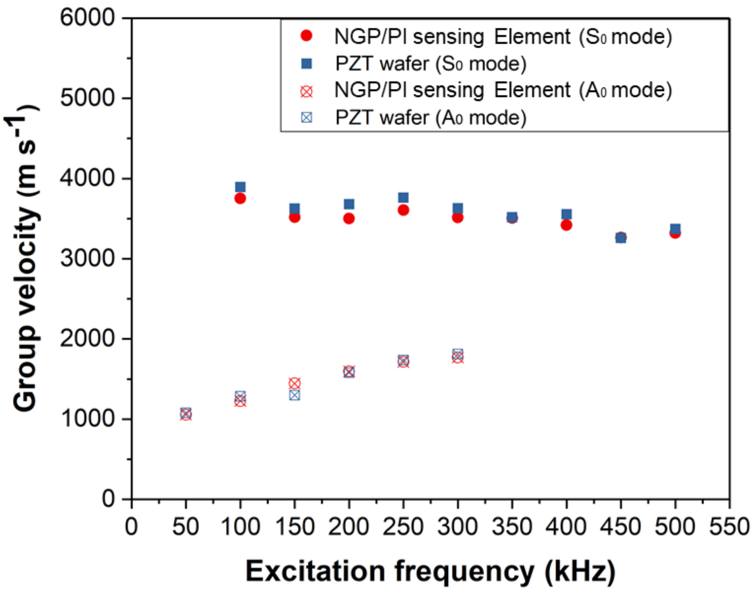

Figure 7.7 Comparison of group velocities acquired by APNSA sensing elements and PZT wafers (50-500 kHz).

7.3 MUSIC-driven Diagnostic Imaging of Composites Using APNSA

With proven responsivity and sensing precision in responding to broadband acousto-ultrasonic wave signals, the fabricated APNSA, in conjunction with the aforementioned MUSIC algorithm, is applied to implement *in-situ* damage identification, as an application paradigm. An APNSA consisting of eight graphene/PI sensing elements (labelled as S1, S2, …, S8) is surface mounted on the glass fibre/epoxy composite laminate plate, pictured in **Figure 7.8(a)**, along with an additional PZT wafer as a wave actuator, **Figure 7.8(b)**. A steel cylinder (Ø20 mm, 200 g weight) is additionally bonded on the plate at the location of (30 mm, 10 mm) as the mock-up anomaly. The experimental system and measurement procedures remain the same as those used in Section 7.2.2. A five-cycle Hanning-windowed sinusoidal toneburst at a central frequency of 100 kHz is applied to the PZT actuator, generating an excitation wave with a wavelength (λ) of 37.2 mm. The element pitch in APNSA has been pre-set as 16 mm during inkjet printing, which is smaller than the half wavelength (*i.e.*, 37.2/2=18.6 mm) of the generated wave.

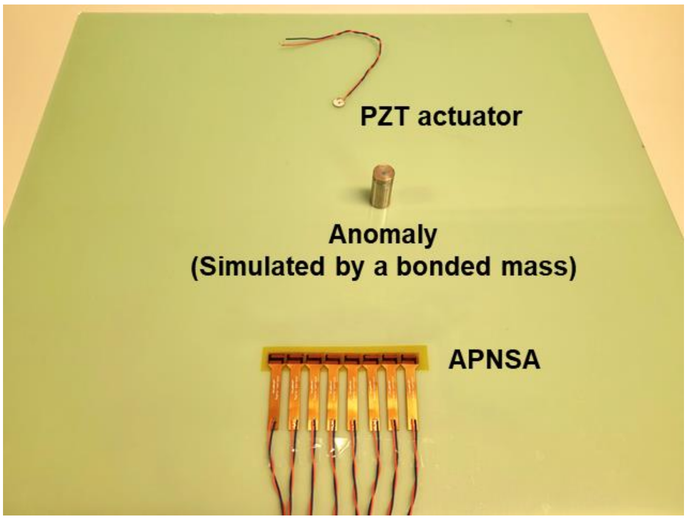

(a)

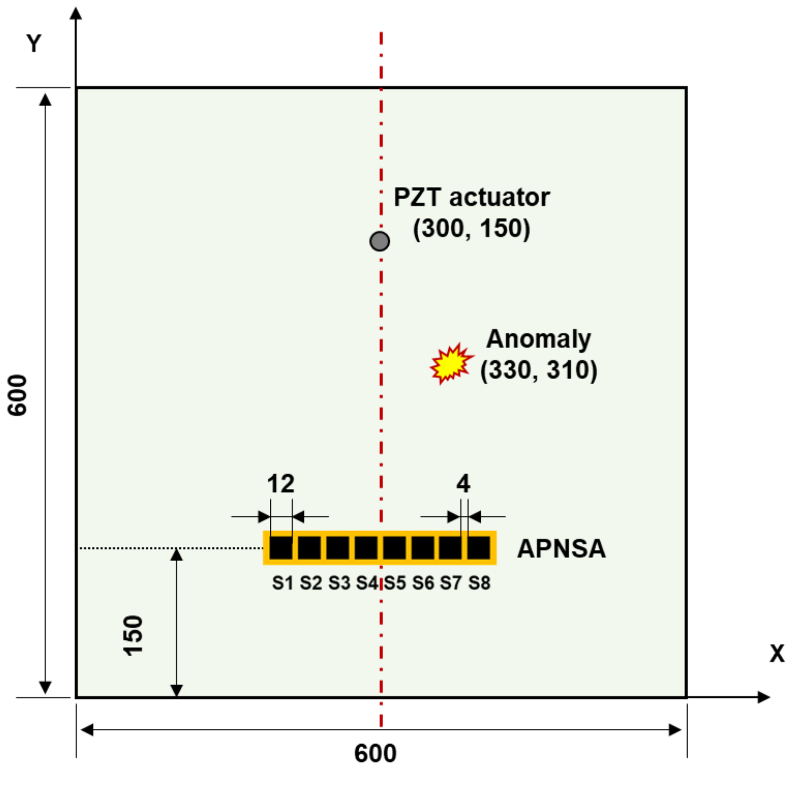

(b)

Figure 7.8 (a) Photograph and (b) schematic of the glass fibre/epoxy composite laminate plate with APNSA and a mock-up anomaly (unit: mm).

Two raw Lamb wave signals, captured by sensing element S1 of APNSA before and after introducing the mock-up anomaly, are shown in **Figure 7.9(a)**. Comparing two signals, an additional wave packet, **Figure 7.9(b)**, is prominent and classified as the anomaly-induced wave component, which is named the anomaly-scattered wave. Extending the above procedure to the whole elements of APNSA, all residual signals that contain all anomaly-scattered waves are extracted, **Figure 7.9(c)**, and written in a vector form, as

$$\boldsymbol{R}^{\text{residual}}(t) = [r_1^{\text{residual}}(t), ..., r_m^{\text{residual}}(t), ..., r_8^{\text{residual}}(t)]^{\mathrm{T}}, \tag{7.1}$$

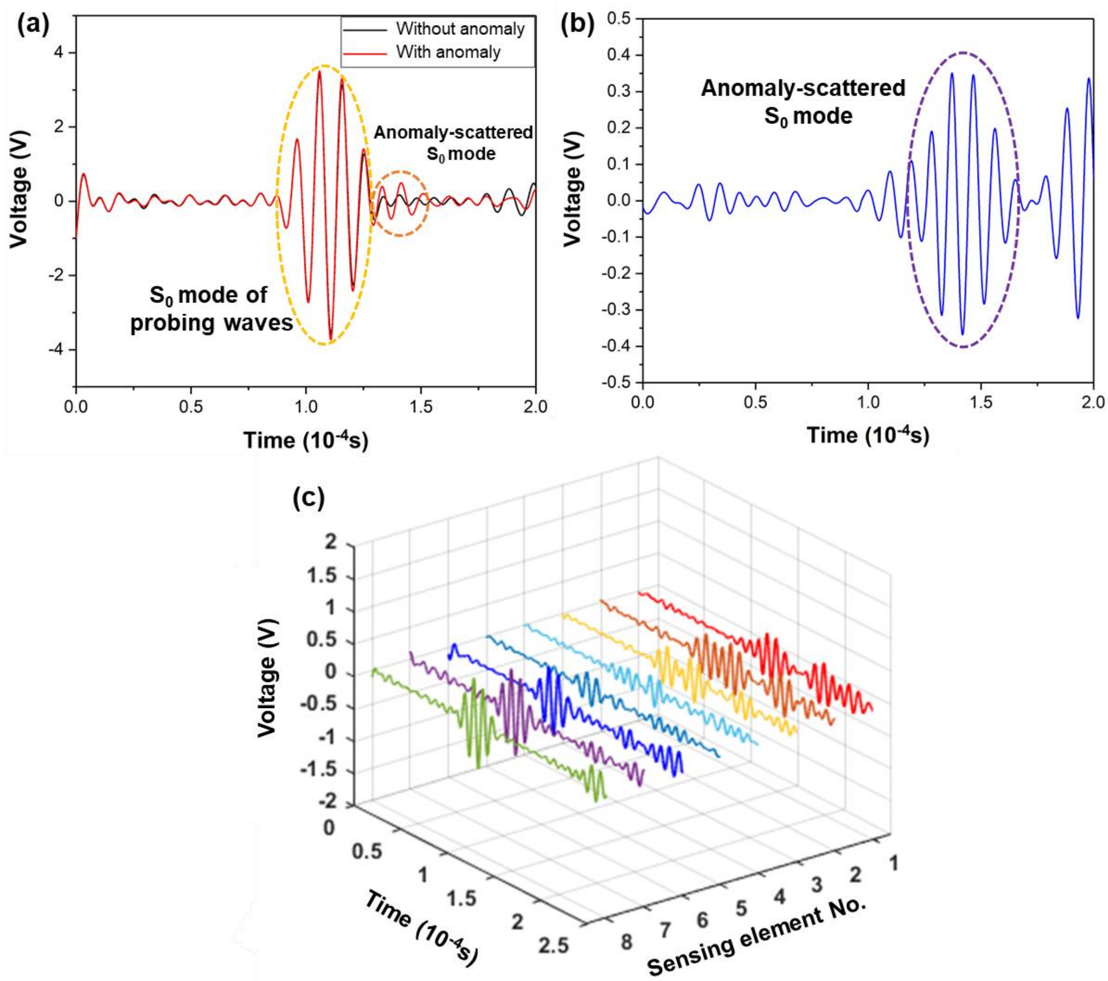

Figure 7.9 (a) Wave signals captured by S1 of APNSA, before and after the mock-up anomaly introduced; (b) anomaly-scattered S_0 mode waves in the residual signal captured by S1; and (c) residual signals captured by all the sensing elements of APNSA.

As indicated in **Figure 7.10**, the actuator is placed at position (x_0, y_0), and the m^{th} sensing element of APNSA is at (x_m, y_m). Assuming that a scanning position in the inspection region is at (x, y), the APNSA steering vector $\boldsymbol{A}(x, y)$ at this position can be defined according to the previous introduction in Section 5.3, as

$$\boldsymbol{A}(x,y) = [a_1(x,y),...,a_m(x,y),...,a_8(x,y)]^T, \tag{7.2}$$

where

$$a_m(x,y) = \sqrt{\frac{d_1}{d_m}}\exp^{i\omega_0\tau_m},$$

$$\tau_m = \frac{l\cos\theta}{c}(m-1) + (\frac{-l^2}{cd_1}\sin^2\theta)(m-1)^2 \quad (m = 1, 2, \ldots, 8),$$

$a_m(x,y)$ is the steering vector of sensing element Sm, and τ_m is the difference in propagation time between two signals captured by sensing element S1 and element Sm.

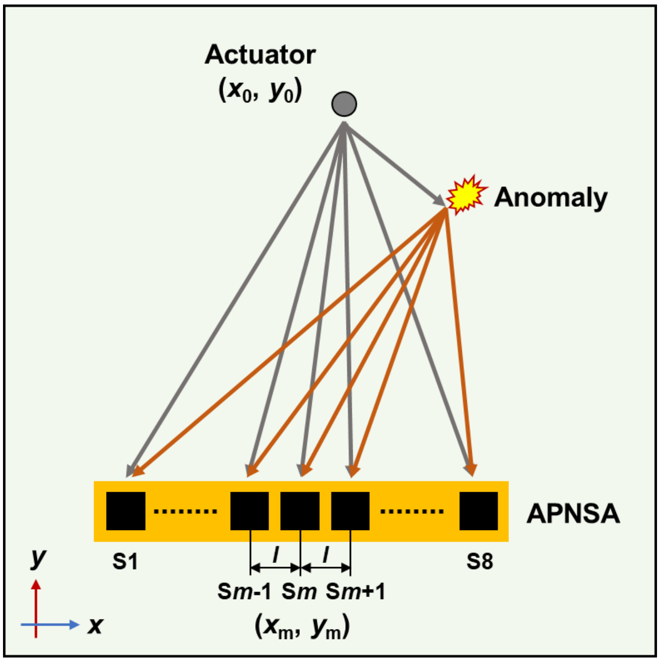

Figure 7.10 Use of MUSIC algorithm and APNSA for anomaly imaging.

Recalling the MUSIC algorithm, the pixel value of the spatial spectrum at (x, y), $P_{MUSIC}(x, y)$, is formulated as

$$P_{MUSIC}(x, y) = \frac{1}{\boldsymbol{A}^H(x, y)(\boldsymbol{U}_{\mathrm{N}}\boldsymbol{U}_{\mathrm{N}}^H)\boldsymbol{A}(x, y)}. \tag{7.3}$$

Superscript H represents the complex conjugate transpose. By varying the scanning position (x, y), the spatial spectrum of the entire inspection region of the laminate is obtained. When the scanning position matches the anomaly location, the steering vector $\boldsymbol{A}(x, y)$ is orthogonal with regard to the noise subspace $\boldsymbol{U}_{\mathrm{N}}$, and thus the denominator of Equation (7.3) approaches 0, resulting in a peak in the spatial spectrum that corresponds to the anomaly location.

The imaging result is illustrated in **Figure 7.11**, showing high agreement with the true location of the mock-up anomaly, demonstrating the great application potential towards *in-situ* SHM.

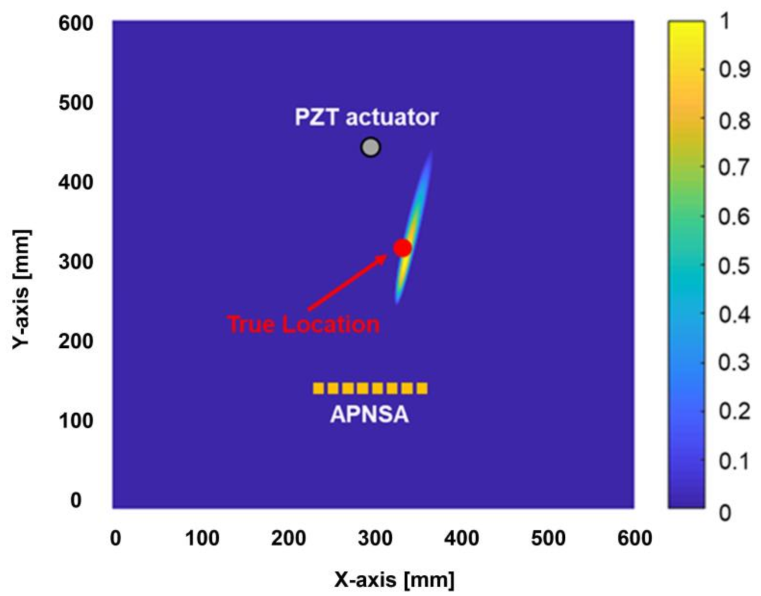

Figure 7.11 Anomaly image obtained via MUSIC algorithm and APNSA.

7.4 Summary

An *in sit*u health diagnosis framework, from sensing to the presentation of diagnostic results, is developed in this chapter, by integrating the APNSA sensor and MUSIC diagnosis algorithm. Compared with conventional ultrasonic arrays, APNSA can be fully integrated with the inspected structure, featuring high flexibility, ultralight weight, and broadband responsivity. Supported by such a novel sensor and used in conjunction with the aforementioned MUSIC algorithm, the continuous monitoring of damage can be implemented. The framework has been validated experimentally by intuitively and promptly characterizing structural damage in the composite laminates, and results highlight its alluring application prospects for damage detection and health status perception in a real-time and *in situ* manner.

CHAPTER 8

Conclusions and Recommendation for Future Work

8.1 Conclusions

Diagnostic imaging based on ultrasonic waves has attracted increasing attention from researchers in recent years because it can provide readily interpretable images, which are capable of intuitively indicating the structural damage details and even the overall 'health' state of the structure under inspection. However, prevailing diagnostic imaging still suffers some problematic issues:

(i) it is often a challenge for imaging techniques to delineate the lower surface of an embedded scatterer, let alone achieve a detailed depiction of its full features;

(ii) most approaches have a limited capability to detect the specimens featuring an irregular surface;

(iii) prevailing MUSIC-based methods are largely bound up with the use of a linear array, leaving blind zones and failing to access the full planar area of an inspected sample;

(iv) MUSIC algorithm in guided wave imaging, manipulated in the time domain, is applicable to monochromatic excitation only, ignoring signal features spanning a broad frequency band which also carry information of damage; and

(v) restricted by bulky transducers and computationally expensive imaging algorithms, it is a tough task to extend diagnostic imaging to real-time, continuous, *in-situ* SHM.

Aiming at circumventing the above-addressed deficiencies and bottlenecks that the prevailing diagnostic imaging are facing, in this PhD study, a novel diagnostic imaging framework has been proposed to revamp traditional imaging approaches.

First, the ETRM algorithm is investigated, whereby the lower surface of an embedded scatterer can be characterized cost-effectively, conducive to the precise delineation of the damage with full features. On the basis of the multipath scattering analysis and Fermat's principle of the acoustic wave propagation, the algorithm presented a virtual phased array to reconstruct the lower surface of the embedded damage. In conjunction with the damage upper surface constructed by the actual phased array, the full features damage can be precisely delineated. The ERTM is validated, in both simulation and experiment, by evaluating damage with different geometric profiles. Results show that compared with the conventional method, the EMTR method can efficiently characterize the lower surfaces of the flaw and precisely delineate the full profiles of scatterers, which provides a great alternative for characterizing the flaw with complex shapes.

To further detect the specimen featuring an irregular top surface, an RTM-based multistep ASA imaging framework is developed. Multistep ASA calculates forward propagation wavefields of sources and backward propagation wavefields of the received wave signals in the fluid-solid coupled system, with which the transient wavefields at the fluid-solid interface are used as incident waves to the solid. Upon applying a zero-lag cross-correlation imaging condition of RTM to the obtained forward and backward wavefields, the image of the specimen with an irregular surface can be reconstructed, to visualize damage, irrespective of the damage quantity. Experiments are performed to validate the proposed approach, in which multiple SDHs, at different locations in aluminum blocks with various irregular surfaces, are characterized quantitatively. The validation affirms that the multistep ASA shows an enhanced imaging resolution and contrast against conventional TFM.

An Am-MUSIC algorithm has been proposed to remove the limitation of uniform sensor array arrangement in the conventional method and improve damage imaging resolution. The Am-MUSIC method is developed by manipulating the signal representation matrix at each image pixel using the excitation signal series instead of the scattered signal series. Thanks to that, the Am-MUSIC algorithm does not necessarily entail the use of a linear phased array, and instead, it is compatible with a sparse sensor network in which individual transducers can be positioned arbitrarily. At each image pixel, the orthogonal attributes between the signal subspace and noise subspace inherent in the signal representation matrix are quantified, in terms of which Am-MUSIC yields a full spatial spectrum of the inspected sample, to visualize damage. The performance of the proposed algorithm has been verified by both simulations and experiments. Imaging results show that compared with the conventional method, the developed algorithm can successfully localize the damage and significantly improve the image quality. Moreover, the novel Am-MUSIC method uses a distributed array of inexpensive piezoelectric wafers, which is easier to be arranged on structures and more responsive to the demands of *in situ* SHM.

Aimed at exploiting the merits of the Am-MUSIC algorithm (particularly its flexibility in configuring a sensor network) but surmounting the deficiency that the algorithm remains, F-MUSIC is developed. Distinct from Am-MUSIC, F-MUSIC constructs the signal representation equation over the frequency domain, rather than at each pixel in the spatial domain, based on a multiple-damage-scattered wavefield model. F-MUSIC avoids computationally expensive pixel-based calculation, and fuses rich information scattered in a broad band to enhance imaging precision. The algorithm is validated using simulation and experiment, and results articulate that the effectiveness of F-MUSIC is not restricted by the quantity of damage, and with it, the imaging precision is not sacrificed as a result of the use of a sparse sensor network.

Lastly, an *in-situ* health diagnosis framework, from sensing to diagnosis, is developed by integrating the APNSA sensor and MUSIC diagnosis algorithm. Instead of conventional ultrasonic arrays, a new breed of nanocomposite-based ultrasonic sensor – APNSA – is developed, which can be fully integrated with the inspected structure, and also features high flexibility, ultralight weight, and broadband responsivity. Supported by such a novel sensor and used in conjunction with the MUSIC algorithm, the continuous monitoring of damage can be implemented. The effectiveness of the diagnosis framework is validated experimentally by characterizing structural damage in the composite laminates, and results highlight its alluring application prospects towards a real-time and *in-situ* SHM.

In short, the main achievements and original contributions of this PhD study can be summarized as follows:

- Development of the ETRM algorithm for characterizing both the upper surface and the lower surface of the embedded damage, achieving the precise delineation of the full profiles of damage.
- Development of the RTM-based multistep ASA imaging framework for ultrasonic testing of a specimen with an irregular top surface, demonstrating its capability of accurately depicting multiple damage.
- Development of the Am-MUSIC algorithm for damage detection in conjunction with the use of a sparse sensor network with an arbitrarily positioned transducer, capable of removing the limitation of uniform sensor array arrangement and improving damage imaging resolution.
- Development of the F-MUSIC algorithm based on a multiple-damage-scattered wavefield model, showing advantages in lowering the computational costs, fusing rich information scattered in a broad band and detecting multiple damage sites.
- Development of an *in-situ* health diagnosis framework by integrating the nanocomposite-based APNSA sensor and the MUSIC algorithm, extending ultrasonic imaging from offline testing to the *in-situ* SHM.

8.2 Recommendations for Future Work

With the promising outcomes reported here, there are still some problematic issues and challenges remaining for future exploration.

First, in this study, the effective use of waves reverberating between the top and bottom of the sample is key to accessing the whole profile of an embedded scatterer [83, 87]. However, for a thick sample, the highly reverberating waves quickly convert the acoustic energy of incident waves to diffuse waves, with a considerably reduced magnitude. One can lower the excitation frequency to minimize that effect, but it is at the cost of sacrificing the sensitivity of the incident waves to a small flaw [171]. To circumvent this problem, diffuse wavefields are increasingly explored, because diffuse waves are highly repeatable yet sensitive to perturbation in the sample (e.g., a flaw). As a representative modality of diffuse waves, coda waves, widely employed for seismogram analysis in geosciences, can be extended to damage identification [171, 172]. Nonetheless, due to multiple waves scattering and reverberation, coda wave signals are complex in appearance and it is thus a challenge to observe phenomenal changes in coda wave signals under their noisy and chaotic appearance. Therefore, future research will entail more efforts to cost-effectively extract damage features in coda wave signals.

Second, on basis of the linear wave scattering phenomena (*e.g.*, wave reflection, transmission), the present study casts major attention on the detection of linear macroscopic damage such as the side-drilled holes. However, engineering structures commonly initiates from microscopic damage, including fatigue crack under cyclic loading, early bolt loosening in the multi-type joints, and pitting damage [173-175]. Such types of damage present highly nonlinear features with their characteristic dimensions being remarkably smaller than the wavelength of a probing wave and may not be detected efficiently using conventional approaches based on linear wave scattering. Therefore, it is fairly challenging but of great significance to monitor and characterize the undersized damage in engineering structures when the damage is still in its embryo stage. The generation of nonlinear features is attributed to the material nonlinearity in the terms of the material's stress-strain relation or the contact acoustic nonlinearity (CAN) induced owing to the modulation of a 'breathing' crack nonlinear, and induce nonlinear phenomenal changes in captured signals, typically as the accumulative second harmonic waves. Therefore, in future work, a microscopic damage identification technique can be developed by combining results arising from this study and the nonlinearities of higher-order acousto-ultrasonic (AU) waves. Two major approaches would be recommended: mixed frequency responses (*e.g.,* nonlinear wave modulation spectroscopy) [176, 177] and shifts in resonance frequency (*e.g.,* nonlinear resonant ultrasound spectroscopy) [178, 179].

Third, the MUSIC-based methods developed in the study are primarily dependent on comparing the signals captured from the structure under inspection with baseline signals from a benchmark counterpart that is assumed to be free of damage. However, during this process, changes in measurement conditions may affect captured signals and should be considered. In practice, ambient temperature is the most common environmental change and has been investigated in pioneer studies [180-182], which indicates that in normal applications, change in ambient temperature is so small that there is no need to employ compensation, whereas when measurements operate in an environment of elevated temperature, the influence of temperature cannot be ignored. Thus appropriate temperature compensation will be applied in an environment with temperature variation, to improve the quality of wave signals and benefit damage identification.

Bibliography

[1] A.K.S. Jardine, D. Lin, D. Banjevic, A review on machinery diagnostics and prognostics implementing condition-based maintenance, Mechanical Systems and Signal Processing, 20 (2006) 1483-1510.

[2] J. García-Martín, J. Gómez-Gil, E. Vázquez-Sánchez, Non-destructive techniques based on eddy current testing, Sensors, 11 (2011) 2525-2565.

[3] J. Krautkrämer, H. Krautkrämer, Ultrasonic testing of materials, Springer Science & Business Media, 2013.

[4] G. Gaussorgues, S. Chomet, Infrared thermography, Springer Science & Business Media, 1993.

[5] J. Blitz, Electrical and magnetic methods of non-destructive testing, Springer Science & Business Media, 2012.

[6] S. Rothberg, J.R. Baker, N.A. Halliwell, Laser vibrometry: pseudo-vibrations, (1989).

[7] B.L. Luk, A.H.S. Chan, Human Factors and Ergonomics in Dye Penetrant and Magnetic Particles Nondestructive Inspection Methods, Engineering Letters, 15 (2007).

[8] Y.Y. Hung, H.P. Ho, Shearography: An optical measurement technique and applications, Materials science and engineering: R: Reports, 49 (2005) 61-87.

[9] J.A. Rowlands, The physics of computed radiography, Physics in Medicine & Biology, 47 (2002) R123.

[10] R. Drai, F. Sellidj, M. Khelil, A. Benchaala, Elaboration of some signal processing algorithms in ultrasonic techniques: application to materials NDT, Ultrasonics, 38 (2000) 503-507.

[11] C.-H. Chen, Ultrasonic and advanced methods for nondestructive testing and

material characterization, World Scientific, 2007.
[12] J.L.J.M.E. Rose, Success and challenges for ultrasonic testing in NDT and SHM, Materials Evaluation, 68 (2010) 494-500.
[13] C.L. Morgan, W.S. Trought, G. Sheldon, T.K. Barton, B-scan and real-time ultrasound in the antepartum diagnosis of conjoined twins and pericardial effusion, AJR. American journal of roentgenology, 130 (1978) 578-580.
[14] M. Fatemi, A.C. Kak, Ultrasonic B-scan imaging: Theory of image formation and a technique for restoration, Ultrasonic Imaging, 2 (1980) 1-47.
[15] P. Webb, C. Wykes, High-resolution beam forming for ultrasonic arrays, IEEE Transactions on Robotics and Automation, 12 (1996) 138-146.
[16] C. Fan, M. Caleap, M. Pan, B.W. Drinkwater, A comparison between ultrasonic array beamforming and super resolution imaging algorithms for non-destructive evaluation, Ultrasonics, 54 (2014) 1842-1850.
[17] R. Růžek, R. Lohonka, J. Jironč, Ultrasonic C-Scan and shearography NDI techniques evaluation of impact defects identification, NDT & E International, 39 (2006) 132-142.
[18] C. Holmes, B. Drinkwater, P. Wilcox, The post-processing of ultrasonic array data using the total focusing method, Insight-Non-Destructive Testing and Condition Monitoring, 46 (2004) 677-680.
[19] C. Holmes, B.W. Drinkwater, P.D. Wilcox, Post-processing of the full matrix of ultrasonic transmit–receive array data for non-destructive evaluation, NDT & E International, 38 (2005) 701-711.
[20] S. Müller, E. Niederleithinger, T. Bohlen, Reverse time migration: A seismic imaging technique applied to synthetic ultrasonic data, International Journal of Geophysics, 2012 (2012).
[21] M. Hu, S.-E. Chen, D. Pan, Reverse time migration based ultrasonic wave detection for concrete structures, Design, Construction, and Maintenance of Bridges, 2014, pp. 53-60.

[22] H. Gao, Y. Shi, J.L. Rose, Guided wave tomography on an aircraft wing with leave in place sensors, AIP Conference Proceedings, American Institute of Physics, 2005, pp. 1788-1794.

[23] J.E. Michaels, Detection, localization and characterization of damage in plates with an in situ array of spatially distributed ultrasonic sensors, Smart Materials and Structures, 17 (2008) 035035.

[24] L. Qiu, S. Yuan, X. Zhang, Y. Wang, A time reversal focusing based impact imaging method and its evaluation on complex composite structures, Smart Materials and Structures, 20 (2011) 105014.

[25] C. Zhou, Z. Su, L. Cheng, Quantitative evaluation of orientation-specific damage using elastic waves and probability-based diagnostic imaging, Mechanical Systems and Signal Processing, 25 (2011) 2135-2156.

[26] S.-J. Wei, X.-L. Zhang, J. Shi, G. Xiang, Sparse reconstruction for SAR imaging based on compressed sensing, Progress In Electromagnetics Research, 109 (2010) 63-81.

[27] J.S. Hall, J.E. Michaels, Minimum variance ultrasonic imaging applied to an in situ sparse guided wave array, IEEE Transactions on Ultrasonics, Ferroelectrics, and Frequency Control, 57 (2010) 2311-2323.

[28] M. Viberg, B. Ottersten, Sensor array processing based on subspace fitting, IEEE Transactions on signal processing, 39 (1991) 1110-1121.

[29] A.J. Hartemink, D.K. Gifford, T.S. Jaakkola, R.A. Young, Maximum-likelihood estimation of optimal scaling factors for expression array normalization, Microarrays: Optical technologies and informatics, International Society for Optics and Photonics, 2001, pp. 132-140.

[30] R. Schmidt, Multiple emitter location and signal parameter estimation, IEEE transactions on antennas and propagation, 34 (1986) 276-280.

[31] F.-G. Yan, Y. Shen, M. Jin, Fast DOA estimation based on a split subspace decomposition on the array covariance matrix, Signal Processing, 115 (2015) 1-8.

[32] D. Kundu, Modified MUSIC algorithm for estimating DOA of signals, Signal Processing, 48 (1996) 85-90.

[33] S. Sundararaman, D.E. Adams, E.J. Rigas, Structural damage identification in homogeneous and heterogeneous structures using beamforming, Structural Health Monitoring, 4 (2005) 171-190.

[34] J. Yang, J. He, X. Guan, D. Wang, H. Chen, W. Zhang, Y. Liu, A probabilistic crack size quantification method using in-situ Lamb wave test and Bayesian updating, Mechanical Systems and Signal Processing, 78 (2016) 118-133.

[35] T. Gao, X. Liu, J. Zhu, B. Zhao, X. Qing, Multi-frequency localized wave energy for delamination identification using laser ultrasonic guided wave, Ultrasonics, 116 (2021) 106486.

[36] Y. Zhong, S. Yuan, L. Qiu, Multiple damage detection on aircraft composite structures using near-field MUSIC algorithm, Sensors and Actuators A: Physical, 214 (2014) 234-244.

[37] S. Yuan, Q. Bao, L. Qiu, Y. Zhong, A single frequency component-based re-estimated MUSIC algorithm for impact localization on complex composite structures, Smart Materials and Structures, 24 (2015) 105021.

[38] Q. Bao, S. Yuan, F. Guo, L. Qiu, Transmitter beamforming and weighted image fusion–based multiple signal classification algorithm for corrosion monitoring, Structural Health Monitoring, 18 (2019) 621-634.

[39] W. Nsengiyumva, S. Zhong, J. Lin, Q. Zhang, J. Zhong, Y. Huang, Advances, limitations and prospects of nondestructive testing and evaluation of thick composites and sandwich structures: A state-of-the-art review, Composite Structures, 256 (2021) 112951.

[40] J.D.N. Cheeke, Fundamentals and applications of ultrasonic waves, CRC press, 2010.

[41] S.W. Wenzel, R.M. White, Analytic comparison of the sensitivities of bulk - wave, surface - wave, and flexural plate - wave ultrasonic gravimetric sensors, Applied

Physics Letters, 54 (1989) 1976-1978.

[42] J.L. Rose, Ultrasonic waves in solid media, Acoustical Society of America, 2000.

[43] L.W. Schmerr, Fundamentals of ultrasonic nondestructive evaluation, Springer, 2016.

[44] R.N. Thurston, A.D. Pierce, E.P. Papadakis, Reference for Modern Instrumentation, Techniques, and Technology: Ultrasonic Instruments and Devices I: Ultrasonic Instruments and Devices I, Academic Press, 1998.

[45] Olympus, Conventional Transducer Construction, https://www.olympus-ims.com/en/ndt-tutorials/transducers/construction/.

[46] L.W. Schmerr Jr, Fundamentals of ultrasonic phased arrays, Springer, 2014.

[47] A. McNab, M.J. Campbell, Ultrasonic phased arrays for nondestructive testing, NDT international, 20 (1987) 333-337.

[48] D.R. Daum, K. Hynynen, A 256-element ultrasonic phased array system for the treatment of large volumes of deep seated tissue, IEEE transactions on ultrasonics, ferroelectrics, and frequency control, 46 (1999) 1254-1268.

[49] J. Poguet, J. Marguet, F. Pichonnat, L. Chupin, Phased array technology: Concepts, probes and applications, Journal of Nondestructive Testing & Ultrasonics(Germany), 7 (2002) 1-6.

[50] U. NDT, Phased Array probes, https://www.united-ndt.com/en/content/39-phased-array-probes.

[51] Olympus, Inside a Phased Array Transducer, https://www.olympus-ims.com/en/ndt-tutorials/transducers/inside/.

[52] M. Spies, H. Rieder, A. Dillhöfer, V. Schmitz, W. Müller, Synthetic aperture focusing and time-of-flight diffraction ultrasonic imaging—past and present, Journal of Nondestructive Evaluation, 31 (2012) 310-323.

[53] Z. Han, H. Peng, P. Lu, 3D ultrasound imaging in frequency domain with 1D array transducer, Ultrasonics, 76 (2017) 28-34.

[54] M. Krause, F. Mielentz, B. Milman, W. Müller, V. Schmitz, H. Wiggenhauser,

Ultrasonic imaging of concrete members using an array system, NDT & E International, 34 (2001) 403-408.

[55] G.R. Lockwood, J.R. Talman, S.S. Brunke, Real-time 3-D ultrasound imaging using sparse synthetic aperture beamforming, IEEE transactions on ultrasonics, ferroelectrics, and frequency control, 45 (1998) 980-988.

[56] C. Fan, L. Yang, Y. Zhao, Ultrasonic multi-frequency time-reversal-based imaging of extended targets, NDT & E International, 113 (2020) 102276.

[57] M. Schickert, M. Krause, W. Müller, Ultrasonic imaging of concrete elements using reconstruction by synthetic aperture focusing technique, Journal of materials in civil engineering, 15 (2003) 235-246.

[58] J.C. Somer, Electronic sector scanning for ultrasonic diagnosis, Ultrasonics, 6 (1968) 153-159.

[59] A. Fahr, Ultrasonic C-scan inspection of composite materials, (1992).

[60] Olympus, A-Scan Data, https://www.olympus-ims.com/en/ndt-tutorials/instrumententation/ascan/.

[61] Olympus, Single Value B-Scan, https://www.olympus-ims.com/en/ndt-tutorials/instrumententation/bscan/.

[62] Olympus, C-Scan Mapping, https://www.olympus-ims.com/en/ndt-tutorials/instrumententation/cscan/.

[63] Olympus, Phased Array Linear Scans, https://www.olympus-ims.com/en/ndt-tutorials/instrumententation/sscan/.

[64] Olympus, Phased Array C-Scan, https://www.olympus-ims.com/en/ndt-tutorials/instrumententation/pa-cscan/.

[65] L. Demi, Practical guide to ultrasound beam forming: Beam pattern and image reconstruction analysis, Applied Sciences, 8 (2018) 1544.

[66] A. Sawaguchi, K. Toda, Linear electronic scanning type of ultrasonic imaging system using comb electrode arrays with Fresnel zone pattern, Sensors and Actuators A: Physical, 34 (1992) 37-42.

[67] X. Jiang, Q. Han, H. Zheng, G. Tian, P. Wang, Study on Sectorial Scan Angle Range for Phased Array Ultrasonic Testing in standard setting.

[68] K. Hynynen, R. Roemer, D. Anhalt, C. Johnson, Z.X. Xu, W. Swindell, T. Cetas, A scanned, focused, multiple transducer ultrasonic system for localized hyperthermia treatments, International Journal of Hyperthermia, 26 (2010) 1-11.

[69] J. Liang, Z. Wang, Y. Shi, Ultrasonic inspection of thick parts with phased array dynamic focusing, pp. 986-992.

[70] J. Ritter, Universal phased array UT probe for nondestructive examinations using composite crystal technology, Journal of Nondestructive Testing, 1 (1996).

[71] M. Karaman, P.-C. Li, M. O'Donnell, Synthetic aperture imaging for small scale systems, IEEE transactions on ultrasonics, ferroelectrics, and frequency control, 42 (1995) 429-442.

[72] O. Martinez, M. Parrilla, M.A.G. Izquierdo, L.G. Ullate, Application of digital signal processing techniques to synthetic aperture focusing technique images, Sensors and Actuators A: Physical, 76 (1999) 448-456.

[73] A. Chahbaz, R. Sicard, Comparitive evaluation between ultrasonic phased array and synthetic aperture focusing techniques, AIP Conference Proceedings, American Institute of Physics, 2003, pp. 769-776.

[74] T. Stepinski, An implementation of synthetic aperture focusing technique in frequency domain, ieee transactions on ultrasonics, ferroelectrics, and frequency control, 54 (2007) 1399-1408.

[75] M.H. Skjelvareid, Y. Birkelund, Y. Larsen, Internal pipeline inspection using virtual source synthetic aperture ultrasound imaging, Ndt & E International, 54 (2013) 151-158.

[76] P.D. Wilcox, C. Holmes, B.W. Drinkwater, Enhanced defect detection and characterisation by signal processing of ultrasonic array data, Proc. 9th ECNDT, (2006).

[77] P.D. Wilcox, C. Holmes, B.W. Drinkwater, Advanced reflector characterization

with ultrasonic phased arrays in NDE applications, IEEE transactions on ultrasonics, ferroelectrics, and frequency control, 54 (2007) 1541-1550.

[78] M.V. Felice, A. Velichko, P.D. Wilcox, Accurate depth measurement of small surface-breaking cracks using an ultrasonic array post-processing technique, Ndt & E International, 68 (2014) 105-112.

[79] K. Sy, P. Brédif, E. Iakovleva, O. Roy, D. Lesselier, Development of the specular echoes estimator to predict relevant modes for total focusing method imaging, NDT & E International, 99 (2018) 134-140.

[80] J. Zhang, T. Barber, A. Nixon, P. Wilcox, Investigation into distinguishing between small volumetric and crack-like defects using multi-view total focusing method images, AIP Publishing LLC, pp. 040003.

[81] X.-L. Han, W.-T. Wu, P. Li, J. Lin, Combination of direct, half-skip and full-skip TFM to characterize multi-faceted crack, IEEE, pp. 1-4.

[82] X. Han, W. Wu, D. Zhang, H. Wan, Combination of direct, half-skip and full-skip TFM to characterize defect (II), IEEE, pp. 1612-1615.

[83] J. Zhang, B.W. Drinkwater, P.D. Wilcox, A.J. Hunter, Defect detection using ultrasonic arrays: The multi-mode total focusing method, NDT & e International, 43 (2010) 123-133.

[84] N. Quaegebeur, P. Masson, Correlation-based imaging technique using ultrasonic transmit–receive array for Non-Destructive Evaluation, Ultrasonics, 52 (2012) 1056-1064.

[85] A.J. Hunter, B.W. Drinkwater, P.D. Wilcox, The wavenumber algorithm for full-matrix imaging using an ultrasonic array, IEEE transactions on ultrasonics, ferroelectrics, and frequency control, 55 (2008) 2450-2462.

[86] G. Montaldo, M. Tanter, J. Bercoff, N. Benech, M. Fink, Coherent plane-wave compounding for very high frame rate ultrasonography and transient elastography, IEEE transactions on ultrasonics, ferroelectrics, and frequency control, 56 (2009) 489-506.

[87] L. Le Jeune, S. Robert, E.L. Villaverde, C. Prada, Plane wave imaging for ultrasonic non-destructive testing: Generalization to multimodal imaging, Ultrasonics, 64 (2016) 128-138.
[88] J. Camacho, M. Parrilla, C. Fritsch, Phase coherence imaging, IEEE transactions on ultrasonics, ferroelectrics, and frequency control, 56 (2009) 958-974.
[89] N. Portzgen, D. Gisolf, G. Blacquiere, Inverse wave field extrapolation: A different NDI approach to imaging defects, IEEE transactions on ultrasonics, ferroelectrics, and frequency control, 54 (2006) 118-127.
[90] K. Chougrani, N. Pörtzgen, IWEX: a new ultrasonic array technology for direct imaging of subsurface defects, 17th World Conference on Nondestructive Testing, Citeseer, 2008.
[91] C. Wassink, K. Chougrani, J. van der Ent, New possibilities for weld assessment using inverse wavefield extrapolation, International Journal of Sustainable Mechanical Engineering and Design, 4 (2013).
[92] M. Fink, C. Prada, F. Wu, D. Cassereau, Self focusing in inhomogeneous media with time reversal acoustic mirrors, Proceedings., IEEE Ultrasonics Symposium, IEEE, 1989, pp. 681-686.
[93] M. Fink, Time reversal of ultrasonic fields. I. Basic principles, IEEE transactions on ultrasonics, ferroelectrics, and frequency control, 39 (1992) 555-566.
[94] S. Reyes-Rodríguez, N. Lei, B. Crowgey, L. Udpa, S.S. Udpa, Time reversal and microwave techniques for solving inverse problem in non-destructive evaluation, Ndt & E International, 62 (2014) 106-114.
[95] H. Jeong, Time reversal study of ultrasonic waves for anisotropic solids using a Gaussian beam model, NDT & E International, 42 (2009) 210-214.
[96] C. Prada, E. Kerbrat, D. Cassereau, M. Fink, Time reversal techniques in ultrasonic nondestructive testing of scattering media, Inverse problems, 18 (2002) 1761.
[97] D.-Q. Nguyen, W.-S. Gan, Decomposition of time reversal operator method in a

small elastic scatterer, TENCON 2009-2009 IEEE Region 10 Conference, IEEE, 2009, pp. 1-6.

[98] E. Lopez Villaverde, S. Robert, C. Prada, Ultrasonic imaging of defects in coarse-grained steels with the decomposition of the time reversal operator, The Journal of the Acoustical Society of America, 140 (2016) 541-550.

[99] L.J. Cunningham, A.J. Mulholland, K.M.M. Tant, A. Gachagan, G. Harvey, C. Bird, The detection of flaws in austenitic welds using the decomposition of the time-reversal operator, Proceedings of the Royal Society A: Mathematical, Physical and Engineering Sciences, 472 (2016) 20150500.

[100] J. Zhang, B.W. Drinkwater, P.D. Wilcox, Defect characterization using an ultrasonic array to measure the scattering coefficient matrix, IEEE transactions on ultrasonics, ferroelectrics, and frequency control, 55 (2008) 2254-2265.

[101] L. Bai, A. Velichko, B.W. Drinkwater, Ultrasonic characterization of crack-like defects using scattering matrix similarity metrics, IEEE transactions on ultrasonics, ferroelectrics, and frequency control, 62 (2015) 545-559.

[102] L.J. Cunningham, A.J. Mulholland, K.M.M. Tant, A. Gachagan, G. Harvey, C. Bird, A spectral method for sizing cracks using ultrasonic arrays, Inverse Problems in Science and Engineering, 25 (2017) 1788-1806.

[103] N. Dominguez, V. Gibiat, Y. Esquerre, Time domain topological gradient and time reversal analogy: an inverse method for ultrasonic target detection, Wave motion, 42 (2005) 31-52.

[104] R. Seidl, E. Rank, Iterative time reversal based flaw identification, Computers & Mathematics with Applications, 72 (2016) 879-892.

[105] R. Seidl, E. Rank, Full waveform inversion for ultrasonic flaw identification, AIP Conference Proceedings, AIP Publishing LLC, 2017, pp. 090013.

[106] G. Xiang, L. Li, L. Boya, Y. Hongjuan, J. Jingpin, Experimental Investigation of Detection and Location of a Target in three-Layered Media Using the TR–RTM Mixed Method, 2019 14th Symposium on Piezoelectrcity, Acoustic Waves and Device

Applications (SPAWDA), IEEE, 2019, pp. 1-3.

[107] A. Asadollahi, L. Khazanovich, Analytical reverse time migration: An innovation in imaging of infrastructures using ultrasonic shear waves, Ultrasonics, 88 (2018) 185-192.

[108] J. Rao, A. Saini, J. Yang, M. Ratassepp, Z. Fan, Ultrasonic imaging of irregularly shaped notches based on elastic reverse time migration, NDT & E International, 107 (2019) 102135.

[109] M. Mitra, S. Gopalakrishnan, Guided wave based structural health monitoring: A review, Smart Materials and Structures, 25 (2016) 053001.

[110] A. Raghavan, Guided-wave structural health monitoring, 2007.

[111] J. Achenbach, Wave propagation in elastic solids, Elsevier, 2012.

[112] Z. Shen, S. Chen, L. Zhang, K. Yao, C.Y. Tan, Direct-Write Piezoelectric Ultrasonic Transducers for Non-Destructive Testing of Metal Plates, IEEE Sensors Journal, 17 (2017) 3354-3361.

[113] W. Ostachowicz, P. Kudela, P. Malinowski, T. Wandowski, Damage localisation in plate-like structures based on PZT sensors, Mechanical Systems and Signal Processing, 23 (2009) 1805-1829.

[114] S.B. Kim, H. Sohn, Instantaneous reference-free crack detection based on polarization characteristics of piezoelectric materials, Smart Materials and Structures, 16 (2007) 2375-2387.

[115] W. Wright, D. Hutchins, D. Jansen, D. Schindel, Air-coupled Lamb wave tomography, IEEE transactions on ultrasonics, ferroelectrics, and frequency control, 44 (1997) 53-59.

[116] D.P. Jansen, D.A. Hutchins, J.T. Mottram, Lamb wave tomography of advanced composite laminates containing damage, Ultrasonics, 32 (1994) 83-90.

[117] K.R. Leonard, E.V. Malyarenko, M.K. Hinders, Ultrasonic Lamb wave tomography, Inverse problems, 18 (2002) 1795.

[118] K.R. Leonard, M.K. Hinders, Multi-mode Lamb wave tomography with arrival

time sorting, The Journal of the Acoustical Society of America, 117 (2005) 2028-2038.
[119] C. Xu, J.L. Rose, X. Zhao, Detection principle of shape and orientation of corrosive defects using Lamb waves, Journal of Robotics and Mechatronics, 21 (2009) 568-573.
[120] P. Belanger, P. Cawley, F. Simonetti, Guided wave diffraction tomography within the born approximation, IEEE transactions on ultrasonics, ferroelectrics, and frequency control, 57 (2010) 1405-1418.
[121] J.-S. Lee, G. Park, C.-G. Kim, C.R. Farrar, Use of relative baseline features of guided waves for in situ structural health monitoring, Journal of Intelligent Material Systems and Structures, 22 (2011) 175-189.
[122] X. Zhao, R.L. Royer, S.E. Owens, J.L. Rose, Ultrasonic Lamb wave tomography in structural health monitoring, Smart Materials and Structures, 20 (2011) 105002.
[123] K.R. Leonard, E.V. Malyarenko, M.K.J.I.p. Hinders, Ultrasonic Lamb wave tomography, 18 (2002) 1795.
[124] K. Harri, P. Guillaume, S. Vanlanduit, On-line damage detection on a wing panel using transmission of multisine ultrasonic waves, NDT & E International, 41 (2008) 312-317.
[125] S.S. Kessler, S.M. Spearing, C. Soutis, Damage detection in composite materials using Lamb wave methods, Smart materials and structures, 11 (2002) 269.
[126] M. Lemistre, D. Balageas, Structural health monitoring system based on diffracted Lamb wave analysis by multiresolution processing, Smart materials and structures, 10 (2001) 504.
[127] Z. Su, L. Ye, Identification of damage using Lamb waves: from fundamentals to applications, Springer Science & Business Media, 2009.
[128] P.S. Tua, S.T. Quek, Q. Wang, Detection of cracks in plates using piezo-actuated Lamb waves, Smart Materials and Structures, 13 (2004) 643.
[129] A.J. Croxford, P.D. Wilcox, B.W. Drinkwater, Guided wave SHM with a distributed sensor network, Health Monitoring of Structural and Biological Systems

2008, International Society for Optics and Photonics, 2008, pp. 69350E.
[130] C. Fendzi, N. Mechbal, M. Rebillat, M. Guskov, G. Coffignal, A general Bayesian framework for ellipse-based and hyperbola-based damage localization in anisotropic composite plates, Journal of Intelligent Material Systems and Structures, 27 (2016) 350-374.
[131] J. Moll, R.T. Schulte, B. Hartmann, C.P. Fritzen, O. Nelles, Multi-site damage localization in anisotropic plate-like structures using an active guided wave structural health monitoring system, Smart materials and structures, 19 (2010) 045022.
[132] B. Li, L. Ye, Z. Li, Z. Ma, H. Kalhori, Quantitative identification of delamination at different interfaces using guided wave signals in composite laminates, Journal of Reinforced Plastics and Composites, 34 (2015) 1506-1525.
[133] L. Zeng, L. Huang, J. Lin, Damage imaging of composite structures using multipath scattering Lamb waves, Composite Structures, 216 (2019) 331-339.
[134] C.H. Wang, J.T. Rose, F.-K. Chang, A synthetic time-reversal imaging method for structural health monitoring, Smart materials and structures, 13 (2004) 415.
[135] B. Xu, V. Giurgiutiu, Single mode tuning effects on Lamb wave time reversal with piezoelectric wafer active sensors for structural health monitoring, Journal of Nondestructive Evaluation, 26 (2007) 123-134.
[136] J. Wang, Y. Shen, An enhanced Lamb wave virtual time reversal technique for damage detection with transducer transfer function compensation, Smart Materials and Structures, 28 (2019) 085017.
[137] H.W. Park, S.B. Kim, H. Sohn, Understanding a time reversal process in Lamb wave propagation, Wave Motion, 46 (2009) 451-467.
[138] B. Xu, V. Giurgiutiu, Lamb waves time-reversal method using frequency tuning technique for structural health monitoring, Sensors and Smart Structures Technologies for Civil, Mechanical, and Aerospace Systems 2007, International Society for Optics and Photonics, 2007, pp. 65290R.
[139] J.K. Agrahari, S. Kapuria, A refined Lamb wave time-reversal method with

enhanced sensitivity for damage detection in isotropic plates, Journal of Intelligent Material Systems and Structures, 27 (2016) 1283-1305.

[140] A.H.S. Ang, W.H. Tang, Probability concepts in engineering planning and design, basic principles, John Wiley & Sons Incorporated, 1975.

[141] D. Wang, L. Ye, Y. Lu, Z. Su, Probability of the presence of damage estimated from an active sensor network in a composite panel of multiple stiffeners, Composites Science and Technology, 69 (2009) 2054-2063.

[142] Z. Su, L. Cheng, X. Wang, L. Yu, C. Zhou, Predicting delamination of composite laminates using an imaging approach, Smart Materials and Structures, 18 (2009) 074002.

[143] D. Wang, L. Ye, Z. Su, Y. Lu, F. Li, G. Meng, Probabilistic damage identification based on correlation analysis using guided wave signals in aluminum plates, Structural Health Monitoring, 9 (2010) 133-144.

[144] C. Zhou, Z. Su, L. Cheng, Probability-based diagnostic imaging using hybrid features extracted from ultrasonic Lamb wave signals, Smart materials and structures, 20 (2011) 125005.

[145] D. Gao, Z. Wu, L. Yang, Y. Zheng, Guide waves-based multi-damage identification using a local probability-based diagnostic imaging method, Smart Materials and Structures, 25 (2016) 045009.

[146] J. Zhang, K. Liu, C. Gao, Z. Wu, Y. Zheng, D. Gao, Multi-mode guided waves based reference-free damage diagnostic imaging in plates, Structural Durability & Health Monitoring, 13 (2019) 41.

[147] J. Zhang, H. Xu, K. Zhou, Z. Yang, K. Liu, Y. Zheng, S. Ma, Z. Wu, Baseline-Free Damage Diagnostic Imaging Approach Relying on the Extraction of Converted Modes of Ultrasonic Guided Waves, Journal of Aerospace Engineering, 34 (2021) 04021071.

[148] R.O. Schmidt, A signal subspace approach to multiple emitter location and spectral estimation, Stanford University, 1982.

[149] M. Engholm, T. Stepinski, Direction of arrival estimation of Lamb waves using circular arrays, Structural Health Monitoring, 10 (2010) 467-480.
[150] H. Yang, Y.J. Lee, S.K. Lee, Impact source localization in plate utilizing multiple signal classification, Proceedings of the Institution of Mechanical Engineers, Part C: Journal of Mechanical Engineering Science, 227 (2013) 703-713.
[151] H. Yang, T.J. Shin, S. Lee, Source location in plates based on the multiple sensors array method and wavelet analysis, Journal of Mechanical Science and Technology, 28 (2014) 1-8.
[152] Y. Zhong, S. Yuan, L. Qiu, Multi-impact source localisation on aircraft composite structure using uniform linear PZT sensors array, Structure and Infrastructure Engineering, 11 (2015) 310-320.
[153] H. Zuo, Z. Yang, C. Xu, S. Tian, X. Chen, Damage identification for plate-like structures using ultrasonic guided wave based on improved MUSIC method, Composite Structures, 203 (2018) 164-171.
[154] Q. Bao, S. Yuan, Y. Wang, L. Qiu, Anisotropy compensated MUSIC algorithm based composite structure damage imaging method, Composite Structures, 214 (2019) 293-303.
[155] Q. Bao, S. Yuan, F. Guo, A new synthesis aperture-MUSIC algorithm for damage diagnosis on complex aircraft structures, Mechanical Systems and Signal Processing, 136 (2020) 106491.
[156] B. Xu, V. Giurgiutiu, Single Mode Tuning Effects on Lamb Wave Time Reversal with Piezoelectric Wafer Active Sensors for Structural Health Monitoring, Journal of Nondestructive Evaluation, 26 (2007) 123-134.
[157] P. Uginčius, Ray acoustics and Fermat's principle in a moving inhomogeneous medium, The Journal of the Acoustical Society of America, 51 (1972) 1759-1763.
[158] P. Wu, T. Stepinski, Extension of the angular spectrum approach to curved radiators, The Journal of the Acoustical Society of America, 105 (1999) 2618-2627.
[159] D. Belgroune, J.F. de Belleval, H. Djelouah, A theoretical study of ultrasonic

wave transmission through a fluid–solid interface, Ultrasonics, 48 (2008) 220-230.
[160] F. Varray, A. Ramalli, C. Cachard, P. Tortoli, O. Basset, Fundamental and second-harmonic ultrasound field computation of inhomogeneous nonlinear medium with a generalized angular spectrum method, IEEE transactions on ultrasonics, ferroelectrics, and frequency control, 58 (2011) 1366-1376.
[161] V. Giurgiutiu, Structural health monitoring: with piezoelectric wafer active sensors, Elsevier, 2007.
[162] Y. Wang, K. Ho, Unified near-field and far-field localization for AOA and hybrid AOA-TDOA positionings, IEEE Transactions on Wireless Communications, 17 (2017) 1242-1254.
[163] E. Grosicki, K. Abed-Meraim, Y. Hua, A weighted linear prediction method for near-field source localization, IEEE Transactions on Signal Processing, 53 (2005) 3651-3660.
[164] A. Swindlehurst, T. Kailath, Passive direction-of-arrival and range estimation for near-field sources, IEEE Spec. Est. and Mod. Workshop, Citeseer, 1988.
[165] Y. Zhong, S. Yuan, L. Qiu, An improved two-dimensional multiple signal classification approach for impact localization on a composite structure, Structural Health Monitoring, 14 (2015) 385-401.
[166] Y. Labyed, L. Huang, Ultrasound time-reversal MUSIC imaging with diffraction and attenuation compensation, IEEE transactions on ultrasonics, ferroelectrics, and frequency control, 59 (2012) 2186-2200.
[167] X. Yang, K. Wang, P. Zhou, L. Xu, J. Liu, P. Sun, Z. Su, Ameliorated-multiple signal classification (Am-MUSIC) for damage imaging using a sparse sensor network, Mechanical Systems and Signal Processing, 163 (2022) 108154.
[168] M. Morozov, W. Jackson, S.G. Pierce, Capacitive imaging of impact damage in composite material, Composites Part B: Engineering, 113 (2017) 65-71.
[169] F. Flora, M. Boccaccio, G.P.M. Fierro, M. Meo, Real-time thermography system for composite welding: Undamaged baseline approach, Composites Part B:

Engineering, 215 (2021) 108740.

[170] Z. Su, L. Zhou, L. Qiu, H. Xu, Z. Zhihui, L. Menglong, Resistance-voltage transformation system for sensors in dynamic strain measurement and structural health monitoring, Google Patents, 2018.

[171] Y. Okabe, J. Kuwahara, K. Natori, N. Takeda, T. Ogisu, S. Kojima, S. Komatsuzaki, Evaluation of debonding progress in composite bonded structures using ultrasonic waves received in fiber Bragg grating sensors, Smart materials and structures, 16 (2007) 1370.

[172] J.N. Potter, P.D. Wilcox, A.J. Croxford, Diffuse field full matrix capture for near surface ultrasonic imaging, Ultrasonics, 82 (2018) 44-48.

[173] M. Liu, K. Wang, C.J. Lissenden, Q. Wang, Q. Zhang, R. Long, Z. Su, F. Cui, Characterizing hypervelocity impact (HVI)-induced pitting damage using active guided ultrasonic waves: from linear to nonlinear, Materials, 10 (2017) 547.

[174] Z. Zhang, Y. Xiao, Y.Q. Liu, Z.Q. Su, A quantitative investigation on vibration durability of viscoelastic relaxation in bolted composite joints, Journal of Composite Materials, 50 (2016) 4041-4056.

[175] K. Wang, Z. Fan, Z. Su, Orienting fatigue cracks using contact acoustic nonlinearity in scattered plate waves, Smart Materials and Structures, 27 (2018) 09LT01.

[176] J.P. Jiao, B.W. Drinkwater, S.A. Neild, P.D. Wilcox, Low-frequency vibration modulation of guided waves to image nonlinear scatterers for structural health monitoring, Smart Materials and structures, 18 (2009) 065006.

[177] N.C. Yoder, D.E. Adams, Vibro-acoustic modulation utilizing a swept probing signal for robust crack detection, Structural Health Monitoring, 9 (2010) 257-267.

[178] T.J. Ulrich, P.A. Johnson, M. Müller, D. Mitton, M. Talmant, P. Laugier, Application of nonlinear dynamics to monitoring progressive fatigue damage in human cortical bone, Applied Physics Letters, 91 (2007) 213901.

[179] M. Meo, U. Polimeno, G. Zumpano, Detecting damage in composite material

using nonlinear elastic wave spectroscopy methods, Applied composite materials, 15 (2008) 115-126.

[180] G. Konstantinidis, B.W. Drinkwater, P.D. Wilcox, The temperature stability of guided wave structural health monitoring systems, Smart Materials and Structures, 15 (2006) 967.

[181] A. Raghavan, C.E.S. Cesnik, Effects of elevated temperature on guided-wave structural health monitoring, Journal of Intelligent Material Systems and Structures, 19 (2008) 1383-1398.

[182] A.J. Croxford, J. Moll, P.D. Wilcox, J.E. Michaels, Efficient temperature compensation strategies for guided wave structural health monitoring, Ultrasonics, 50 (2010) 517-528.